

Soft X-ray Spectroscopy of Molecular Species in Solution: Studies of Imidazole and Imidazole/Water Systems

A thesis submitted to The University of Manchester
for the degree of Doctor of Philosophy
in the Faculty of Engineering and Physical Sciences

Matthew J. Thomason

2012

School of Chemistry

Table of Contents

Abbreviations	5
Table of Figures.....	7
List of Tables	11
List of Scientific Terms	12
Abstract.....	13
Declaration.....	14
Copyright Statement.....	15
Acknowledgements.....	16
1. Introduction	17
1.1 <i>Background and context.....</i>	17
1.2 <i>Solution Structure and Crystal Nucleation Theory: Modern Approaches.....</i>	19
1.3 <i>Introduction to X-ray Absorption Spectroscopy (XAS).....</i>	22
1.4 <i>Early research on liquid systems with X-ray absorption spectroscopy.....</i>	24
1.5 <i>Specialised cells: investigations of liquid systems under extreme conditions</i>	28
1.6 <i>Organic molecular solutes and solids: a new field for soft X-ray core level spectroscopies</i>	30
1.7 <i>1H-Imidazole and its solutions.....</i>	33
1.7.1 <i>Properties of 1H-Imidazole</i>	33
1.7.2 <i>Self-Association in Imidazole Solutions</i>	36
1.7.3 <i>Soft X-ray photoelectron spectroscopy studies of aqueous imidazole solutions</i>	44
1.8 <i>Computational methods used to simulate NEXAFS.....</i>	50
1.9 <i>Objectives of the research described in this thesis.....</i>	51
2. Methods and Materials.....	53
2.1 <i>Preparation of imidazole solutions.....</i>	53
2.2 <i>Brønsted Equilibria and pH measurements.....</i>	53
2.2.1 <i>Speciation as a function of pH.....</i>	53
2.2.2 <i>Calculation of pH of a weak base.....</i>	55
2.2.3 <i>pH measurements</i>	56
2.3 <i>X-ray absorption spectroscopy.....</i>	57
2.4 <i>Synchrotron Radiation.....</i>	60
2.5 <i>Experimental NEXAFS Setup at BESSY</i>	61
2.6 <i>Raman Spectroscopy</i>	64
2.7 <i>StoBe DeMon Software.....</i>	65
2.8 <i>Gaussian.....</i>	66
2.8.1 <i>Single point energy calculation</i>	67
2.8.2 <i>Geometry Optimisation</i>	67

2.8.3	Frequency calculations	67
2.8.4	Modelling systems in solution.....	68
3.	N K-edge NEXAFS of Imidazole: A Comparative Computational Analysis of Gas Phase Monomer and Solid State Spectra	70
3.1	Introduction.....	70
3.2	Gas phase and solid state N K-edge spectra of imidazole.....	72
3.3	Methodology.....	73
3.4	Results and Discussion	74
3.4.1	Imidazole gas phase monomer	74
3.4.2	Crystalline imidazole.....	79
3.5	Conclusions	82
4.	N K-edge NEXAFS of concentrated aqueous imidazole solutions ($c > 1 \text{ mol L}^{-1}$)	83
4.1	Introduction.....	83
4.2	Methodology.....	84
4.3	Results	85
4.3.1	Raman spectroscopy of imidazole solutions	85
4.3.2	N K-edge NEXAFS.....	87
4.3.3	Imidazole-water dimers: influence of the donor-acceptor bond length	90
4.3.4	Analysis using microsolvation clusters	95
4.3.5	From partial to full hydration: larger clusters.....	103
4.4	Discussion	105
4.5	Conclusions	107
5.	Theoretical analysis of N K-edge NEXAFS of imidazole-imidazole aggregates and their interaction with water.....	108
5.1	Introduction.....	108
5.2	Methodology.....	108
5.3	Results and Discussion	108
5.3.1	Imidazole–imidazole interactions: chains	108
5.3.2	Imidazole–imidazole interactions: trimeric stacks	111
5.3.3	Combined imidazole-imidazole and imidazole-water interactions: microhydrated trimeric stacks	112
5.3.4	Optimised molecular dynamics imidazole trimer and 8 waters.....	114
5.4	Conclusions	118
6.	Aqueous imidazole solutions at low concentrations ($< 1\text{M}$): Comparative N K-edge NEXAFS measurements in water and in chloroform.....	119
6.1	Introduction.....	119
6.2	Methodology.....	120
6.3	Results and Discussion	120
6.3.1	N K-edge NEXAFS of dilute aqueous imidazole solutions	121
6.3.2	Self-association in the absence of imidazole-solvent hydrogen bonds: NEXAFS of imidazole in chloroform.....	123

6.3.3 Self-association in the absence of any hydrogen bonding: NEXAFS measurements of N-methyl imidazole dissolved in chloroform.....	124
6.4 Conclusions	124
7. Conclusions & Future Work.....	126
8. References.....	128
Appendix I: N K-edge NEXAFS data of obtained using an open stagnant solution cell.....	139
Appendix II: Co-Authored Publication.....	140
Appendix III: Stobe Operational Procedures	146

Abbreviations

AIP	Adiabatic ionization potential
API	Active pharmaceutical ingredient
ATR-FTIR	Attenuated total reflectance Fourier transform infrared spectroscopy
a.u.	Arbitrary units
CPS	Counts per second
DFT	Density functional theory
DSC	Dynamic scanning calorimetry
DVS	Dynamic vapour sorption
EDX	Energy-dispersive X-ray analysis
EELS	Electron energy loss spectroscopy
ESXD	Energy scanning X-ray diffraction
EXAFS	Extended X-ray absorption fine structure
EY	Electron-yield
FTIR	Fourier transform infrared spectroscopy
FWHM	Full width at half maximum
FY	Fluorescence-yield
GIXD	Grazing incidence X-ray diffraction
imidazole	1 <i>H</i> -imidazole
IP	Ionisation potential
IR	Infrared spectroscopy
ISEELS	Inner-shell electron energy loss spectroscopy
LCAO	Linear combinations of atomic orbitals
LINAC	Linear [electron] accelerator
LUMO	Lowest unoccupied molecular orbital
MD	Molecular dynamics
MDSC	Modulated dynamic scanning calorimetry
NEXAFS	Near-edge X-ray absorption fine-structure (synonymous with XANES)
NMR	Nuclear magnetic resonance
PCM	Polarisable continuum model
PES	Photoelectron spectroscopy
PPM	parts per million
SAXS	Small angle X-ray scattering
SEM	Scanning electron microscopy
ssNMR	Solid-state nuclear magnetic resonance
StoBe	Stockholm-Berlin code
TGA	Thermogravimetric analysis
UV-vis	Ultraviolet / visible spectroscopy

VIP Vertical ionisation potential
WAXD Wide angle X-ray diffraction
WAXS Wide angle X-ray scattering
XANES X-ray absorption near-edge structure (synonymous with NEXAFS)
XAS X-ray absorption spectroscopy
XES X-ray emission spectroscopy
XPS X-ray photoelectron spectroscopy
XRD X-ray diffraction
XRPD X-ray Powder Diffraction

Table of Figures

Figure 1	X-ray interactions with matter.	23
Figure 2	X-ray absorption K-edge of a Cu metal foil, underlying absorption processes and information that can be obtained from them; definition of NEXAFS and EXAFS region. ^[40]	24
Figure 3	Three different chemical representations of 1 <i>H</i> -imidazole; note the IUPAC numbering of the ring atoms in the centre formula.	33
Figure 4	Cut-out from the unit cell of the imidazole crystal structure, indicating the motif of hydrogen-bonded chains. The sketch on the right ^[170] indicates the length of the N-H donor and H...N acceptor bonds.	34
Figure 5	Number of water molecules available for hydration of a solute as a function of the concentration of the solute in water.	35
Figure 6	Imidazole speciation in aqueous solution as a function of pH, calculated from p <i>K</i> _a values as described in section 2.2.2.	37
Figure 7	UV absorption spectra of imidazole in aqueous solution: ^[199] 1.006×10 ⁻⁴ M at pH = 3.2 (—); 1.025×10 ⁻⁴ M at pH = 6.9 (...), and 1.032×10 ⁻⁴ M at pH = 11.0 (---).	38
Figure 8	Solvent effect on UV absorption spectra of imidazole: ^[199] 1.032 × 10 ⁻⁴ M in NaOH at pH = 11.0 (—) vs. saturated solution in n-hexane (...).	39
Figure 9	Hypochromic effect in UV spectra of aqueous imidazole solutions in the concentration range from 5×10 ⁻⁵ mol L ⁻¹ to 5.1×10 ⁻⁴ mol L ⁻¹ .	39
Figure 10	Structural model for the self-association of imidazole in basic aqueous solutions as proposed by Peral and Gallego. ^[199]	40
Figure 11	Experimental radial distribution functions for (a) Pure water, (b) 4.5 M aqueous imidazole, (c) 7.61 M aqueous imidazole.	41
Figure 12	Bent stacked imidazole structure model for concentrated aqueous solutions (4.5M and 7.61M) as deduced from radial distribution functions determined by EDXD. ^[200]	42
Figure 13	Distribution of stacked and chain dimers vs. imidazole concentration for (a) QCT simulations and (b) AMBER simulations. ^[202]	43
Figure 14	Photoelectron spectra of 2M imidazole and pure water. ^[145]	46
Figure 15	A selection of the microsolvated imidazole·nH ₂ O clusters used for the analysis of the VIP in photoemission spectra from 2M aqueous imidazole solutions. ^[145]	47
Figure 16	N 1s and C 1s XPS results for aqueous imidazole solutions at a pH of 2.6 and 10.5. ^[147]	48
Figure 17	Experimental values vs. predicted pH of ideal imidazole solutions as a function of concentration.	57
Figure 18	Background subtraction for transmission spectrum of Ni metal. ^[96]	59
Figure 19	Components of a Synchrotron radiation laboratory. ^[223] (1) Electron gun; (2) LINAC; (3) Booster ring; (4) Storage ring; (5) Beamline; (6) End station	60
Figure 20	Wiggler device inserted into Storage ring. ^[223]	61
Figure 21	Effects of wigglers and undulators on the X-ray beam. ^[223]	61
Figure 22	Experimental chamber; note the amount of tin foil used to ensure that the photodiode does not detect any background light.	62
Figure 23	Inside the chamber; three x, y, and z stages control and align the X-rays, photo-diode, digital camera and sample holder.	63
Figure 24	This is the position at which the X-rays are aligned to the sample holder. Note the digital camera on the left; this was useful for recognising leaks or crystallisation.	63

Figure 25	Flow cell used during flow experiments. ^[224]	64
Figure 26	Horiba Jobin-Yvon LabRam 300 Raman spectrometer used for this study	65
Figure 27	Fluorescence-yield (FY) and electron-yield (EY) NEXAFS spectra of solid imidazole in comparison with the gas phase inner-shell electron energy loss spectrum (ISEELS) of gas phase imidazole. Modified version of a figure taken from the paper by Apen et al. ^[170]	72
Figure 28	N K-edge NEXAFS spectrum of a gas phase imidazole monomer, as calculated with the StoBe code. Shown are the two individual absorption spectra of the two nitrogen moieties N1 (NH) and N3 (N=) in the molecule, and the combined spectrum, which can be compared to the experimentally observed ISEELS spectrum in Figure 27.	75
Figure 29	Electron density maps for the lowest unoccupied molecular orbital (LUMO) of imidazole #19 (left), the second-lowest unoccupied molecular orbital #20 (middle), and the third-lowest unoccupied molecular orbital #21 (right). Orbital energies are noted below each orbital.	76
Figure 30	Comparison of experimental ISEELS ^[170] and predicted N K-edges for an imidazole monomer, with an energetic shift of 2.4 eV between the two N 1s core level binding energies applied, as taken from experiment/StoBe. The theoretical spectrum was calculated with energy-dependent lifetime broadening and has been energetically shifted relative to the experimental result to obtain best energy match. ^[255]	78
Figure 31	Calculated N K-edge NEXAFS spectrum of solid imidazole, as predicted by the StoBe code for the central molecule in a cluster of 6 molecules cut out from the crystal structure of imidazole. Shown are the two individual absorption spectra of the two nitrogen moieties N1 (NH) and N3 (N=) in the central molecule, as indicated in the cluster structure shown, and the combined spectrum, which can be compared to the experimentally observed electron-yield XAS spectrum in Figure 27.	79
Figure 32	Comparison of experimental electron-yield XAS ^[170] and predicted N K-edges for solid imidazole, with an energetic shift of 1.3 eV between the two N 1s core level binding energies applied. The theoretical spectrum was calculated by Seabourne ^[255] with energy-dependent lifetime broadening and has been energetically shifted relative to the experimental result to obtain best energy match.	81
Figure 33	Raman assignments ^[179,258,259] for bands between 1000 cm ⁻¹ to 1800.cm ⁻¹ . See also table below. In plane vibrations ω = ring stretching, δ = bending ν = stretching, Δ = ring bending out of plane vibrations T = ring bending	85
Figure 34	Raman spectra of aqueous imidazole solutions from 0.03 M to 0.5 M	86
Figure 35	Raman spectra of aqueous imidazole solutions from 1.0 M to 8.1 M	87
Figure 36	N K-edge near edge X-ray absorption fine structure (NEXAFS) spectra of aqueous imidazole solutions as a function of concentration from 0.5 mol L ⁻¹ to 8.2 mol L ⁻¹	88
Figure 37	Calculated N K-edge absorption spectrum of the imidazolium cation.	90
Figure 38	Calculated N K-edge NEXAFS spectra of imidazole·H ₂ O gas phase clusters under variation of the HOH...N3 (N=) distance. Corresponding N 1s core level binding energies of the two N atoms are noted alongside each spectrum.	91
Figure 39	Calculated N 1s core level binding energies of the N-atoms in imidazole·H ₂ O gas phase clusters under variation of the HOH...N3 (N=) distance.	92
Figure 40	Calculated N K-edge NEXAFS spectra of imidazole·H ₂ O gas phase clusters under variation of the H ₂ O...HN distance. Corresponding N 1s core level binding energies of the two N atoms are noted alongside each spectrum.	93
Figure 41	Calculated N 1s core level binding energies of the N-atoms in imidazole·H ₂ O gas phase clusters under variation of the H ₂ O...HN1 distance.	94
Figure 42	Calculated N K-edge NEXAFS spectrum of the geometry-optimised imidazole·H ₂ O gas phase imidazole/water cluster ‘Imi 1 wat v5’ of Jagoda-Cwiklik et al. ^[145] The inset shows the cluster along the three Cartesian axes and reports the 1s core level binding energies of the two N atoms.	95
Figure 43	Calculated N K-edge NEXAFS spectrum of the geometry-optimised imidazole·2H ₂ O gas phase imidazole/water cluster ‘Imi 2 wat v7’ of Jagoda-Cwiklik et al. ^[145] The inset shows the cluster	

	along the three Cartesian axes and reports the 1s core level binding energies of the two N atoms.	96
Figure 44	Calculated N K-edge NEXAFS spectrum of the geometry-optimised imidazole·3H ₂ O gas phase imidazole/water cluster ‘Imi 3 wat v700’ of Jagoda-Cwiklik et al. ^[145] The inset shows the cluster along the three Cartesian axes and reports the 1s core level binding energies of the two N atoms.	96
Figure 45	Calculated N K-edge NEXAFS spectrum of the geometry-optimised imidazole·3H ₂ O gas phase imidazole/water cluster ‘Imi 3 wat v900’ of Jagoda-Cwiklik et al. ^[145] The inset shows the cluster along the three Cartesian axes and reports the 1s core level binding energies of the two N atoms.	97
Figure 46	Calculated N K-edge NEXAFS spectrum of the geometry-optimised imidazole·4H ₂ O gas phase imidazole/water cluster ‘Imi 4 wat v1’ of Jagoda-Cwiklik et al. ^[145] The inset shows the cluster along the three Cartesian axes and reports the 1s core level binding energies of the two N atoms.	98
Figure 47	Calculated N K-edge NEXAFS spectrum of the geometry-optimised imidazole·4H ₂ O gas phase imidazole/water cluster ‘Imi 4 wat v1000’ of Jagoda-Cwiklik et al. ^[145] The inset shows the cluster along the three Cartesian axes and reports the 1s core level binding energies of the two N atoms.	99
Figure 48	Calculated N K-edge NEXAFS spectrum of the geometry-optimised imidazole·4H ₂ O gas phase imidazole/water cluster ‘Imi 4 wat v7800’ of Jagoda-Cwiklik et al. ^[145] The inset shows the cluster along the three Cartesian axes and reports the 1s core level binding energies of the two N atoms.	99
Figure 49	Calculated N K-edge NEXAFS spectrum of the geometry-optimised imidazole·4H ₂ O gas phase imidazole/water cluster ‘Imi 4 wat v7835’ of Jagoda-Cwiklik et al. ^[145] The inset shows the cluster along the three Cartesian axes and reports the 1s core level binding energies of the two N atoms.	100
Figure 50	Calculated N K-edge NEXAFS spectrum of the geometry-optimised imidazole·5H ₂ O gas phase imidazole/water cluster ‘5wat’ of Jagoda-Cwiklik et al. ^[145] The inset shows the cluster along the three Cartesian axes and reports the 1s core level binding energies of the two N atoms.	100
Figure 51	Summary stacked plot showing all calculated N K-edge NEXAFS spectrum of the geometry-optimised gas phase imidazole/water clusters of Jagoda-Cwiklik et al. ^[145]	102
Figure 52	Calculated N K-edge NEXAFS spectrum of an imidazole·5H ₂ O gas phase imidazole/water cluster obtained from an MD simulation.	103
Figure 53	Calculated N K-edge NEXAFS spectrum of an imidazole·15H ₂ O gas phase imidazole/water cluster obtained from an MD simulation.	104
Figure 54	Calculated N K-edge absorption spectra for the monomer and hydrogen bonded chains of imidazole molecules taken out of the crystal structure of imidazole. The spectra were always calculated for the two nitrogen atoms closest to the centre of the molecule.	109
Figure 55	Calculated N K-edge absorption spectra for the monomer and hydrogen bonded chains of imidazole molecules taken from gas phase structures. The spectra were always calculated for the two nitrogen atoms closest to the centre of the molecule.	110
Figure 56	Calculated N K-edge absorption spectrum for the central molecule in a Gaussian 03 optimised stack of 3 imidazole molecules.	112
Figure 57	Calculated N K-edge absorption spectrum for the central molecule in a microhydrated Gaussian 03 optimised stack of 3 imidazole molecules.	113
Figure 58	Calculated N K-edge spectra for water-coordinated trimer stacks under variation of the imidazole-water distances in the Gaussian 03-derived imidazole stack	114
Figure 59	Calculated N K-edge absorption spectrum for the central molecule in a microhydrated cluster of 3 imidazole molecules and 8 water molecules. Shown are the structure and the associated spectrum before optimisation by molecular dynamics.	115

- Figure 60 Calculated N K-edge absorption spectrum for the central molecule in a microhydrated cluster of 3 imidazole molecules and 8 water molecules. Shown are the structure and the associated spectrum after 75 molecular dynamics optimisation steps. 115
- Figure 61 Calculated N K-edge absorption spectrum for the central molecule in a microhydrated cluster of 3 imidazole molecules and 8 water molecules. Shown are the structure and the associated spectrum after 150 molecular dynamics optimisation steps. 116
- Figure 62 Calculated N K-edge absorption spectrum for the central molecule in a microhydrated cluster of 3 imidazole molecules and 8 water molecules. Shown are the structure and the associated spectrum after 225 molecular dynamics optimisation steps. 116
- Figure 63 Calculated N K-edge absorption spectrum for the central molecule in a microhydrated cluster of 3 imidazole molecules and 8 water molecules. Shown are the structure and the associated spectrum after 300 molecular dynamics optimisation steps. 117
- Figure 64 Summary plot of all calculated spectra during MD optimisation of the imidazole trimer·8H₂O structure 117
- Figure 65 N K-edge near edge X-ray absorption fine structure (NEXAFS) spectra of flowing aqueous imidazole solutions as a function of concentration from 0.03 mol L⁻¹ to 0.5 mol L⁻¹. Also included is a spectrum of a 0.03 mol L⁻¹ stagnant solution. 120
- Figure 66 N K-edge near edge X-ray absorption fine structure (NEXAFS) spectra of four stagnant aqueous imidazole solutions, measured in the flow cell as a function of concentration from 0.03 mol L⁻¹ to 8.2 mol L⁻¹. 122
- Figure 67 N K-edge near edge X-ray absorption fine structure (NEXAFS) spectra of flowing imidazole solutions in chloroform as a function of concentration, from 0.5 mol L⁻¹ to 2.0 mol L⁻¹. 123
- Figure 68 N K-edge near edge X-ray absorption fine structure (NEXAFS) spectra of flowing N-methylimidazole solutions in chloroform as a function of concentration, from 0.5 mol L⁻¹ to 2.5 mol L⁻¹. 124
- Figure 69 Experimental N K-edge NEXAFS data of aqueous imidazole solutions from 0.03 M to 8.2 obtained in an open stagnant container cell enclosed in a He-filled chamber. These data were acquired during an initial run at BESSY, but indicated a number of problems with the setup. First, air ingress resulted in contamination of the data by emission from gaseous N₂; evaporation of solvent led to the detection of solid imidazole (bottom spectrum) at the saturation concentration; later studies (see chapter 6) with a flow cell indicated that beam damage and other restructuring effects may take place under stagnant conditions. 139

List of Tables

Table 1	Radial distribution function peak assignments for water. ^[200]	42
Table 2	Radial distribution function peak assignments for concentrated aqueous imidazole solutions. ^[200]	42
Table 3	Comparison of PCM results ^[145] against experimental ionisation potentials	45
Table 4	Comparison of equilibrium and non equilibrium PCM potentials ^[145] against vertical ionisation potentials of halides in solution.	45
Table 5	Calculated VIPs for microsolvation clusters of increasing complexity. ^[145]	48
Table 6	Experimental and calculated C1s and N1s core level binding energies for neutral imidazole and imidazolium species. ^[147]	49
Table 7	Scale factors for frequencies and zero-point energies (ZPEs) in Gaussian.	68
Table 8	N 1s peak positions and assignments for the solid state and gas phase imidazole spectra shown in Figure 27. Adapted table taken from the paper by Apen et al. ^[170] .	73
Table 9	Calculated and experimental IPs and 1s → π^* transition energies for gas phase imidazole monomers.	76
Table 10	Ground state molecular orbitals and their energies for an isolated imidazole molecule, as calculated by Gaussian 03.	77
Table 11	Calculated and experimental ^[170] IPs and 1s → $1\pi^*$ transition energies for solid imidazole. For comparison the calculated gas phase monomer values previously reported in Table 9 are also included.	80
Table 12	Summary of Raman vibrational bands ^[179,258,259] including small spectral features at 626 cm^{-1} and 3149 cm^{-1}	86
Table 13	Calculated N1s core level binding energies and energy difference between the N1 ('NH') and N3 ('N=') 1s → $1\pi^*$ NEXAFS bands for the imidazole N atoms in the geometry-optimised gas phase imidazole/water clusters of Jagoda-Cwiklik et al. ^[145] .	101

List of Scientific Terms

A	Area
C_p	Heat capacity
E_B	Binding energy
E_K	Kinetic energy
ΔH	Enthalpy change
h	Planck constant (= 6.626×10^{-34} J s)
$h\nu$	Photon energy
I	Intensity / Nuclear spin quantum number
j	Quantum number
K	DSC calibration constant / Dissociation constant
K_a	Acid dissociation constant
$\text{p}K_a$	Negative logarithm of acid dissociation constant
$\Delta\text{p}K_a$	Change in $\text{p}K_a$ [$\text{p}K_a$ (base) – $\text{p}K_a$ (acid)]
L	Orbital quantum number
m	Mass
n	Principal quantum number
P	Pressure
Q	Heat flow
r	Rate
s	Spin quantum number
T_g	Glass transition temperature
T_m	Melting temperature
Z	Atomic number
δ	Chemical shift
ϕ_w	Work function
λ	IMFP <i>or</i> Wavelength
μ	Micro-
ν	Frequency
θ	Theta / Diffraction angle
σ	Shielding value /Wavenumber

Units

eV	Electronvolt	= 1.602×10^{-19} J
J	Joule	= 6.24×10^{18} eV
mbar	Millibar	= 0.750 Torr
		= 100 Pascals
ppm	Parts per million	
a.u.	Arbitrary units	

Abstract

Soft X-ray near-edge X-ray absorption fine-structure (NEXAFS) spectroscopy of liquids, an emerging synchrotron radiation technique, has been applied to characterise the local environment of imidazole in aqueous solution to elucidate the structural nature of the well known self-association effects in this system. Atomic core level spectroscopies such as NEXAFS are extremely sensitive to short range structure, including bond lengths and angles as well as coordination numbers, in condensed matter and in molecular systems.

N K-edge NEXAFS data were successfully acquired for aqueous imidazole solutions were studied from low concentrations (10^{-2} mol L⁻¹) to saturation (> 8 mol L⁻¹). Previous UV/Vis studies had established that imidazole undergoes significant self-association already at concentration well below 1 mol L⁻¹ while energy-dispersive X-ray diffraction studies indicated the formation of water mediated hydrogen-bonded self-associated structures of imidazole.

NEXAFS revealed that in the concentration range from 0.50 (~100 H₂O molecules per imidazole molecule) to the saturation concentration of 8.20 mol L⁻¹ (~7 H₂O molecules per imidazole molecule) no significant variation in the local coordination around imidazole molecules takes place. It appears that progressive self-association at higher concentration is not associated with local structural changes.

Using *ab initio* calculations of N K-edge spectra for complex structure models that explicitly included the evaluation of imidazole gas phase data, the imidazole crystal structure as well as imidazole-imidazole and imidazole-solvent interactions in solution, it was possible to relate the observed imidazole spectra to structure models. Systematic calculations evaluating gas phase monomers and oligomers of pure imidazole, the solid state of imidazole, stacked self-associated imidazole clusters in solution, chained structures of self-associated clusters in solution, and explicitly including the water solvation shell were carried out. Comparative measurements in with chloroform solutions shed some light on the nature of the self-associates present at the lower concentrations investigated in this work.

Examining also synergistic interactions between imidazole and water the view was obtained that increasing the concentration of imidazole solutions leads to the assembly of self-associated clusters of hydrated imidazole monomers, which are held together by secondary interactions that are weaker than the hydrogen bonding in the hydrate shell. This result demonstrates the suitability of soft X-ray spectroscopy measurements for the investigation of local structure in solutions of molecular organic solutes.

Declaration

This dissertation is the result of my own work, except where reference is made to other sources. Furthermore, except where explicitly stated, it includes nothing which is the outcome of work done in collaboration. It has not been submitted, in whole or in part, for a degree or any other qualification at another university.

Matthew Thomason
The University of Manchester

Copyright Statement

i. The author of this thesis (including any appendices and/or schedules to this thesis) owns certain copyright or related rights in it (the “Copyright”) and s/he has given The University of Manchester certain rights to use such Copyright, including for administrative purposes.

ii. Copies of this thesis, either in full or in extracts and whether in hard or electronic copy, may be made **only** in accordance with the Copyright, Designs and Patents Act 1988 (as amended) and regulations issued under it or, where appropriate, in accordance with licensing agreements which the University has from time to time. This page must form part of any such copies made.

iii. The ownership of certain Copyright, patents, designs, trade marks and other intellectual property (the “Intellectual Property”) and any reproductions of copyright works in the thesis, for example graphs and tables (“Reproductions”), which may be described in this thesis, may not be owned by the author and may be owned by third parties. Such Intellectual Property and Reproductions cannot and must not be made available for use without the prior written permission of the owner(s) of the relevant Intellectual Property and/or Reproductions.

iv. Further information on the conditions under which disclosure, publication and commercialisation of this thesis, the Copyright and any Intellectual Property and/or Reproductions described in it may take place is available in the University IP Policy (see <http://www.campus.manchester.ac.uk/medialibrary/policies/intellectual-property.pdf>), in any relevant Thesis restriction declarations deposited in the University Library, The University Library’s regulations (see <http://www.manchester.ac.uk/library/aboutus/>) and in The University’s policy on presentation of Theses.

Acknowledgements

The main influence in my undertaking of this research was the encouragement from my MChem project supervisor Sven Schroeder. Sven offered me a PhD in an upcoming area of synchrotron science, the analysis of solutions using soft XAS. This opportunity has opened the way for me to develop and learn techniques and comprehend aspects of this complex area of science.

Initial beam line experiments led to a three year long collaboration with a then 4th year PhD student at BESSY, Berlin, now Professor Emad F Aziz. Emad was a knowledgeable and enthusiastic a true character and over the further visits to BESSY became not only a research collaborator but a friend. Always willing to spend those extra hours on the beam line to complete experiments. Emad opened the door to the main body of my research, over a full week he taught me the basics of StoBe simulations. This really was the start of the story in terms of future collaborations and interpreting soft XAS studies of imidazole.

I would also like to specifically thank a Guy Hembury for his support and ongoing questioning of my work during my first three years. It has been a great working atmosphere in the research group to and I would like to thank Luanga Nchari, David Meehan and the rest of the group.

Computationally on Gaussian Ben Sattelle assisted greatly with my first theoretical calculations. This led to further successful collaboration with Prof Paul Popelier's group and Majeed Shaiks cutting edge molecular dynamic calculations.

I am indebted to Dr Che Seabourne for sharing his CASTEP results for gas phase and crystalline imidazole. I also thank Professor Pavel Jungwirth for sharing the structure parameters for his optimised gas phase imidazole/water clusters.

Finally I can't really thank enough the help, support and patience from my wife Jennifer and parents Mark and Lesley and my brother Andrew.

1. Introduction

1.1 Background and context

Crystallisation is one of the oldest and most familiar branches of science. Crystal growth experiments have been performed by many people while still at school. It therefore comes as a surprise to many, even within scientific circles, that the process of crystallisation from liquid solutions is still not well understood at the molecular level. As will be explained in more detail in section 1.2 below, the gap in our scientific understanding is the so-called nucleation state.^[1,2] This is believed to be a dense but not solid state assembled from molecules present in the supersaturated state of a solution, just before crystallisation takes place. The structure and dynamics of this ‘transition state’, and how it controls the structural outcome of the crystallisation are still almost completely unknown. This state of affairs is largely due to the fact that experimental techniques that provide sufficiently incisive structural insight into the molecular structure around solutes in solution have been hard to come by.^[2]

The fundamental obstacle to deepening our understanding of nucleation are the experimental difficulties associated with obtaining data directly from nucleating solutions, to relate nucleation events to intra- and inter-molecular composition and structure. The limited knowledge we already have has come from the application of various experimental techniques, which sometimes shed light on some aspect of the early stages of crystallisation. These including single crystal X-ray diffraction (XRD), small angle X-ray scattering (SAXS), wide angle X-ray diffraction (WAXS), neutron scattering, *in situ* optical microscopy, infrared spectroscopy (IR), grazing incidence X-ray diffraction (GIXD), atomic force microscopy (AFM) and scanning electron microscopy (SEM). Very useful are also computational modelling approaches such as molecular dynamics simulations, semi-empirical methods and density functional theory.

The project described in this thesis examines whether near-edge X-ray absorption fine-structure (NEXAFS) spectroscopy with soft X-rays, which is an emerging technique for studying the molecular structure of and around solutes in solution, can be applied to the characterisation of the early stages of nucleation and crystallisation. The overall objective was to demonstrate that information on the nature of the structure of a highly self-

associated solute/solution system could be obtained, with a view to paving the way for studies of supersaturated systems, from which the formation of crystal nuclei with well-defined long-range crystallographic structure begins.

On the practical side, understanding nucleation behaviour is of importance for a wide range of industrial processes. However, particular scientific interest relates to molecular crystals in the pharmaceutical industry, with the grand challenge being the prediction and control of polymorph formation. Polymorphism is the formation of different crystal structures for the same chemical compound and an important phenomenon associated with the crystallisation of molecular materials. Polymorphism has important implications for the resulting material's physical, chemical as well as biochemical and biomedical properties, and has far-reaching implications on patent ownership in the pharmaceutical industry. As with crystallization in general, the critical stage in polymorph formation is also the nucleation state.^[1,3] Thus, it is the structure of this state, and how it is influenced, which is key to understanding, predicting and controlling the polymorphic outcome of a crystallization.

As will be explained in the objectives section (1.9) below, for a number of reasons it was decided to choose aqueous imidazole solutions as a molecular solute for this work. Imidazole solutions had not been previously analysed in solution with X-ray absorption spectroscopy (XAS). In fact, the XAS investigations carried out in this work represents the first XAS study of a non-ionic molecular organic solute in solution. Work in the first year focused on a feasibility study, performing spectroscopy on a simple open cell with stagnant solutions at the BESSY-II synchrotron source in Berlin, Germany, and exploring StoBe simulations of the spectra. This work indicated that good quality data could readily be obtained over a wide range of concentrations (10^{-3} mol L⁻¹ to saturation concentrations around 10 mol L⁻¹). However, this work also revealed the limits of the open cell approach and the use of stagnant solutions. First, evidence for X-ray beam damage in the stagnant system was observed, and second, for high concentrations, evaporation near the solution surface led to the observation of crystallised solid rather than of the desired solution. XAS work in the 2nd year was therefore performed using a newly developed closed flow cell developed by our cooperation partners at BESSY-II. Additional data were acquired and the results were interpreted using computational modelling with the StoBe code, which continued throughout the third year of the PhD. It was found that small cluster models did not account reliably for the observed

experimental data. More complex cluster models obtained by molecular dynamics simulations in the group of P.L.A. Popelier at Manchester were tested and found to yield better agreement with experiment.

1.2 Solution Structure and Crystal Nucleation Theory: Modern Approaches

The concept of the nucleation stage of crystallization was established over 60 years ago in the pioneering work by Volmer.^[4] Briefly, classical nucleation theory states that the process occurs in two distinct steps, firstly, molecules in a supersaturated solution aggregate to form organized nuclei so developing a surface that separates them from the environment, with their size dictating the stability; secondly, once the nuclei have crossed a critical size, making the total free energy of the growth process fall and eventually become negative, the continued growth becomes a favourable process.^[5,6] However, this essentially thermodynamic consideration of nucleation theory does not consider the importance of intermolecular interactions as well as the precise structural nature of the pre-crystalline state.

Supramolecular chemistry and biochemistry are areas of science in which it is well established that dynamics and kinetics contribute to an assembly process, including their change over the time course of a crystallisation process. This conclusion can also be drawn from traditional crystallisation experiments whose outcomes vary with factors such as temperature, evaporation rate, solvent, concentration and pressure. However, due to the lack of insight and appreciation of the dynamic nature of the nucleation state, such intermolecular factors, clearly crucial in the outcome, are absent from classical nucleation theory.

As reviewed by Oxtoby,^[7] new theoretical models have therefore been developed since Volmer's work, which indicate that classical theory fails both quantitatively and qualitatively in various situations. For example, it has been realised that the critical nuclei can differ drastically from the eventual new phase in both composition and structure. This is well highlighted by work by Hartke^[8] on molecular clusters of noble gases, mercury, water and others found in gas expansion experiments: "if one adds more particles to a cluster, the energetically optimal structure is neither preserved nor changes in a continuous fashion. Instead, several cluster size regions are found where one structural principle generally dominates. The structure of the solid is usually reached at relatively large sizes after more than one structural transition". Work by Cooks et al^[9] similarly

found that the size of serine molecular clusters and the nature of their intermolecular interactions were key to stability. Using electrospray ionization mass spectrometry experiments of water-methanol solutions of serine they showed that it tends to form “magic number” clusters of eight molecules composed of four hydrogen-bonded dimers from 1:1.

From single crystal X-ray diffraction analysis and studies of the Cambridge Structural Database, as pioneered by Desiraju,^[10] has come the concept of a ‘supramolecular synthon’. These are common building blocks of intermolecular interactions that are found to influence crystal packing (e.g. the carboxylic acid dimer). This concept when considered along with the similar structural building blocks found to influence the assembly of discrete assemblies in solution (supramolecular) chemistry, has led researchers to postulate how the initial (observable) interacting species in solution relate to their crystal structures via the nucleation state. In this light work by Hunter and Davey used high resolution solution ¹H NMR chemical shift data obtained from as close to the nucleation state as possible,^[11] to generate 3D structures of the molecule via computational methods.^[12] The results suggested that the solution and solid state structures were similar, but gave no insight into the greater intermolecular structure of the nucleation clusters.

Experimental studies of the structure of supersaturated and especially concentrated solutions of molecular solutes therefore receive increasing attention in the context of elucidating the self-assembly pathways leading to crystallisation.^[2,13-17] A few examples of experimental studies that have been able to provide structural information on the nucleation state shall be given. For example, Davey et al discovered various structural aspects for small molecular systems by solution nuclear magnetic resonance (NMR),^[18] which provide details as to the interactions present in compounds during the initial stages of crystallisation. The relevant concentration dependent change of two different compounds allowed for a prediction of the packing in the crystal structure. Nucleation in solid ordered protein phases suggests that a two-step nucleation process takes place.^[19] The nucleation process occurs within a region with a dense state of molecules for a brief time. This nucleation scenario for proteins has been supported by a number of studies.^[20-22] Small-angle X-ray scattering (SAXS) and wide-angle X-ray diffraction (WAXD) have been used to study small organic molecules in an attempt to probe the nucleation and crystallisation states.^[23] These studies report SAXS intensity arising from entities that are

not crystalline in nature. These results imply that the initial step of a phase transition occurs on separation of a non-crystalline, possibly amorphous, phase. This separation then rapidly generates crystals. *In situ* optical microscopy^[24] confirmed the presence of such an amorphous phase during small molecule crystallisation. The analysis revealed a separation event in the solute-rich liquid immediately before crystallisation, but it was also highlighted that there is a need for further in depth studies to allow understanding on a molecular level. Infrared (IR) spectroscopy^[25] has been used to find the relationship between structural and growth synthons in crystal nucleation. The solid state structure of three organic acids (benzoic, tetrolic, mandelic) was used to assign the various functional groups. The solution spectra interpretation enabled the determination of composition and solvent. For benzoic and tetrolic acid a correlation was found between the growth synthon and the structural synthon.^[25] The third, mandelic acid, was more difficult to analyse unequivocally as strong solvent effects were reported. The outcome from this study showed that significant rearrangements occur within developing crystal nuclei.^[25]

Weissbuch et al^[26] attempted to modify the nucleation state with inhibitors and promoters. This additive-modified crystallisation was successfully probed with grazing incidence X-ray diffraction (GIXD) of a monohydrate cholesterol system, in which the GIXD technique probes approximately three monolayers at the surface. Analysis of the monolayer data allowed a link to be deduced between crystal formation and the nucleation state. The outcome of the study was a working hypothesis that the structure in the supersaturated solutions already resembled that of the final crystal structure.

Similarly, the already mentioned work by Spitaleri et al^[11] analysed a simple amide and a complex crystal system with ¹H NMR, attempting to gain insight during the early stages of crystallisation. They found that the technique was useful for probing possible solid state structures with solution data. The data from this study were further investigated using previously developed computational methods,^[12,27] simulating 3D structures for the two systems. However, the actual structure of the nucleation state could not be determined.

However, Jonkheijm et al^[28] probed and reported the varied structural changes that occur during the nucleation process of an organometallic compound. The self assembly of a π -conjugated system to a helical structure was analysed by circular dichroism measurements. This analysis revealed in depth the structures present during nucleation. Initially monomers formed dimers. When a minimum of ten dimers was present this

formed a so called pre-aggregate. The pre-aggregate was transformed via helix formation producing a nucleus of 28 dimers. Effects of solvent on the nucleation process were reported with solvent structure greatly affecting formation and stability of dimers and preaggregates. Where the solvent contained even or odd numbers of carbon atoms the temperature of helical formation was altered.

Actual computational simulations of the nucleation state are difficult because they require high levels of theory combined with computing power. Gavezzotti et al^[29,30] studied with success two systems: the aggregation of acetic acid and the crystal polymorphism of tetrolic acid. Hamad et al^[31] looked at solvent effects on the polymorphism of 5-fluorouracil with molecular dynamics. These simulations were carried out in three solvents: water, nitro-methane and wet nitro-methane. These simulations showed that water and nitromethane both produce form I, whereas dry nitromethane produced form II of fluorouracil. The simulations were very useful for determining the relative solvent-solute effects and hence polymorph formation.

Desgranges et al^[32] studied the relative molecular mechanism within polymorph selection during the nucleation of a colloid particle. Here molecular dynamic simulations showed that polymorphism can be controlled in a simple system. Alteration of the crystallisation conditions changed the stability of two possible polymorphs. The two crystallites follow different routes, polymorph selection occurs either in the nucleation state or during the growth stage. The study reports that selection via the growth state is highly complex and not fully understood.

Bolhuis et al^[33] and Dellago et al^[34] used high level algorithms to determine rate constants for various transition pathways, relating directly to the various transitions that are seen during and before crystallisation. The methodology involves studying transition pathways for unusual events in highly complicated systems. In comparison to previously mentioned dynamic approaches this method does not need transitions to be specified. Rather this method focuses on the sampling method of the transition state. This can then be analysed statistically.

1.3 Introduction to X-ray Absorption Spectroscopy (XAS)

The technique in the focus of this dissertation is X-ray absorption spectroscopy (XAS). To guide the reader through the introductory chapters a qualitative overview over the principles underlying XAS shall be given here. A more quantitative in-depth treatment

will be given in section 2.1 below. There are also several recommended books on XAS^[35-38] and a very instructive introduction recounting the interesting history of XAS.^[39]

In XAS analysis photon-induced excitations of core atomic electrons take place. Initially, when the X-rays impinge on the atom there is an interaction between the X-ray radiation and the bound electrons. The electrons either absorb the radiation and achieve an excited state or simply scatter the X-rays elastically or inelastically.

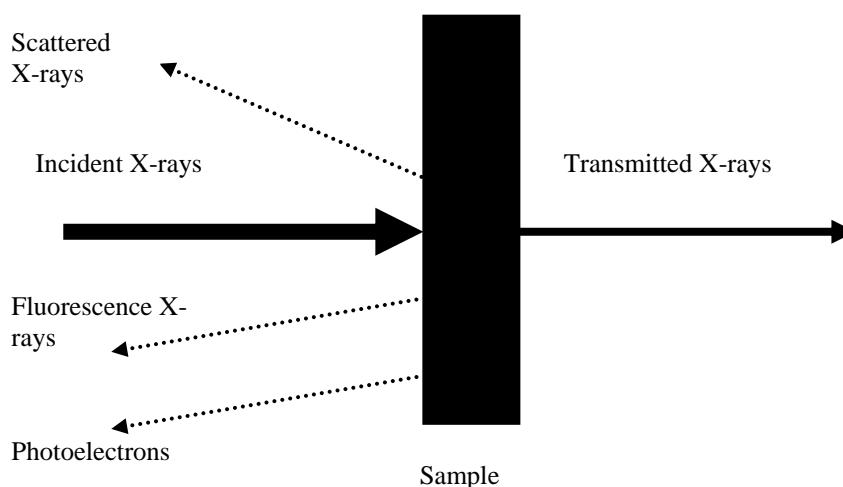


Figure 1 X-ray interactions with matter.

XAS measurements are carried out as a function of X-ray photon energy, always close to the characteristic core level binding energies of the elements. This feature makes XAS a unique and very valuable technique as it can distinctly probe the local electronic structure of many elements. If the X-ray energy is sufficient to excite an electron from an atomic core orbital, a jump in absorption coefficient occurs, which is called an absorption edge. To within about ± 5 eV the energetic position of the edges is characteristic the element analysed. The edge occurs when there is just the necessary amount of incident photon energy to excite a core electron from the atom. As an example, the Cu K-edge, which is due to excitation of Cu 1s electrons, at ~ 8990 eV is shown in Figure 2.

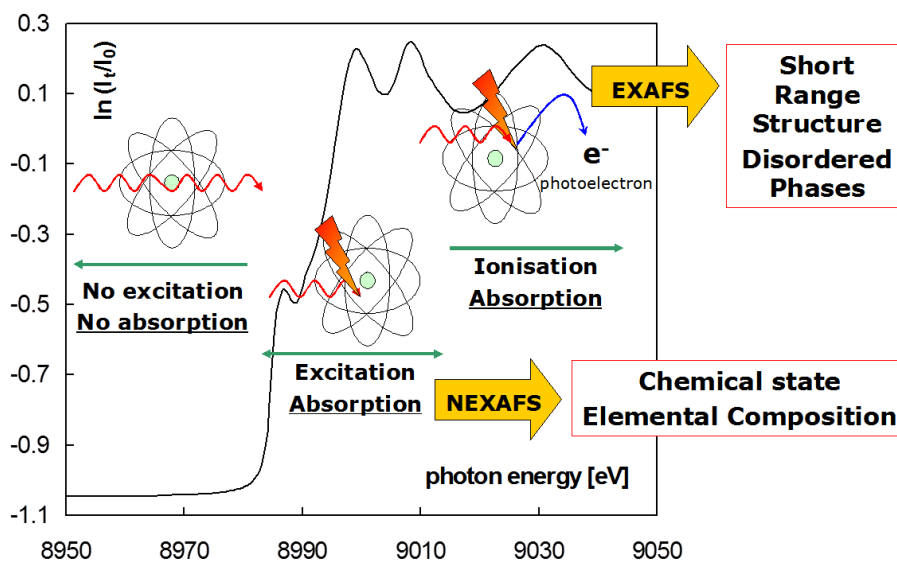


Figure 2 X-ray absorption K-edge of a Cu metal foil, underlying absorption processes and information that can be obtained from them; definition of NEXAFS and EXAFS region.^[40]

It can be seen that there are fine-structure features superimposed over the absorption edge, which are caused either by excitation of the core electron to an unoccupied atomic or molecular orbital, or, especially at energies above the ionisation potential (IP) of the atom, by backscattering of the photoelectron wave by surrounding atoms. These effects are called the X-ray absorption fine structure (XAFS).

The absorption edge spectrum is traditionally sub-divided into three specific regions, as seen in Figure 1. The pre-edge area, where no core excitation takes place, is usually smooth and featureless. The near-edge X-ray absorption fine structure (NEXAFS) region stems from electrons excited from the core level to unoccupied bound levels and multiple scattering of the resulting low-energy electrons. The NEXAFS region is often also called the X-ray absorption near-edge structure (XANES). The extended X-ray absorption fine structure (EXAFS) denotes the energy range from a few 10 eV above the absorption edge. It often extends up to ~ 1000 eV above the edge. The EXAFS is dominated by single scattering of the higher energy photoelectrons by neighbouring atoms.

1.4 Early research on liquid systems with X-ray absorption spectroscopy

The first publications on X-ray absorption spectroscopy (XAS) date back almost 100 years, to 1920.^[41,42] It was soon realised that the shape of the spectra arises from electronic transitions to unoccupied electronic states below the continuum threshold^[43,44]

and also from scattering of free photoelectron waves at neighbouring atoms.^[45-47] First suggestions for a theory of the extended X-ray absorption fine-structure (EXAFS) were made by Kronig^[43-45], for various molecules and crystalline solids. An application of this early theory was made by Hartree et al^[46] who successfully applied theoretical calculations to the EXAFS of GeCl₄. Further analysis utilising EXAFS soon followed in the 1930s. Various gaseous or solid structures involving Br, As, Zn, Hg, Xe and Kr were analysed.^[48,49] These papers merely reported their findings, making no clear comparisons between the states of the elements.

This was not the case for a study by Drynski and Smoluchowski^[50] comparing GeCl₄ in gaseous, liquid and solid forms. Here the first analysis of a liquid was carried out, by using a glass capillary. Experimental results demonstrated a significant difference between the solid, liquid and gaseous forms. The paper concludes that qualitative investigations clearly reveal differences between the states of matter, though improvements in theory would allow greater insight into the experimental results.

After these initial investigations major developments in analysis of liquids with EXAFS was not made between 1940 and the late 1960s. A hindrance was that there was no agreement as to how the EXAFS of solids could be interpreted quantitatively.^[39] Some research of merit was carried out by a group in Japan investigating amorphous systems. EXAFS of phases in the system nickel/sulphur were analysed for both amorphous and crystalline states.^[51,52] Results highlighted that the amorphous EXAFS showed similarity to the crystalline EXAFS, however the crystal EXAFS fine structure was more pronounced compared to the amorphous systems. Later in 1957 the same group reported on the EXAFS of crystalline and amorphous Ge.^[53] Comparing the EXAFS from both states the group suggests a diamond crystalline structure of Ge is found in the amorphous systems. This similarity was also reported by Nelson et al.^[54] Here comparison of three forms of GeO₂ was made hexagonal crystalline, tetragonal crystalline and amorphous. They state that the amorphous system has a high state of short range order which is identical to the hexagonal crystalline form. Both results support short range order theories indicating that short range interpretation of EXAFS was necessary. This interpretation was later confirmed by Brummer et al^[55] with the investigation of K₃[Fe(CN)₆] solutions.

A major breakthrough in the analysis of EXAFS was the investigation by Sayers et al.^[56] For the first time the EXAFS was analysed by application of Fourier analysis, showing that the radial distribution function of atoms around on the X-ray absorbing atom could

be recovered. This allowed significant information to be gleaned within a complex of different atoms such as: the number of neighbouring atoms, distances from neighbouring atoms and the number of local co-ordination shells. The technique was demonstrated on evaporated and crystalline Ge. The investigation found the distances between first and second neighbours to be within 1% of the known crystallographic distances. During this time in the 1970s a significant development in X-ray sources was made with the advent of synchrotron radiation sources, this allowed much improved spectra to be collected in a reduced time. For example, using a standard X-ray tube, analysis would typically take up to 2 weeks, whereas it is possible using synchrotron radiation to carry out the same analysis in 30 min. The advantages were demonstrated by Kincaid and Eisenberger with synchrotron studies of Kr, Br₂ and GeCl₄ in the gas phase.^[57] Measurements taken using the synchrotron radiation from the SPEAR storage ring at Stanford benefitted from a 5×10^4 fold improvement in X-ray intensity compared to previously used X-ray tube sources. Comparing theory plots of Br₂ and GeCl₄ EXAFS against experimental plots highlighted that the theory prediction of the amplitude was around a factor of 2 larger than the experimental value. Also there was a difference in the theoretical peak positions compared to the experimental results; this error was reported to be 5%. The paper concluded that theoretical approaches were not sufficient to allow a quantitative agreement with the data collected using the synchrotron source. The same authors then also established the application of synchrotron radiation to the analysis of aqueous solutions,^[58] measuring the EXAFS of Cu²⁺ and Br⁻ ions in aqueous solution. Due to the element selectivity of X-ray absorption spectroscopy (XAS) the ions could be characterized separately in dilute aqueous solutions. Similar solvation studies were reported for aqueous Ni²⁺ solutions.^[59] Here high resolution XAS were acquired for Ni(NO₃)₆·6H₂O salt and its 0.1M aqueous solution. Analysis of the EXAFS followed a Fourier transform method reported by Stern et al.^[60] The first and second spheres of coordinated water molecules to Ni²⁺ were clearly observed in the Fourier transform and nearest-neighbour distances were determined. Extended X-ray absorption fine structure was also reported for NiCl₂ aqueous solutions at 2.7 and 3.7M to examine the concentration variations in the structure around the Ni cations,^[61] for which indications had previously been found by neutron diffraction^[62] and Raman spectroscopy.^[63,64] EXAFS compared to neutron diffraction has several advantages in this application as neutron analysis is sensitive to deuterium and hydrogen and less sensitive to Cl,^[65] while EXAFS does not detect deuterium or H and is sensitive to Cl. So the Ni²⁺ ion and its

surrounding O and Cl atoms in solution can be easily interrogated with EXAFS. The subsequent EXAFS of Ni^{2+} solutions confirmed the neutron diffraction data, with Ni^{2+} ions being coordinated to six water molecules at a distance of 2.07 Å. Further to this, the analysis confirmed an outer sphere of 3 Cl^- atoms at a distance of 3.1 Å, for which evidence had previously been reported by neutron diffraction.^[65] Oddly, no support was found for first sphere halogen co-ordination, which had been observed around the same time by EXAFS for concentrated aqueous CuBr_2 solutions,^[66] for which the analysis indicated significant local ordering with a rectangular coordination of Cu by Br, linked to each other to form a chain assembly. The absence of coordination by halogen in the NiCl_2 study was later shown to be an interpretation error.^[67] The CuBr_2 analysis also revealed a higher level of disorder compared to the crystal structure that increases when lowering the solution concentration. Even at low concentrations around 0.1M there is a degree of assembly with over half the Cu and Br ions forming a plane square molecule. The analysis supports the application of EXAFS analysis over a wide range of concentrations.

Further research on solutions of CuBr_2 , ZnBr_2 , NiCl_2 and NiBr_2 confirmed significant association of ions in solution at higher concentrations.^[67] To test the effect of water on the local order of molecules in concentrated solution the temperature was varied for analysis of CuBr_2 and ZnBr_2 , between room temperature and 75°C. It was expected that the effect of water on local order would be less pronounced at higher temperatures. The raw data presented for ZnBr_2 for the solid, saturated solution and dilute solution, revealed a similarity between the solids and the saturated solutions, confirming local order of ion at concentrated solution. The temperature-dependent studies reveal distinct conclusions for CuBr_2 and ZnBr_2 . For CuBr_2 solutions the high energy (~150 eV-300 eV) range of the EXAFS showed little difference, while the low energy (~0eV-150eV) range varied distinctly as a function of the degree of hydration: its amplitude reduced from high temperature 75°C to low temperature 21°C. This observation supported the expected reduction of the hydration number with an increase in temperature, though it was noted that the amplitude reduction was not constant over the temperature range, but particularly strong around 60°C. The temperature results for ZnBr_2 showed no clear results linking spectral changes to the change in temperature: the EXAFS for low and high temperatures almost exactly matched over the whole photon energy range.

Early studies on metallic liquids were made by Petersen and Kunz^[68,69] who investigated Na, Al and Li with soft X-rays at the L and K edges. Experiments were conducted in

ultra-high vacuum using partial photoelectric yield as a suitable method of attaining a signal directly related to the absorption coefficient. Further development of inorganic melts were added by Crozier et al who used XAS to interrogate the liquid semiconductor As_2Se_3 and liquid Zn.^[70] This paper highlights that during data analysis any asymmetric atom distribution will require consideration. The methodological requirements were later summarized in a review by Crozier.^[71]

Many scientific areas have over the last three decades strongly benefitted from the application of EXAFS to solutions, melts and glasses, including chemistry, physics, biology and earth science. Due to the wide interest this has led to XAS techniques being developed further both theoretically and experimentally. Only a few examples of such work shall be highlighted here.

1.5 Specialised cells: investigations of liquid systems under extreme conditions

For example, instrumental developments have been made for permitting the analysis of samples under extreme temperatures and pressure. The sample cells used in early experiments were quartz cells in form of a sealed capillary.^[50] Today for conventional liquid analysis two types of methods are used.^[72,73] First, closed cells are used that contain the sample between two windows. Second, an inert matrix of powder, glue or wax is dispersed within the sample and then melted; this method be used for low melting point metals or powder mixtures. The benefits of both methods need to be evaluated against certain criteria, sample stability during phase transitions, density changes of sample and resistance to contamination. Taking the first issue, a closed cell would not allow for phase changes resulting in increased pressure and possibly a broken cell. However, the inert mixture would allow for a phase change to take place with no negative consequences. The second issue for a closed cell can be certain experimental conditions where a change of density can result in spectra with a higher degree of noise. Sample density changes do not affect an inert matrix as the volume will remain constant, independent of any sample density changes. On the other hand, contamination is less likely contained in a closed cell compared to a dispersed sample in an inert medium that can be contaminated.

For standard experimental conditions using aqueous solutions cell designs usually do not present any significant issues. If analysis needs to be carried out under pressure a cell design must be used that can withstand such pressures. Examples for the use of such cells

have been solution studies up to 350°C^[74] and in supercritical water.^[75] By development application of droplet techniques higher melting point liquids have become accessible and more metallic liquids have been studied with EXAFS.^[73,76-80] ESXD (energy scanning X-ray diffraction) analysis is often combined with EXAFS analysis to ensure that the undercooled liquid is not crystallised and/or to probe the long-range structure of the system.

Aqueous solutions, specifically local environments of solute species, have been investigated with X-ray techniques; this is due to the simple experimental setups employed for XAFS with hard X-rays. A complete review of such application in addition to the references already cited in section 1.4 would go beyond the scope of this thesis, but a few examples shall be given.

An example of investigations applying molecular dynamic simulations to interpret structural changes were carried out by D'Angelo and co-workers.^[81-84] The analysis of ions and molecules in supercritical water has also been an active area of investigation from the chemical and physical perspective. This is challenging as a hydrothermal experimental state has to be attained in the laboratory. Investigations of ions have progressed from early studies adopting single shell fits with Gaussian disorder to more realistic fitting models using cumulant disorder models, to finally following a molecular thermodynamic approach based on molecular dynamics. Experiments have included a wide range of ions, e.g., Sr²⁺,^[75] Rb⁺,^[85] Br⁻,^[86] Ag⁺,^[74] Sr²⁺,^[87] and Ni²⁺.^[88]

Noble gases have a water solubility minimum at about 80°C that has led to several XAS investigations. Because noble gases have minimal solubility in water these small effects have eluded other experimental investigations until the application of XAS. Known thermodynamic effects of noble gases in solution at low temperature indicate the possibility that the presence of noble gases increases the order of the water association.

The first attempt to examine Kr in H₂O was made using supercritical water,^[75] but no signal from Kr-O interactions was found. The first recorded Kr-O interactions were obtained by pressurising Kr in water at 10 MPa. The Kr-O coordination could be analysed resulting in the determination of the first short range radial distribution function.^[89,90] Temperature-dependent experiments to about 80°C at both the Kr and Xe K-edges revealed a dramatic temperature dependence of the EXAFS that implied a strong disordering of the hydration shell in this temperature range, thus providing the first microscopic structural basis for the understanding of the solubility data.^[89] Using both

temperature and pressure control a solid clathrate structure was examined and compared to the Kr environment in the liquid.^[91]

1.6 Organic molecular solutes and solids: a new field for soft X-ray core level spectroscopies

In spite of the early historical application of EXAFS to molecular liquids^[50] the studies of molecules in liquid systems, especially organic molecules, are still largely unexplored. Barely any studies at all relate to the crystallisation science of molecular solutes.^[2] A reason for the scarcity of studies in this area is that intramolecular interactions often dominate over intermolecular interactions, which limits the sensitivity to intermolecular structure. This makes both molecular liquid spectra and vapour spectra very difficult to distinguish as they tend to give similar spectra. Although these similarities are present EXAFS analysis can have remarkable sensitivity to molecular structures, even down to 0.001 Å.^[92] This allows detection of even very small changes in the molecular structures between different phases.

The main difficulty faced by studies of liquid systems containing organic solutes and of most organic solids has arisen from the soft photon energy range ($E < 1000$ eV) in which the absorption edges of the most relevant absorbers, C, N, and O, occur. Experiments with photons in this range have traditionally required ultra-high vacuum chambers. As a result, NEXAFS has played a pivotal role in the elucidation of the electronic structure and atomic-scale morphology of ultra-high vacuum-compatible systems, such as adsorbate-covered surfaces, thin films and highly dispersed materials. However, samples with a vapour pressure above $\sim 10^{-6}$ mbar could not be investigated in such systems, preventing NEXAFS from being applied in studies of liquid solutions, melts and many organic solids.

Technical developments since the late 1990s have begun to transform NEXAFS from a pure UHV technique to a routine probe that can also be employed at pressures closer to 1 atm. These developments were paralleled and, in part, inspired by the development of high-pressure X-ray photoelectron spectroscopy (XPS) with synchrotron radiation, which primarily took place through the development of applications in the field of heterogeneous catalysis^[93] and for studying liquid water condensation in controlled humidity chambers.^[94,95]

XPS is intrinsically surface sensitive because it relies on the analysis of the elastic peaks associated with the emission of X-ray induced photoelectrons, which have a limited penetration depth in condensed matter before undergoing inelastic losses. In contrast, NEXAFS can be performed with either surface or bulk sensitivity by selectively monitoring the emission of electrons, particularly total and partial electron yields, or X-ray fluorescence.^[35,38,96-98] Electron detection techniques are preferred when the X-ray absorbing element of interest is present in high concentrations.^[96,99,100] Fluorescence detection is more suited to the characterization of samples containing the element of interest in dilute form.^[35,38,96-98,101] More recently, UV emission and optical fluorescence/luminescence associated with the decay of the X-ray induced atomic core holes have also been introduced for monitoring the bulk absorption coefficient,^[102,103] while differential surface charging has been exploited for Kelvin probe XAS surface microscopy with near atomic resolution.^[104,105] Recent developments in soft X-ray spectromicroscopy have been reviewed by Yoon.^[106] In this review, recent developments and applications of soft X-ray spectromicroscopy, with a focus on scanning transmission X-ray microscopy (STXM), are described.^[106]

The efficiency of indirect NEXAFS detection methods has been steadily improved over the last decades, and construction of 3rd generation synchrotron X-ray sources with higher photon flux and brilliance have permitted their use in non-vacuum environments: counting statistics are sufficient even when the path through the gas phase reduces the incoming X-ray beam intensity by one or two orders of magnitude.

The NEXAFS structure traces the unoccupied density of states below the ionisation threshold of the probed atoms. In the early days of NEXAFS spectroscopy^[38,97] curve-fitting was often applied to identify the energetic positions of electronic transitions and to resolve the position of the ionization potential, which is identical to the energy of the corresponding elastic photoelectron peak in XPS.^[38] The dependence on the polarisation vector of the synchrotron light can be employed to determine the angle at which ordered organic adsorbate layers with π electron systems are oriented relative to a surface plane,^[38] while the position of the σ^* shape resonance in the spectra allows the determination of bond lengths.^[107]

Since the 1990s, *ab initio* packages like StoBe^[108,109] and FEFF^[110-113] have begun to allow calculations of the complete absorption spectra using detailed structural models generated by computational chemical packages, molecular modeling or plausible trial and

error structures. Progress in the theory underlying the electronic structure calculations has been reviewed by Rehr^[114-116]. These methods allow to compare model structures with experimental data. This is the approach that will be taken in the present work.

The present study was enabled by the development of instrumental solutions for performing NEXAFS and XPS measurements under non-vacuum conditions. Dedicated spectrometer vessel design permits investigations of liquid samples through liquid jet techniques^[117] as well as by use of humidity and liquid chambers.^[118-120] These systems have in recent years facilitated XPS and NEXAFS studies of solvent structure,^[121-135] vapor/solution interfaces^[136-141] and solution species.^[142-156]

Early examples dealt mainly with the chemical state and the coordination around inorganic element ions in solutions. For example, NaCl electrolytes have been studied with soft XAS from 0.1M to 5M.^[157] The results showed that Debye-Hückel theory allows a description of phase behaviour only for concentrations up to approximately 0.1 mol L⁻¹. To understand the experimental results of solutions with higher concentrations StoBe-Demon^[158] modelling was carried out. Various Na⁺ environments were modelled by systematically evaluating varying Na-Cl and Na-water distances. These calculations allowed comparisons to be made between the theoretical and experimental NEXAFS. Ultimately the origin of the spectral fingerprints could be elucidated by linking with structural models, which revealed that over the 1M to 5M concentration ranges the Na⁺-Cl⁻ distance decreased, suggesting the formation of ion pairs.

In another study^[159] the hindrance associated with ion-ion interactions in NaI electrolytes was investigated. The XANES of NaI was examined comparatively, once in ethanol and once in water. StoBe^[158] was again used to correlate structural models with the experimental spectra. The molecular orbitals were analysed for each solvent system, and a sensible match was found for the spectral features and respective molecular orbital. A good correlation between the experimental and calculated data was found when significant effects of cation-anion interactions in the water based system were taken into account, while similar conclusions were not possible for the structure in ethanol.

There have been much fewer studies of organic molecular solutes in solution so far, and mostly with XPS. These studies have addressed (i) aqueous solutions of lysine,^[160] for which it was shown that the core levels allowed following the pH-dependent protonation state of the molecule in solution and (ii) imidazole solutions.^[145-147] These imidazole studies formed the basis for the work presented in this thesis and will therefore be

summarised in detail in the next section. Very recently, the NEXAFS of aqueous formic acid and formate solutions was reported,^[161] showing that care has to be taken in the interpretation of NEXAFS because of a complex interplay between initial state and final state effects as a function of the protonation state in this system. Recent XPS work on organic co-crystal phases in our group has shown that the core level binding energies are a highly incisive probe for elucidating hydrogen bonding and proton transfer between Brønsted donors and acceptors,^[162-166] in line with the abovementioned XPS results^[145-147,160] for lysine and imidazole solutions. This suggests strongly that XAS of solution species will provide similar insight into the balance between hydrogen bonding in non-ionic molecular solute systems.

1.7 1*H*-Imidazole and its solutions

1.7.1 Properties of 1*H*-Imidazole

1*H*-imidazole (Figure 3) has the sum formula $C_3N_2H_4$ and a molecular mass of 68.08 g mol⁻¹. It has a melting point of 89-91°C (362-364 K) and a boiling point of 256°C (529 K). The IUPAC numbering of the ring atoms is indicated in Figure 3.

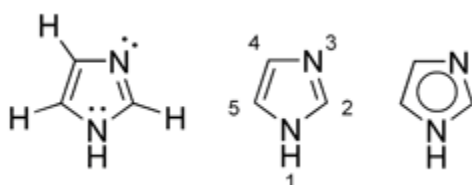


Figure 3 Three different chemical representations of 1*H*-imidazole; note the IUPAC numbering of the ring atoms in the centre formula.

For the remainder of this dissertation the term ‘imidazole’ will be used interchangeably with its correct full IUPAC name, 1*H*-imidazole.

The mass density of solid imidazole is 1.23 g cm⁻³, corresponding to 18.07 mol L⁻¹ of solid. Its crystal structure has been obtained using X-ray diffraction analysis at room temperature by Will^[167] and at -150°C by Martinez-Carrera.^[168] Neutron diffraction analysis has been carried out at 20 and -150°C as well.^[169] From these studies it is well established that imidazole has a monoclinic crystal structure with the space group $P2_1/C$. There are four molecules in the unit cell. The main structural feature is the presence of infinite chains of hydrogen-bonded imidazole molecules along the *c*-axis (Figure 4).

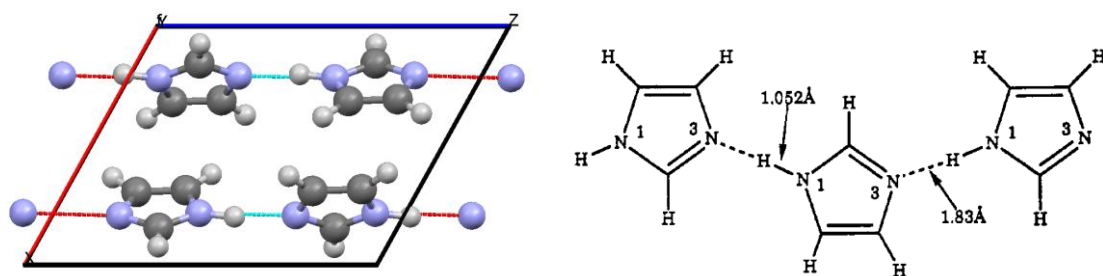


Figure 4 Cut-out from the unit cell of the imidazole crystal structure, indicating the motif of hydrogen-bonded chains. The sketch on the right^[170] indicates the length of the N-H donor and H...N acceptor bonds.

The analysis of solid imidazole with low frequency Raman spectroscopy was reported in 1968.^[171] The paper added to an analysis previously carried out by Zimmermann^[172] which has left four low frequency bands unassigned. The paper highlights the strong hydrogen interactions found in the imidazole crystal lattice. The analysis method,^[173-175] indicated that certain modes became more apparent due to the strong hydrogen bonds formed in the imidazole crystal lattice, in line with previous reports.^[176-178] It was noted that the splitting between symmetrically and anti-symmetrically coupled vibrations is particularly high in presence of strong hydrogen bonds. Further IR and Raman analysis on ¹⁵N- and D-substituted imidazoles have also been carried out.^[179] The analysis highlights a broad band with some fine structure between 3300-1800 cm⁻¹ due to NH(D)-N stretching vibrations.

Two decades later, a study of imidazole and imidazolium with ultraviolet (UV) and Raman spectroscopy was undertaken, which provided greater insight into the excitation mechanisms.^[180] The investigation reports that as excitation energies reach 190-220 nm the vibrational modes are significantly enhanced. This electronic-vibrational excitation study provided a more incisive avenue towards elucidating the functional contribution of histidine in proteins.

Considerable attention over the decades has been paid to the proton conductivity of solid imidazole, which has been examined numerous times because it was believed to follow the Grotthus mechanism.^[181] For example, ¹⁵N NMR studies were carried out to shed light on this issue. The results did not lend support for a Grotthus mechanism,^[181-183] though other methods of charge tunnelling were not ruled out. The system was studied *ab initio* early on as well, for example using MNDO and Gaussian-76.^[184] This analysis then

laid foundations to unravelling the mechanisms involved in the proton exchange that may take place in aqueous solution. The study concluded that intermolecular hydrogen exchange was energetically favourable.

In aqueous solutions imidazole can establish two Brønsted equilibria, with pK_a values^[185,186] of $pK_{a1} = 7.05$ and $pK_{a2} = 14.52$ (see section 2.2 below for a more quantitative details).

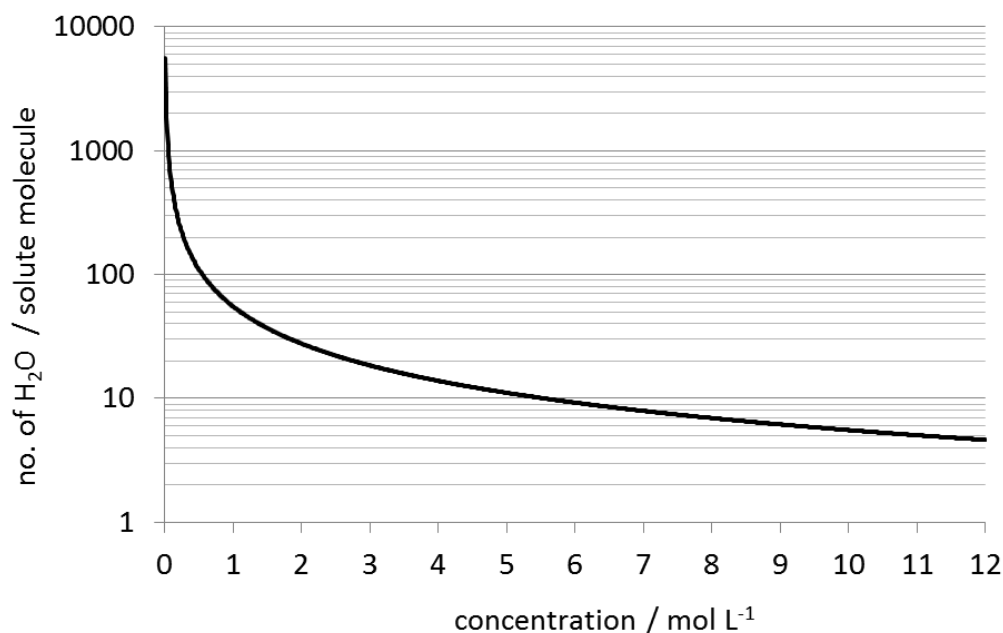


Figure 5 Number of water molecules available for hydration of a solute as a function of the concentration of the solute in water.

The solubility of imidazole in water is very high. Concentrations up to 11.18 mol L^{-1} can be achieved.^[187] It must be remembered at such high concentrations the availability of hydrating molecules becomes limited, leading to non-ideal behaviour with likely ordering of the solvent and intermolecular interactions (self-association) between solute molecules. The dependence of water molecule availability on concentration is quantitatively illustrated in Figure 5. It can be seen that at concentrations above $\sim 5.5 \text{ mol L}^{-1}$ the number of available hydrating molecules per solute molecule drops below 10, reaching a value of ~ 5 at the saturation concentration of imidazole. It is expected that such solutions exhibit association structures with solute-solute, solute-solvent, and solvent-solvent interactions that would not be observable in their corresponding ideal solutions. The self-association processes taking place in aqueous imidazole solutions have therefore attracted the interest of researchers for many decades.

This has led to numerous investigations, some of which will be summarised in the next section.

1.7.2 Self-Association in Imidazole Solutions

The self-association in aqueous imidazole solutions has been studied since early work by Hückel and co-workers investigated its physical properties.^[188] A critical review of early self-association studies and general formulae for the mathematical treatment of possible relevant equilibria were given by Wolff.^[189] The importance of hydrogen bonds in the self-association of imidazole solutions was recognised early on, for example for carbon tetrachloride,^[190] and led to NMR investigations already in the 1960s.^[172,191-194] Since then the system has always attracted attention because of its participation in intramolecular hydrogen bonding as the side group in the amino acid histidine, which plays an important role in enzyme catalysis. A study of acetyl histamine and methyl dihydrourocanate using IR spectroscopy^[195] highlighted that imidazole may contribute to protein hydrogen bonding.

The first IR analysis and assignment of imidazole vibrations was undertaken by Otting.^[196] The analysis highlighted several key trends for imidazole at various concentrations in chloroform solution. The strong absorption of the non-bonded NH moiety decreased in intensity as the imidazole concentration was increased, indicating self-association. In line with this, a concomitant increase of the absorption from the bonded NH moiety with concentration was found. The degree of self-association was also evident through IR investigations of carbon tetrachloride solutions.^[190] It was concluded that chains of imidazole oligomers were formed as the concentration increased: the N-H band at 3000 cm^{-1} became more apparent while a reduction was noted at 3500 cm^{-1} for the NH band assigned to the free end groups of the imidazole oligomers.

IR studies of the NH stretching vibration of imidazole in the non-polar solvents benzene and carbon tetrachloride were more recently carried out by Pralat and Czechowski.^[197] From the temperature-dependent analysis of the extinction coefficients the authors concluded that a high degree of self-association occurs through strong hydrogen-bonding already at concentrations as low as $2 \times 10^{-3}\text{ mol L}^{-1}$ in both solvents.

¹H NMR of imidazole solutions in chloroform were performed by Wang et al.^[198] Chemical shifts and the temperature dependence of the spectra indicated that imidazole

predominantly exists as a trimer in chloroform solutions. ΔG° , ΔS and ΔH values for trimerisation at 300 K were reported as -8.4 kJ mol^{-1} , $-15 \text{ J K}^{-1} \text{ mol}^{-1}$ and $-13.0 \text{ kJ mol}^{-1}$, respectively.

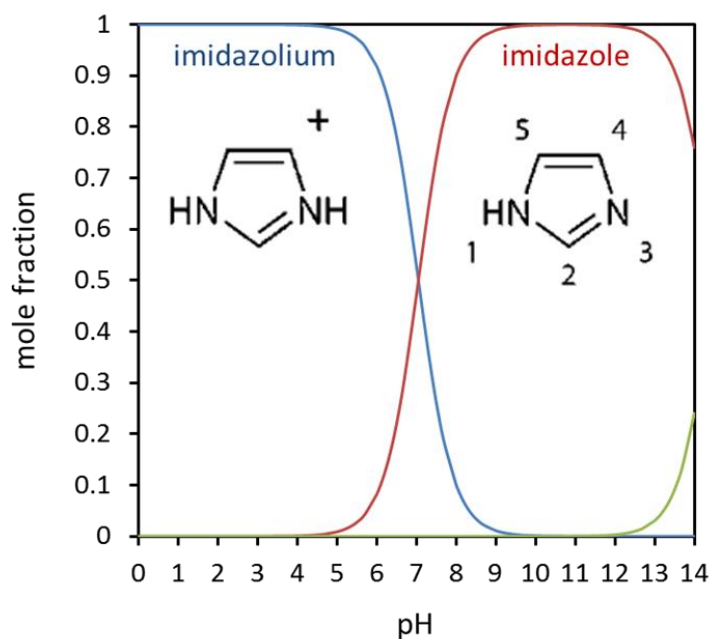


Figure 6 Imidazole speciation in aqueous solution as a function of pH, calculated from pK_a values as described in section 2.2.2.

The speciation of imidazole in aqueous solution as a function of pH can be predicted from the well known pK_a values. The mathematical basis of this calculation will be given in section 2.2. Figure 6 gives the result. It can be seen that the protonated species, the imidazolium cation, dominates at pH values below approximately 5.5, while the neutral unprotonated imidazole species predominates in the pH range between approximately 8.5 and 12.5. Above a pH of approximately 13 deprotonation of the 3N position should become noticeable, resulting in the formation of an anionic species.

The most incisive previous studies of the nature of imidazole self-association in aqueous solutions have been carried out at low concentrations with UV-vis spectroscopy^[199] and at high concentrations by radial distribution function analysis using X-ray scattering.^[200]

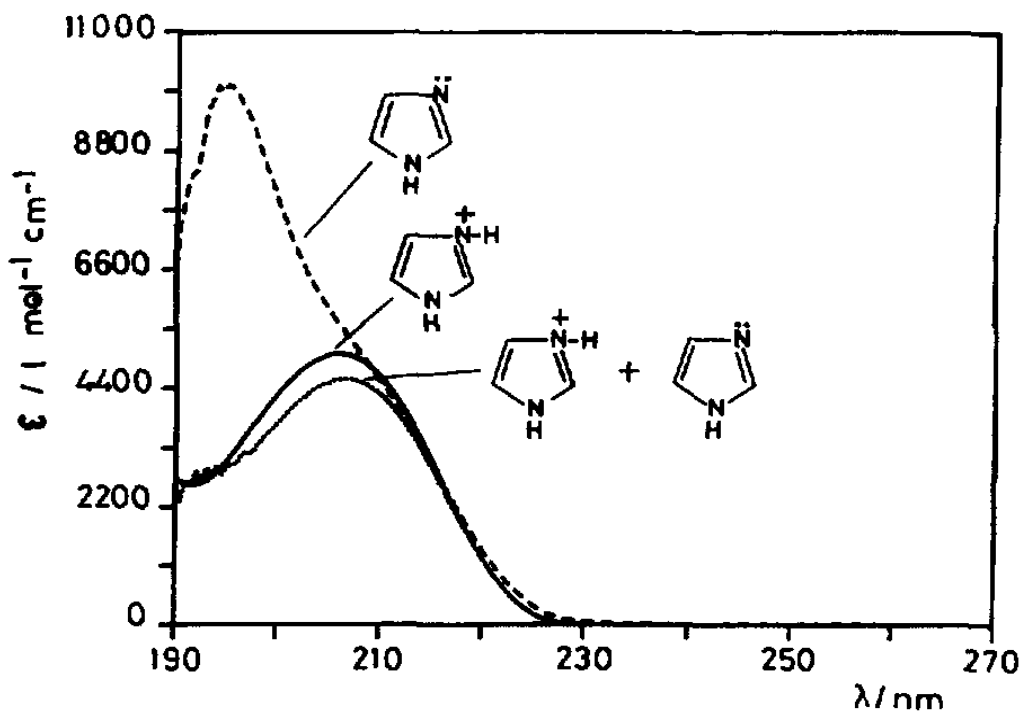


Figure 7 UV absorption spectra of imidazole in aqueous solution:^[199] 1.006×10^{-4} at pH = 3.2 (—); 1.025×10^{-4} M at pH = 6.9 (...), and 1.032×10^{-4} M at pH = 11.0 (---).

The UV study examined imidazole and some of its derivatives with concentrations varying from 5×10^{-6} to 2×10^{-1} M, at three pH values. At pH = 3.2, where imidazolium predominates (Figure 6), at the near-neutral pH = 6.9, where imidazolium and unprotonated imidazole coexist in a 50:50 ratio (Figure 6), and at a pH of 11.0, where the neutral unprotonated imidazole species predominates (Figure 6). Clearly detectable differences in the respective UV-vis spectra were observed (Figure 7).

It can clearly be seen that there is a band at 205 nm that predominates in neutral and acidic pH, whereas at basic pH there is a strong absorption at 195 nm. It was suggested that the 194 nm band corresponds to $n-\pi^*$ transitions and the band at 205 nm to $\pi-\pi^*$ transitions. To explain the differences seen for the representative transitions and bands the key point to note is the disappearance of the $n-\pi^*$ band at acidic pH. In an attempt to better understand this observation further, the $n-\pi^*$ transitions analysis was also done in a non-polar solvent (hexane), which should only be able to stabilise neutral species.

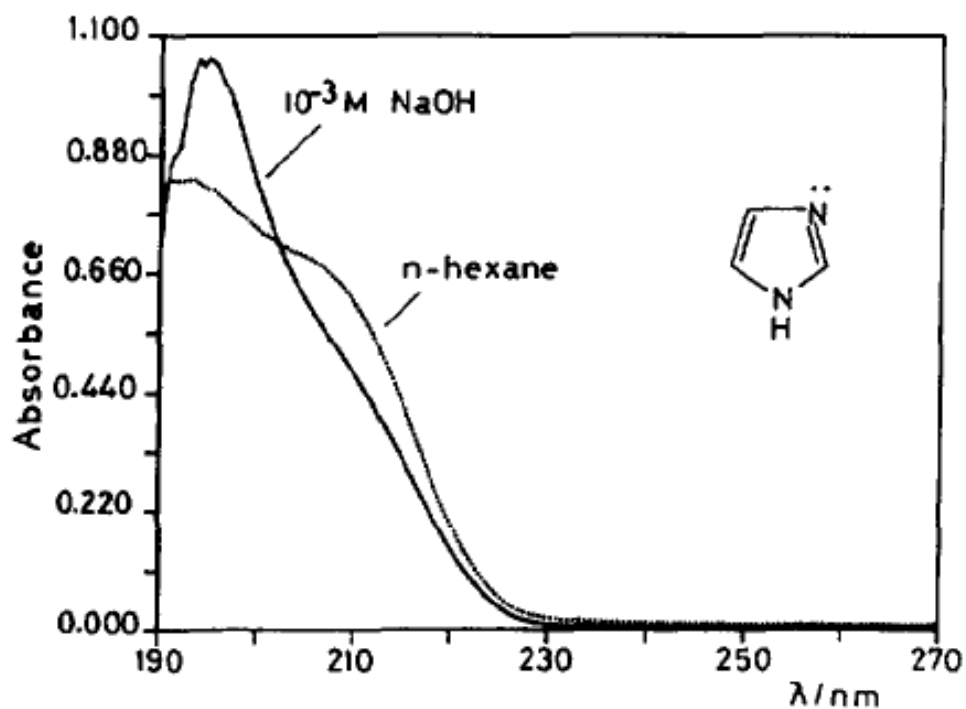


Figure 8 Solvent effect on UV absorption spectra of imidazole:^[199] $1.032 \times 10^{-4} \text{ M}$ in NaOH at pH = 11.0 (—) vs. saturated solution in n-hexane (...).

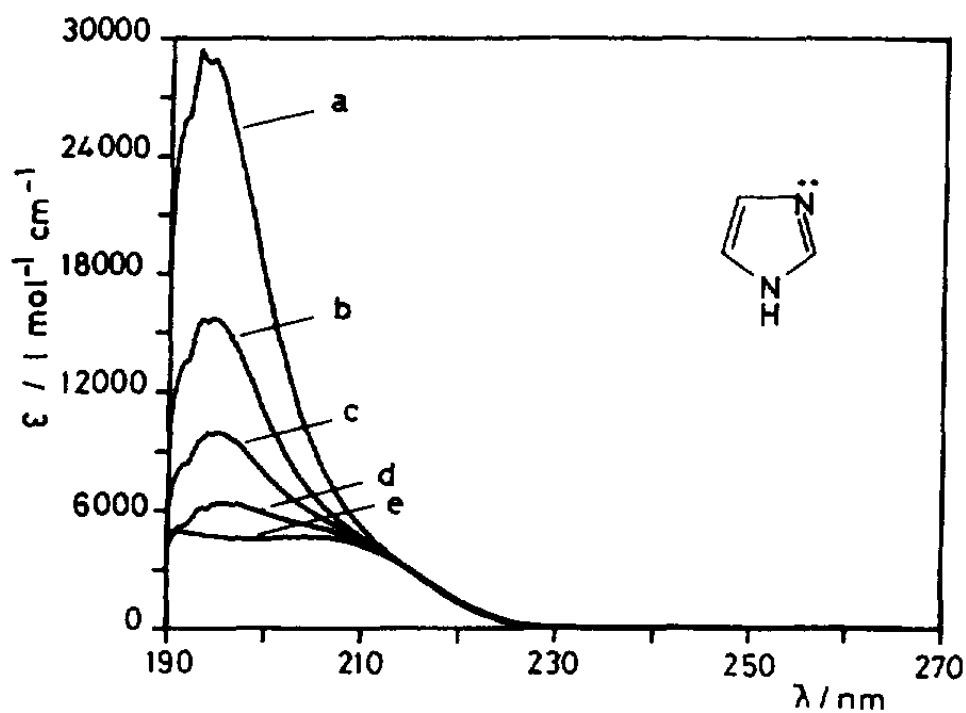


Figure 9 Hypochromic effect in UV spectra of aqueous imidazole solutions in the concentration range from $5 \times 10^{-5} \text{ mol L}^{-1}$ to $5.1 \times 10^{-4} \text{ mol L}^{-1}$.

Measuring in n-hexane increased the resolution between the two transitions of the neutral species (Figure 8), but did not allow a full separation. The spectra for n-hexane revealed a slight inflection at 211 nm and a shift of the band at 194 nm towards 192 nm. What is clear from the difference between the absorption spectra is that the neutral species in water is significantly electronically influenced relative to that in n-hexane.

The authors also examined the effect of concentration on the spectra in an attempt to determine the self-association equilibrium constant; in line with self-association an increase in concentration produced an increase in hypochromic effects (Figure 9), which is in line with observations reported previously for solutions in benzene and CCl_4 ,^[197] and in chloroform.^[198] The authors determined self-association constants for dimeric and polymeric species and found that neutral solutions, where neutral imidazole and cationic imidazolium coexist in an approximate 50:50 ratio, had an extremely high propensity to dimerisation, with a dimerisation constant K_2 of $\sim 10^9 \text{ L mol}^{-1}$ and a polymerisation constant K_n of $\sim 1 \text{ L mol}^{-1}$. The basic solution, in which neutral imidazole molecules predominate, was much more prone to polymerisation ($K_n \sim 2 \times 10^3 \text{ L mol}^{-1}$) while also exhibiting a moderate dimerisation constant of $K_2 \sim 3 \times 10^4 \text{ L mol}^{-1}$. The authors proposed that the observed behaviour in basic solution was in line with a stack model incorporating both H-bonding and π - π interactions, as reproduced in Figure 10.

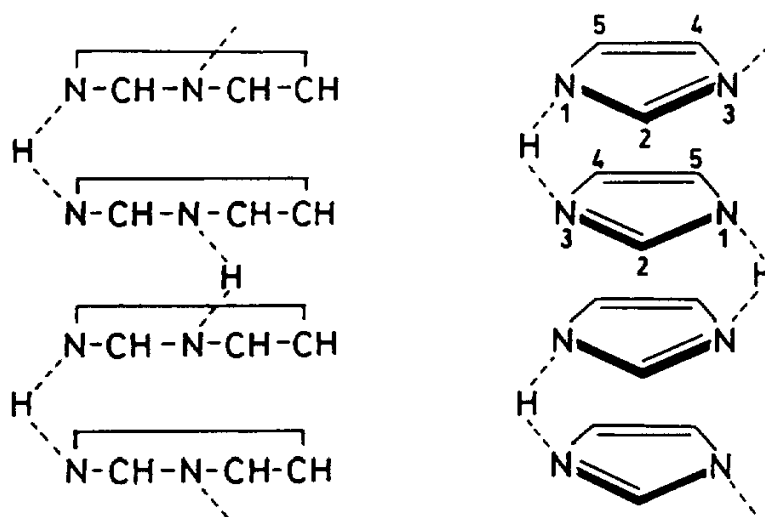


Figure 10 Structural model for the self-association of imidazole in basic aqueous solutions as proposed by Peral and Gallego.^[199]

Gontrani et al analysed concentrated (4.5M and 7.6M) aqueous imidazole solutions by energy-dispersive x-ray diffraction (EDXD).^[200] The pH was not adjusted, suggesting that the solutions had a pH of approximately 10.7 (see Figure 11 below) and were dominated by neutral imidazole species. Structural and radial distribution functions for water and imidazole solutions were reported. The distribution functions allowed peak assignment to various atom-atom distances; these are summarised in the tables below.

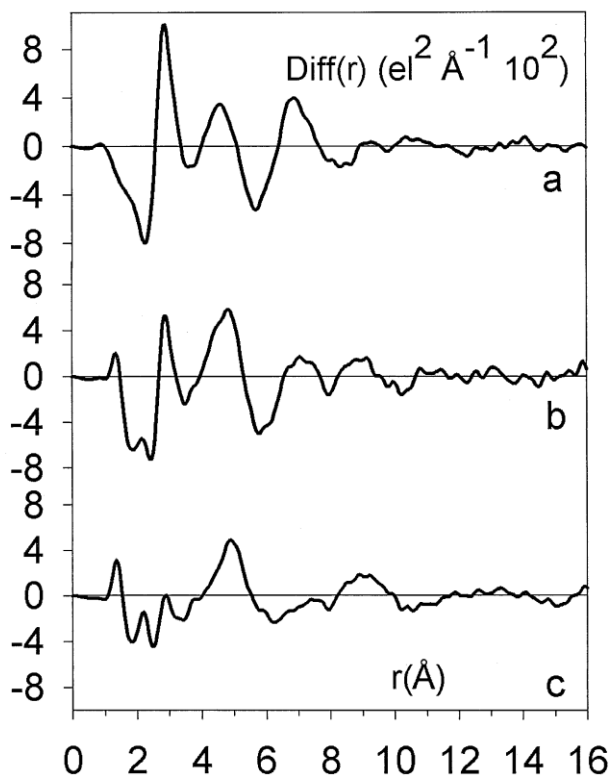


Figure 11 Experimental radial distribution functions for (a) Pure water, (b) 4.5 M aqueous imidazole, (c) 7.61 M aqueous imidazole.

This analysis importantly allows the peaks at 4.85 Å and 9 Å in the imidazole radial distribution function to be assigned to solute-solute and solute-solvent interactions. Using these data a structural model was developed to reproduce the experimental pair-distribution data. A wide range of geometric water/imidazole arrangements were tested (planar dimers, linear polymers etc) in an attempt to determine a likely solution structure. Best agreement was found for imidazole forming bent polymeric stacks, similar to those proposed by Peral and Gallego (Figure 10). This structure is reproduced in Figure 12. The centres of mass of neighbouring imidazole molecules are approximately 3.7 Å apart. Each imidazole molecule is coordinated by water molecules, which are hydrogen-bonded

to the N moieties, with $3\text{N}\dots\text{H}_2\text{O}$ and $1\text{NH}\dots\text{OH}_2$ distances of 2.78 Å and 2.85 Å, respectively.

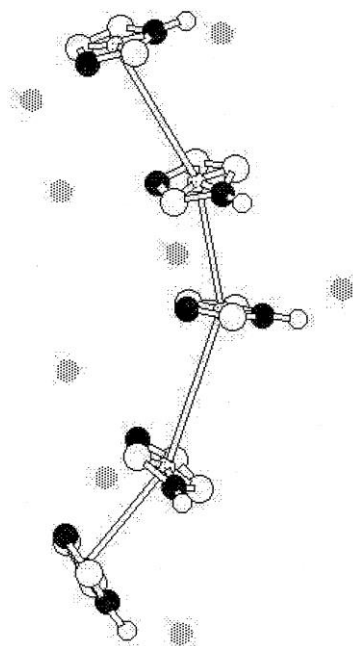


Figure 12 Bent stacked imidazole structure model for concentrated aqueous solutions (4.5M and 7.61M) as deduced from radial distribution functions determined by EDXD.^[200]

RDF Peak	Interpretation
0.95 Å	O-H contacts within the molecule
2.85 Å	O...O contacts between first neighbour molecules
4.65 Å	O...O contacts between second neighbour molecules
6.9 Å	O...O contacts between third neighbour molecules

Table 1 Radial distribution function peak assignments for water.^[200]

RDF Peak	Interpretation
1.35 Å and 2.15 Å	Interactions between adjacent atoms in the ring and atoms across the ring of the Imidazole molecule
4.85 Å	Water peak, slightly shifted

Table 2 Radial distribution function peak assignments for concentrated aqueous imidazole solutions.^[200]

It is interesting to note that both the UV-vis study of dilute solutions^[199] and the EDXD work on concentrated solutions by Gontrani et al^[200] led to an interpretation in terms of a

stacking model of imidazole molecules. This is different from the structural motif hydrogen-bonded chains of molecules found in the solid state of pure imidazole (see section 1.7.1) as well as in its melt.^[201] The possibility of chain structures was therefore recently reinvestigated in a molecular dynamics study of Liem et al.^[202] Who examined the structure of neutral aqueous imidazole assemblies at high concentrations. In line with the results of the two experimental studies the simulations do indicate the existence of self-associated stacked structures, but an increasing amount of chain-like assemblies are found as the concentrations are increased towards saturation (Figure 13).

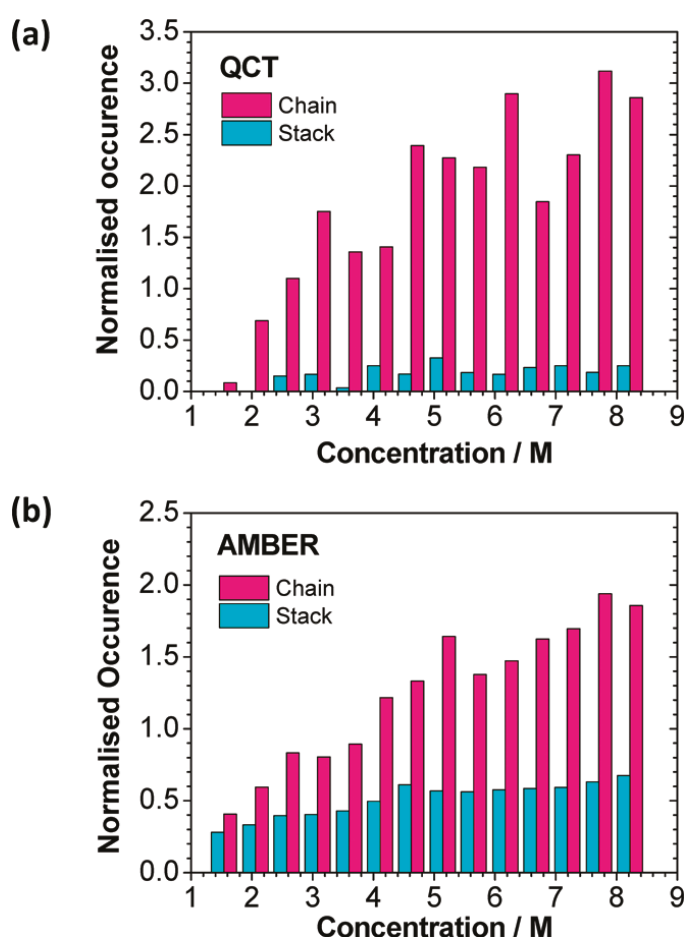


Figure 13 Distribution of stacked and chain dimers vs. imidazole concentration for (a) QCT simulations and (b) AMBER simulations.^[202]

As can be seen in the figure, the exact balance found between chain and stack structures depends sensitively on the choice of molecular dynamics algorithm, with the QCT method yielding a much stronger preference for chain formation than the AMBER

simulations. Furthermore, especially for the lower concentrations there are reliability limitations arising from the limited size of the solution sample that is accessible by simulation and the likelihood of reliably finding imidazole-imidazole interactions by simulation in the more dilute systems.^[202] However, it would seem plausible that imidazole-imidazole interactions similar to those found in its bulk pure phase would appear at concentrations where the supply of hydrate molecules is limited (see Figure 5). The structures identified in the radial distribution functions generated by the molecular dynamics simulations appear to be broadly in agreement with the structural parameters determined by Gontrani et al.,^[200] so the possibility of strongly self-associated chain-like assemblies resembling the solid state structure, perhaps mediated by hydrogen bonding through water, should be further considered.

Regarding the role of water in stabilising the self-associated assemblies, it is interesting to note that recent FTIR work has shown that water molecules prefer to act as an OH...3N hydrogen-bond donor toward imidazole, rather than acting as a N_H...OH₂ acceptor.^[203]

1.7.3 Soft X-ray photoelectron spectroscopy studies of aqueous imidazole solutions

As already mentioned in section 1.7.2, concentrated aqueous imidazole solutions have already been investigated as micro-jets^[117,120] by means of photoelectron spectroscopy (PES).^[145-147] This previous work will be strongly drawn upon in the interpretation of the experimental results obtained for this dissertation, and shall therefore be summarised here in sufficient detail to aid the reader.

The aim of the investigations reported by Jagoda-Cwiklik et al.^[145,146] was to measure the vertical ionisation potential (VIP) and adiabatic ionisation potentials (AIP) of both gas phase imidazole and imidazole in solution, and to relate the obtained values to a structure model through *ab initio* calculated molecular models. The VIP was calculated by comparing the energy difference between the optimised neutral structure and the cationic imidazole structure at neutral geometry. The AIP relates directly to the energy difference between the optimised neutral structure and optimised cation. To computationally model the ionisation potentials three methods were utilised; (1) microsolvation of the solute; (2) a hybrid of both quantum chemical and molecular dynamic (MD) approaches; (3) a polarizable continuum solvent model (PCM). A full quantum mechanical treatment of the ionisation potential was not possible, as the required calculations are computationally too expensive. The first two computational methods had been thoroughly tested in previous

investigations, while the PCM method was new. Two tests of PCM theory were therefore carried out for known ionisation potentials of halides in gas phase and solution. The results of this work are summarised in Table 3 and in Table 4.

anion	MP2/aug-cc-pvdz (aug-cc-pvtz)	experimental ionization potential in the gas phase
F ⁻	3.51 (3.59)	3.40
Cl ⁻	3.52 (3.58)	3.61
Br ⁻	3.37 (3.44)	3.36
I ⁻	3.15 (3.21)	3.06

Table 3 Comparison of PCM results^[145] against experimental ionisation potentials

anion	equilibrium PCM MP2/aug-cc-pvdz (aug-cc-pvtz)	nonequilibrium PCM MP2/aug-cc-pvdz (aug-cc-pvtz)	experimental vertical ionization potential in water ^a
F ⁻	7.36 (7.47)	9.63 (9.79)	9.8 (estimated)
Cl ⁻	6.63 (6.71)	8.55 (8.63)	9.6
Br ⁻	6.24 (6.34)	8.05 (8.14)	8.8
I ⁻	5.71 (5.85)	7.40 (7.48)	7.7

Table 4 Comparison of equilibrium and non equilibrium PCM potentials^[145] against vertical ionisation potentials of halides in solution.

The list of experimental vs. calculated ionisation potentials in Table 3 demonstrates the ability of the PCM method to accurately determine within 0.2 eV the potentials of halides in the gas phase. The results for modelling atoms in solution (Table 4) demonstrate that an equilibrium PCM model is not suitable. Better agreement with experimental data was found using a non-equilibrium PCM model (Table 4). This benchmarking indicated that the non-equilibrium PCM model was more suitable for the investigation and computational analysis of solution species by PES.

The experimental studies were carried out at BESSY (Berlin) on the UG41 PGM beamline, using a 2M solution of imidazole in water. No pH adjustment was performed, so the solutions were composed of neutral imidazole molecules (see Figure 6 and section 2.2). The spectrum was then compared to pure liquid water. Any differences in the

imidazole photoelectron spectra can be attributed to imidazole molecule and not surrounding water molecules (Figure 14).

Comparing both the imidazole and water spectra regions, one can clearly see that there is a region where the imidazole spectra have greater intensities. These areas include the binding energy ranges from -30 eV to -18 eV, and at the onset of emission around -8 eV. The latter region is of interest because it provides the lowest vertical ionisation potential (VIP), a quantity that is computationally accessible, as it represents the energy required for photo detachment from the HOMO of neutral aqueous imidazole. The lowest VIP of aqueous imidazole solutions generally occurs at a lower energy than the VIP of pure water, therefore the small shoulder seen on the peak below -10 eV is attributed to the corresponding lowest energy VIP. Its exact value was determined as -8.26 eV by fitting a small shoulder using three Gaussian peaks, as seen in the inset of Figure 14. The dotted blue line represents the emission peak for pure water.

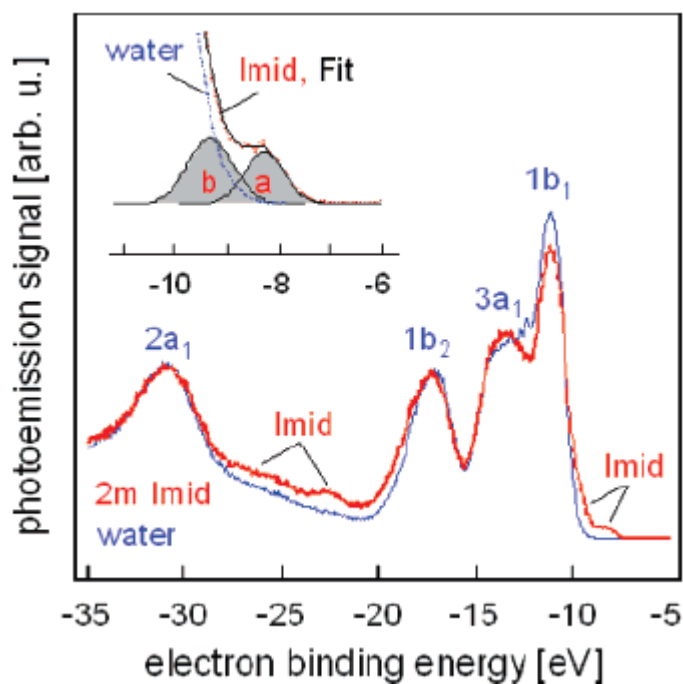


Figure 14 Photoelectron spectra of 2M imidazole and pure water.^[145]

The authors then calculated the VIPs for a series of geometry-optimised microsolvated gas phase clusters to examine how much hydration was required to reproduce the

experimental result of -8.26 eV satisfactorily. A selection of the more complex microsolvated clusters is reproduced in Figure 15.

The results (Table 5) indicate that increasing the number of water molecules in the microsolvation clusters generates increasingly better agreement with experiment. However, even microsolvation with 5 water molecules is not sufficient to reproduce the observed value of -8.26 eV. It appears that solvent effects beyond the first solvent shell have to be included to obtain agreement with experiment. The authors conclude that microsolvating by a small number of water molecules is not sufficient and that it is important to include long-range polarization of the water solvent by the solute. It is interesting to note, however, that the microsolvated imidazole monomer models considered in this study do not take into account self-association of imidazole. It would appear important to additionally examine more complex structure models such as those suggested by Gontrani et al.^[200] and Liem et al.^[202]

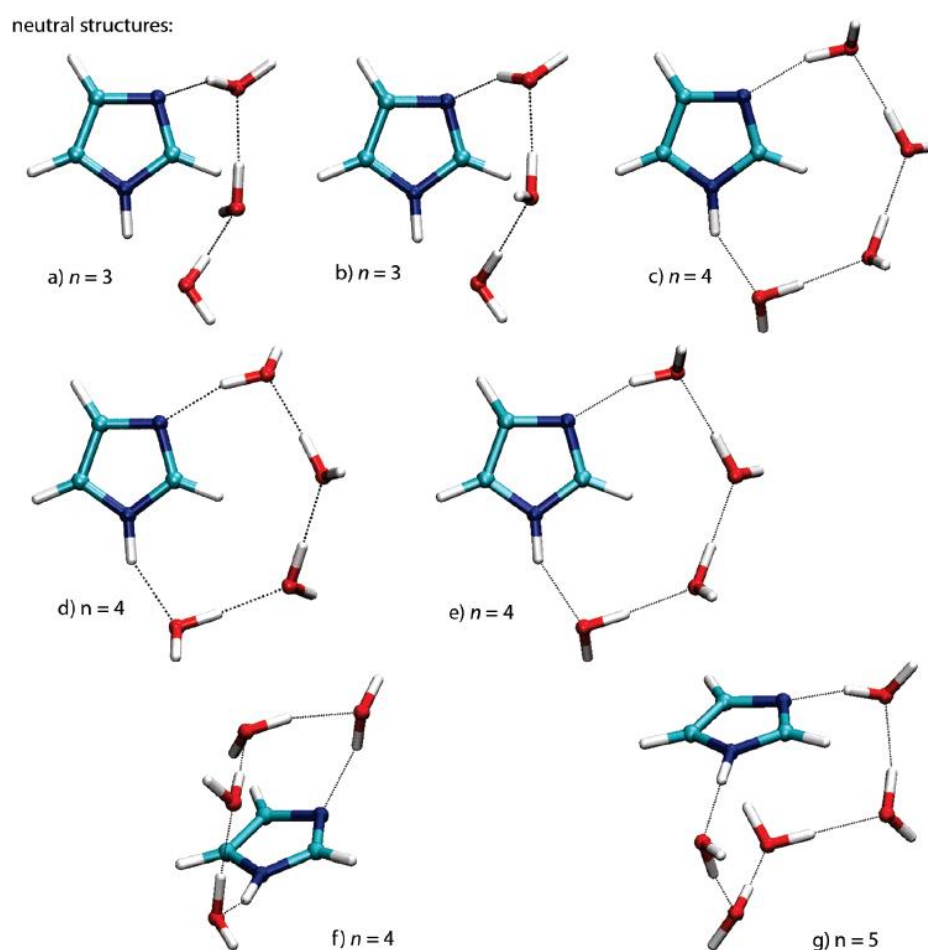


Figure 15 A selection of the microsolvated imidazole· $n\text{H}_2\text{O}$ clusters used for the analysis of the VIP in photoemission spectra from 2M aqueous imidazole solutions.^[145]

n H ₂ O	VIP [eV]
0	7.87
1	7.96
2	7.97
3(a)	7.93
3(b)	7.93
4(c)	7.95
4(d)	7.95
4(e)	7.95
4(f)	8.06
5	8.06

Table 5 Calculated VIPs for microsolvation clusters of increasing complexity.^[145]

In a separate study,^[147] the C 1s and N 1s core level binding energies of neutral imidazole and the imidazolium cation were experimentally examined by liquid microjet XPS. The results are summarised in Figure 16 and in Table 6.

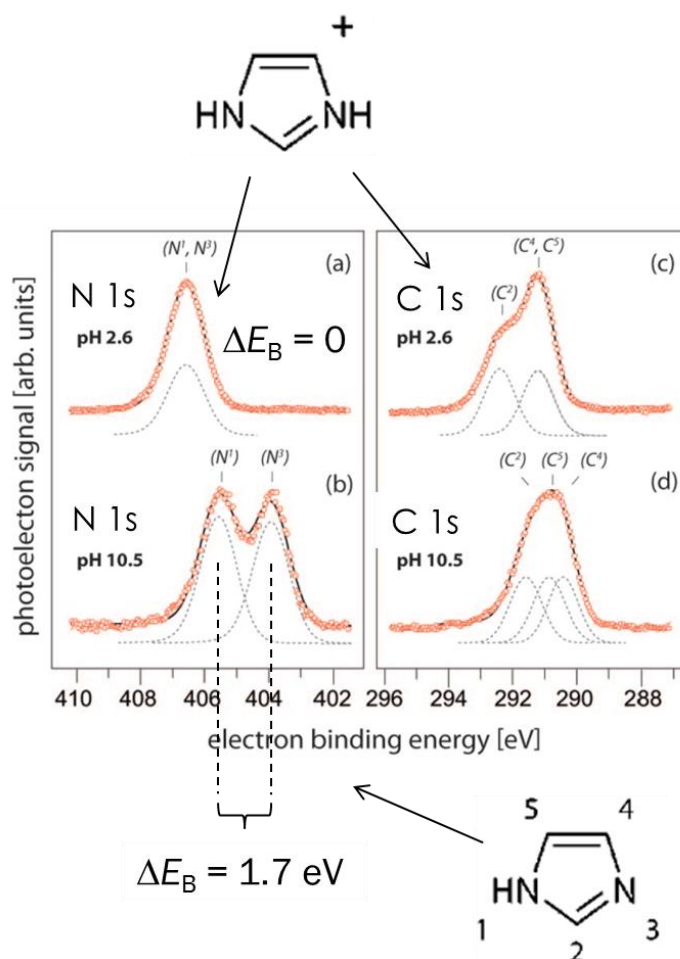


Figure 16 N 1s and C 1s XPS results for aqueous imidazole solutions at a pH of 2.6 and 10.5.^[147]

	neutral				protonated			
	exptl	$\Delta\varepsilon$	calcd	$\Delta\varepsilon$	exptl	$\Delta\varepsilon$	calcd	$\Delta\varepsilon$
N ¹	405.6		406.22		406.6		412.50	
N ³	403.9	1.7	403.95	2.3	406.6	0.0	412.50	0.0
C ²	291.7		291.32		292.4		298.05	
C ⁴	290.5	0.8	290.72	0.6	291.2	1.2	296.82	1.2
C ⁵	290.9	0.4	290.30	0.4	291.2	0.0	296.82	0.0

^a $\Delta\varepsilon$ is the difference between the respective binding energies.

Table 6 Experimental and calculated C1s and N1s core level binding energies for neutral imidazole and imidazolium species.^[147]

It can be seen from the experimental results that protonation leads to the equivalency of the C 1s and N 1s core level binding energies in the now symmetry-equivalent N and C atoms of the imidazolium ring. It is also evident that the experimental N 1s core level binding energy shift of the neutral aqueous imidazole species (1.7 eV) is much lower than the value of 2.3 eV predicted for an isolated neutral gas phase imidazole molecule. As the study of VIPs the structure model used for the calculation of theoretical values lacks the complexity expected for a self-associated system. Not all information contained in the experimental data has yet been mined.

Overall, it can therefore be concluded from these photoemission studies that more systematic work is required to generate a more quantitative view of the relationship between photoemission features and the structure of self-associated imidazole solutions. XAS is more versatile than XPS for the study of solutions, through its ability to provide information on ground and excited states involving the valence region of atoms. The development of XAS methodology should be straightforward because there is no requirement for high resolution detectors that require ultra-high vacuum, and hence no use of a liquid microjet is required. Nevertheless, the combination of XPS and XAS would be the most powerful, as the knowledge of ground state core level binding energies provided by XPS facilitates a more reliable interpretation of XAS data. Recently published work on formic acid and formate solutions indicates indeed that it is essential to be able to separate initial state from final state orbital chemical shifts.^[161]

1.8 Computational methods used to simulate NEXAFS

Different kinds of computer software have been used for the analysis of XAS data. The purpose of this section is to give a very brief overview of the main computational techniques currently used in the field. A comprehensive list of all the available computational methods can be found on the international XAFS society website ^[204]. The most widely applied program used to interpret XAFS spectra *ab initio* is the FEFF series^[205-207] of programs. FEFF applies a multiple scattering description of the EXAFS and near-edge spectra to a cluster of atoms that has the X-ray absorber of interest in its centre. The most recent code FEFF8 applies numerous parameters including polarisation dependencies, a fully relativistic cross section and atomic calculations.^[115,208-211]

Molecular orbital methods have long been used for the calculation of electronic states by linear combination of atomic orbitals (LCAOs). The most commonly used LCAO method for the calculation of near-edge core level spectra is the use of the discrete variation method DV- $X\alpha$ that can calculate the core-hole relaxation state.^[38] A negative aspect of using DV- $X\alpha$ is that the calculation is only suitable for XANES spectra, whereas FEFF can calculate both XANES and EXAFS spectra. Jiang et al calculated the XANES spectra of Co compounds (Co (OH)₂, CoTiO₃, Co₃O₄, and CoAl₂O₄) utilising the DV- $X\alpha$ method.^[212] Utilising this approach various atomic potentials were interpreted and a crystal potential generated. To summarise the calculations utilised, both discrete variational wave functions and multiple scattering wave functions allow the determination of projected states and final state. It is important to note that the SF₆ molecule has been used as a reference with the DV- $X\alpha$ method, in effect to confirm the efficacy of various computational codes.^[213,214] The LCAO DV- $X\alpha$ SF₆ molecule calculation compares well with experimental XANES data. Further examples of the application of the LCAO DV- $X\alpha$ method to XANES interpretation include XANES spectra of silicon oxides,^[215] transition metal complexes^[216,217] and oxyanions.^[218]

Boron K-edge NEXAFS was recorded for boric acid, borate and polyborate ions and directly compared to theoretical NEXAFS spectra determined from first principles DFT for both of the following approximations excited electron and core hole.^[219] The simulations were useful as the following could be inferred from the experimental results: water is orientated isotropically about the boric acid and that boron K-edge NEXAFS are insensitive to hydrogen bonding, salt interactions and molecular environment. The analysis of the N₂ K-edge NEXAFS was utilised to demonstrate that the quantisation can be determined exactly computationally via the discrete variable representation.^[220] The

computationally determined NEXAFS spectra can thus be predicted semi-quantitatively. The computational results ultimately prove the limits to which the method can determine theoretical vibrational features in NEXAFS spectra. The effect of nuclear quantum dynamics^[221] on the simulated nitrogen K-edge NEXAFS of *s*-triazine has also been examined, showing that the inclusion of nuclear quantum dynamics allows the interpretation of some spectral features that undergo broadening. The results from the computational calculations highlight the significant impact of nuclear quantum dynamics on the sensitivity of NEXAFS with regards quantum nuclear motions within molecules. This lead to the conclusion for further simulated NEXAFS calculations, that the quantum motion of molecules under study should be accurately understood.

1.9 Objectives of the research described in this thesis

The overall objective of this work was to demonstrate that it was possible to extend the application of soft X-ray absorption spectroscopy to the interrogation of solution assemblies of a complex, non-ionic self-associating organic solute, from low concentrations through to concentrated solutions, and perhaps even to the supersaturated state from which nucleation occurs.

Aqueous imidazole was chosen as the test system for these studies for the following reasons:

- XPS data of solutions were already available in the literature (see previous section), which would be a significant aid in the interpretation of the NEXAFS
- Very high concentrations are achievable, ensuring that detectable signals could be achieved
- The system is well known to exhibit strong self-association, making its structural elucidation an interesting scientific objective in its own right
- The system is highly relevant for biological, pharmaceutical and medical science
- Previous computational studies of imidazole/water clusters were available in the literature
- A parallel programme of molecular dynamics work at our University was pursued in the group of P.L.A. Popelier, providing structural model input to the interpretation of the obtained data

Besides demonstrating the feasibility of NEXAFS studies of this system the key scientific aim was to generate further structural understanding of the self-association process in aqueous imidazole solutions. To achieve this aim, the following objectives were formulated, which would permit a step-wise systematic approach of building up complexity and a more complete understanding of the system:

- A full understanding of the N K-edge spectrum of the imidazole gas phase monomer,
- A full understanding of the N K-edge spectrum of the imidazole crystal structures,
- Elucidation of the influence if imidazole-water interactions on the N K-edge spectrum,
- Elucidation of the influence if imidazole-imidazole interactions on the N K-edge spectrum, including hydrogen bonding and π - π interactions.
- Evaluation of complex structural models involving both imidazole-imidazole and imidazole-water interactions to generate an understanding of the N K-edge spectrum of solutions and arrive at a structure model.

2. Methods and Materials

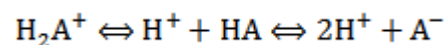
2.1 Preparation of imidazole solutions

Imidazole was obtained from Sigma Aldrich as ACS grade $\geq 99\%$ (titration) with total impurities of $\leq 0.2\%$ water. 1-methylimidazole was obtained from Sigma Aldrich with a purity of 99%. All solutions were made using laboratory grade deionised water.

2.2 Brønsted Equilibria and pH measurements

2.2.1 Speciation as a function of pH

A Brønsted acid with two K_a values, K_{a1} and K_{a2} , is characterised by the coupled equilibria



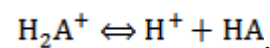
Equation 1

For a speciation diagram we wish to know the concentrations $[\text{A}^-]$, $[\text{HA}]$, $[\text{H}_2\text{A}^+]$. To obtain them we must solve a system of equations. To begin with, we know that

$$[\text{HA}]_0 = [\text{A}^-] + [\text{HA}] + [\text{H}_2\text{A}^+]$$

Equation 2

The equilibrium reaction at low pH is



Equation 3

so we can write, using the well known^[222] definition of the K_a :

$$K_{a1} = \frac{[\text{H}^+][\text{HA}]}{[\text{H}_2\text{A}^+]} = \frac{[\text{H}^+][\text{HA}]}{[\text{HA}]_0 - [\text{HA}] - [\text{A}^-]}.$$

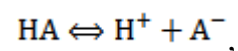
Equation 4

This expression can be rearranged to

$$[\text{HA}] = \frac{[\text{HA}]_0 - [\text{A}^-]}{\left(1 + \frac{[\text{H}^+]}{K_{a1}}\right)}$$

Equation 5

The equilibrium for the second dissociation at high pH is



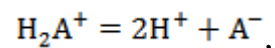
Equation 6

from which follows that

$$K_{a2} = \frac{[\text{H}^+][\text{A}^-]}{[\text{HA}]} = \frac{[\text{H}^+][\text{A}^-]}{[\text{HA}]_0 - [\text{A}^-] - [\text{H}_2\text{A}^+]}$$

Equation 7

The overall equilibrium is



Equation 8

and the expression for its equilibrium constant is

$$K = K_{a1}K_{a2} = \frac{[\text{H}^+]^2[\text{A}^-]}{[\text{H}_2\text{A}^+]} = \frac{[\text{H}^+]^2[\text{A}^-]}{[\text{HA}]_0 - [\text{HA}] - [\text{A}^-]} ,$$

Equation 9

which can be rearranged to

$$[\text{HA}] = [\text{HA}]_0 - [\text{A}^-] \times \left(1 + \frac{[\text{H}^+]^2}{K} \right)$$

Equation 10

We now combine the expressions for [HA] in Equation 5 and in Equation 10,

$$[\text{HA}]_0 - [\text{A}^-] \times \left(1 + \frac{[\text{H}^+]^2}{K} \right) = \frac{[\text{HA}]_0 - [\text{A}^-]}{\left(1 + \frac{[\text{H}^+]}{K_{a1}} \right)} ,$$

Equation 11

solve for $[\text{A}^-]$, and obtain

$$[\text{A}^-] = [\text{HA}]_0 \left(\frac{1}{1 + \frac{[\text{H}^+]}{K_{a2}} + \frac{[\text{H}^+]^2}{K}} \right)$$

Equation 12

This expression is plausible: for high pH, $[H^+] \rightarrow 0$, and $[A^-]$ becomes equal to $[HA]_0$. Using it we can now calculate $[HA]$ from Equation 10:

$$[HA] = [HA]_0 \left(1 - \frac{1 + \frac{[H^+]^2}{K}}{1 + \frac{[H^+]}{K_{a2}} + \frac{[H^+]^2}{K}} \right),$$

Equation 13

which yields

$$[HA] = [HA]_0 \left(\frac{1}{1 + \frac{K_{a2}}{[H^+]} + \frac{[H^+]}{K_{a1}}} \right)$$

Equation 14

This expression shows how $[HA]$ depends, as expected, on both acidity constants, and with opposite dependence on pH for each of the two equilibria.

Using Equation 1, $[H_2A^+]$ now follows as:

$$[H_2A^+] = [HA]_0 - [A^-] - [HA]$$

Equation 15

or

$$[H_2A^+] = [HA]_0 - [HA]_0 \left(\frac{1}{1 + \frac{[H^+]}{K_{a2}} + \frac{[H^+]^2}{K}} \right) - [HA]_0 \left(\frac{1}{1 + \frac{K_{a2}}{[H^+]} + \frac{[H^+]}{K_{a1}}} \right)$$

Equation 16

Using this expression together with Equation 12 and Equation 14, and the imidazole pK_a values^[185,186] of $pK_{a1} = 7.05$ and $pK_{a2} = 14.52$, one obtains the diagram shown in Figure 6.

2.2.2 Calculation of pH of a weak base

Imidazole is a weak base in water. The pH of its aqueous solutions can be calculated from the pK_a value and its concentration $[HA]_0$ as follows. First, we remember that the pK_a is

$$pK_a = -\log_{10}(K_a).$$

Equation 17

The acid/base equilibrium defines the K_a value of a partially dissociated acid as

$$K_a = \frac{[\text{H}^+][\text{A}^-]}{[\text{HA}]} = \frac{[\text{H}^+]^2}{[\text{HA}]_0 - [\text{H}^+]}$$

Equation 18

Charge neutrality requires that $[\text{H}^+] = [\text{A}^-]$, so we can substitute and solve for $[\text{H}^+]$. We obtain

$$[\text{H}^+] = -\frac{K_a}{2} \pm \sqrt{K_a [\text{HA}]_0 + \frac{K_a^2}{4}}$$

Equation 19

Using this equation we can calculate the pH of any weak acid or base as a function of its concentration $[\text{HA}]_0$.

2.2.3 pH measurements

All pH measurements of imidazole solutions were made using a micro tipped pH electrode probe. Before any measurements the pH electrode was calibrated to check for tolerance using three various buffered solutions (3, 6 and 9).

As expected for a weak base, it was found that all imidazole solutions had a pH above 9. Figure 17 compares the experimentally observed pH values with the expected pH behaviour, as calculated with Equation 19 using the $\text{p}K_{a1}$ of imidazole (7.05).^[185,186] It can be seen that the measured pH agrees well with the expected pH at concentrations up to approximately 1 mol L^{-1} .

The experimental values are consistently somewhat lower than expected when the imidazole concentration exceeds approximately 2 mol L^{-1} . This may be an indication for an increasing degree of self-association by imidazole-imidazole hydrogen bonding. Such self-association would be expected to reduce availability of molecules for interaction with water and release of OH^- anions.

However, the effect is small and the predicted pH behaviour is only very slightly outside the estimated error of the pH. Furthermore, it is not clear whether the response of the pH electrode may be affected by high concentrations of hydrogen-bonding solutes.

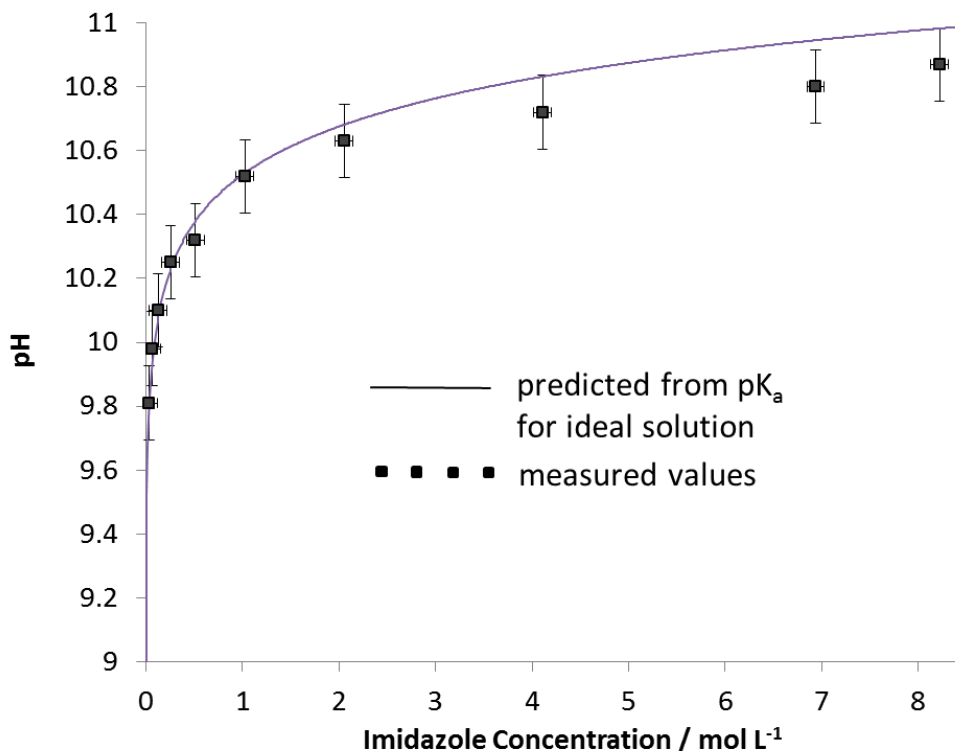


Figure 17 Experimental values vs. predicted pH of ideal imidazole solutions as a function of concentration.

2.3 X-ray absorption spectroscopy

The linear X-ray absorption coefficient $\mu(E)$ is defined through the attenuation law

$$I(E) = I_0(E)e^{-\mu(E) \cdot d}$$

Equation 20

where $I(E)$ is transmitted X-ray intensity, d the sample thickness, $I_0(E)$ the X-ray intensity prior to entering the sample and E the photon energy.^[96] The XAFS function $\chi(k)$ is defined as the variation of $\mu(k)$ about the smoothly varying, ‘atomic’ background $\bar{\mu}(k)$,^[96]

$$\chi(k) = \frac{\mu(k) - \bar{\mu}(k)}{\bar{\mu}(k)},$$

Equation 21

and is commonly described as a function of the magnitude the photoelectron wavevector k (where $k = 2\pi/\lambda$, with λ the photoelectron wavelength, k is usually given in \AA^{-1}). The relation between the wavevector and the energy E_e of the free photoelectron is given by^[96]

$$E_e = \frac{\hbar^2 k^2}{2m_e},$$

Equation 22

where m_e is the mass of the electron at rest. It follows that the magnitude of the wavevector k can be calculated from E_e according to^[96]

$$k = \frac{2\pi\sqrt{2m_e E_e}}{\hbar} = 0.51171\sqrt{E_e}.$$

Equation 23

The XAFS is the sum of all photoelectron scattering paths Γ , often expressed in Hartree atomic units with $e = m = \hbar = 1$,⁽⁴⁷⁾

$$\chi(k) = \sum_{\Gamma} \frac{S_0^2}{kR^2} |f_{\text{eff}}^{\Gamma}(k)| \exp\left(-\frac{2R}{\lambda(k)}\right) \exp\left(-\frac{2\sigma_{\Gamma}^2}{k^2}\right) \sin[2kR + \phi_{\Gamma}(k) + 2\delta_c(k)]$$

Equation 24

Amplitude losses through many-body interactions are included through the k -independent amplitude factor S_0^2 and a mean-free-path function $\lambda(k)$.^[96] The scattering matrix $f_{\text{eff}}^{\Gamma}(k)$ represents the effective curved-wave backscattering amplitude for each path Γ , whereas $\phi_{\Gamma}(k)$ is the effective phase shift of the scattering path and $\delta_c(k)$ the final-state phase shift at the central atom.^[96] The Debye-Waller factor $2\sigma_{\Gamma}^2$ accounts for the dephasing of the backscattered photoelectron wave through thermal and static disorder.^[96]

The origin of the photoelectron wavevector scale is *a priori* unknown.^[96] In theory, the kinetic energy E_e of the photoelectron is given by^[96]

$$E_e = \hbar^2 k^2 / 2m_e = E_{\text{tot}} - E,$$

Equation 25

where E_{tot} is the total energy of the photoelectron and E the energy of a free electron of zero wavevector in the sample, *i.e.*, the effective mean potential seen by a free electron. E is experimentally not accessible.^[96] Only the energetic position of the absorption edge (E_{edge}) can be observed, which occurs at the lowest unoccupied non-forbidden

energy level and is offset from the true initial binding energy of the photoelectron by E_0 , the so-called threshold energy:^[96]

$$E_e = \hbar\omega - E_{\text{edge}} + E_0.$$

Equation 26

NEXAFS analysis consists essentially of modelling of the spectral pre-edge background to generate a normalised absorption spectrum and identification of the absorption features in the data. Data need to be carefully examined for artificial irregularities, such as noise spikes, singularities ('glitches') in the monochromator transmission function or other unusual features.^[96] In obvious cases, these can sometimes be removed by editing of the raw spectrum or through interpolation between neighbouring datapoints. Normalisation usually follows a three-step process,^[96] including (i) fitting and subtraction of a smooth, polynomial pre-edge function extrapolated into the post-edge region, (ii) fitting and subtraction of the post-edge background, and (iii) edge-step normalization of the $\mu(E)$ spectrum to the post-edge background or the edge-step height.^[96] A typical background subtraction obtained by this three-step procedure is given in Figure 18 for the K-edge spectrum of Ni metal.^[96]

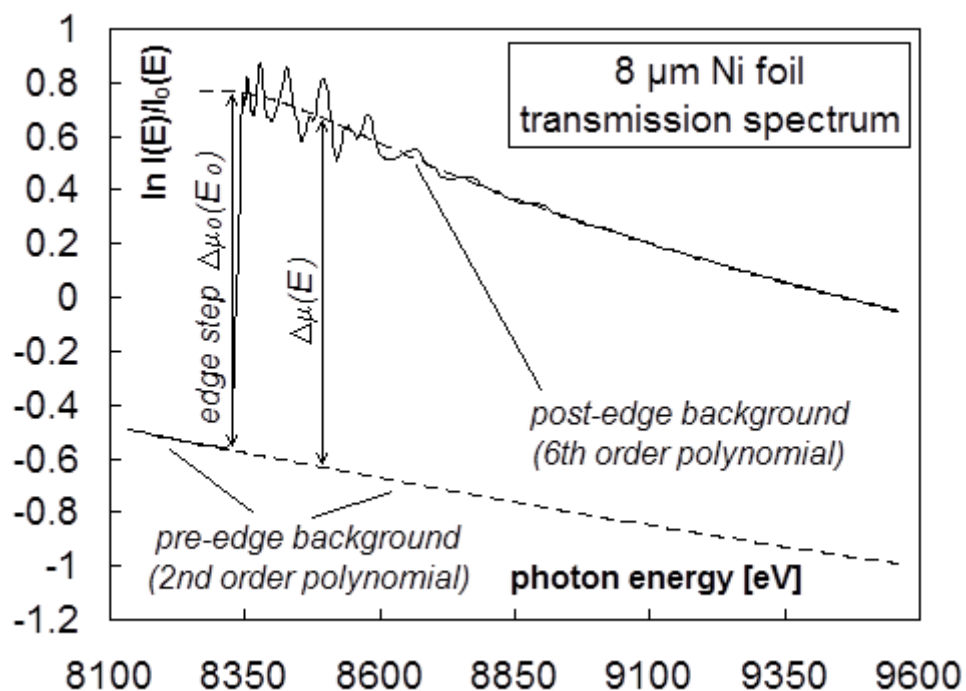


Figure 18 Background subtraction for transmission spectrum of Ni metal.^[96]

2.4 Synchrotron Radiation

XAS experiments have advanced considerably since the 1970s due to the development of synchrotron radiation sources. Synchrotron radiation is produced when charged particles are accelerated through a magnetic field; in turn these magnets also steer and keep the particles in the correct position. Below is a figure of the main components of a synchrotron explaining how the radiation eventually reaches the beam line and experimental end station.

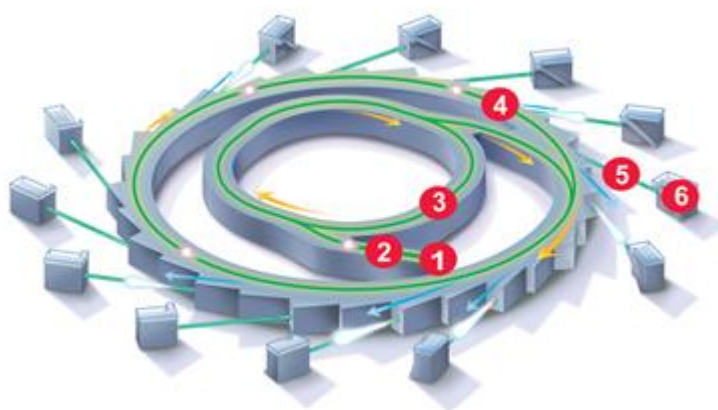


Figure 19 Components of a Synchrotron radiation laboratory.^[223] (1) Electron gun; (2) LINAC; (3) Booster ring; (4) Storage ring; (5) Beamline; (6) End station

The electrons are sourced at the electron gun and are boiled off a cathode running off 220,000 volts; the electrons are then transferred away from the cathode using a strong positive charge. The accelerator then uses microwave fields to accelerate the electrons up to $3 \times 10^8 \text{ m s}^{-1}$. The linear [electron] accelerator (LINAC) then pulses the electrons out into a vacuum to the booster ring. Here the electrons gain a massive energy boost from roughly 200 MeV to 6 GeV. The ring is surrounded by electro magnets that direct the high energy electrons around the ring. When these electrons reach the necessary energies they are injected into the storage ring, where they are circulated producing synchrotron radiation. Joining the storage ring are several beam lines and experimental chambers that accommodate different types of synchrotron radiation. This describes only the basic structure of a synchrotron; however developments are continually improving synchrotrons allowing for even brighter beams. Wigglers and undulators have been developed these are inserted into the storage ring. They allow the electrons to be controlled creating a narrow brighter beam.

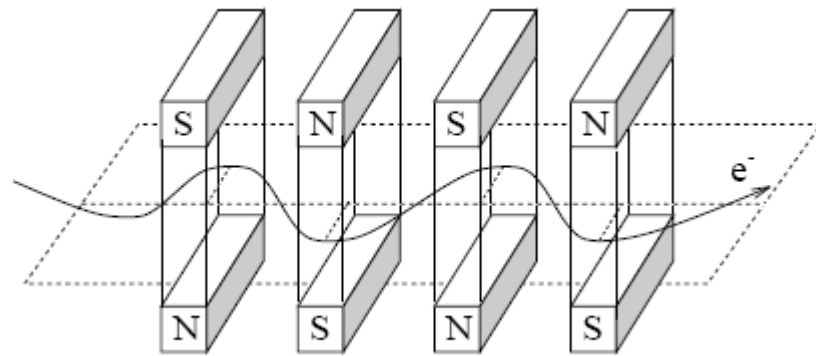


Figure 20 Wiggler device inserted into Storage ring.^[223]

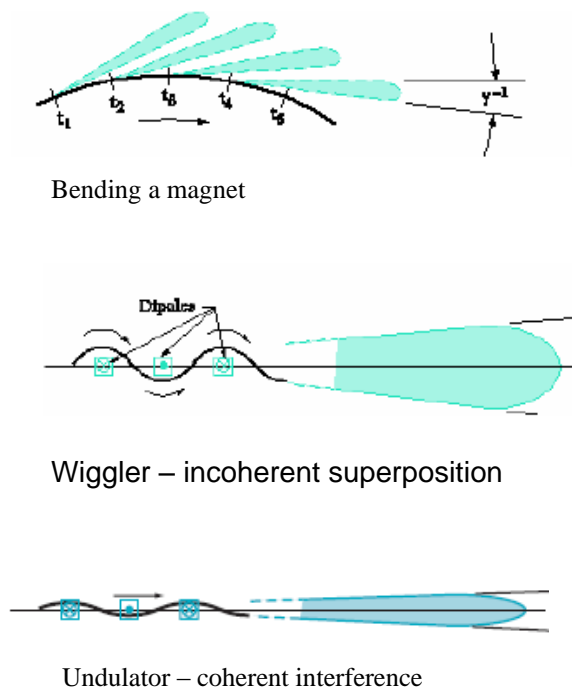


Figure 21 Effects of wigglers and undulators on the X-ray beam.^[223]

2.5 Experimental NEXAFS Setup at BESSY

Altogether three weeks of experiments for this project were carried out at the BESSY synchrotron facility in Berlin. BESSY is the third synchrotron source of its kind in Germany providing a range of ultra-bright photons. In total 46 beam lines are in use taking advantage of undulator, dipole and wiggler sources.

The analysis was undertaken on beamline U41- PGM. The pictures below illustrate the experimental set up on the beam line and experimental chamber. The experimental

chamber has been specifically designed for analysis of solution systems under vacuum or an inert helium atmosphere. The end station setup incorporates a differential pumping stage that enables operation of an end station at high pressures, a refocusing mirror and the main chamber (Figure 22). Light from the ring is first refocused under ultra-high vacuum conditions and then passes through the differential stage to a high vacuum environment. Before the X-rays enter into the high pressure experimental chamber they pass through a thin Si_3N_4 membrane.

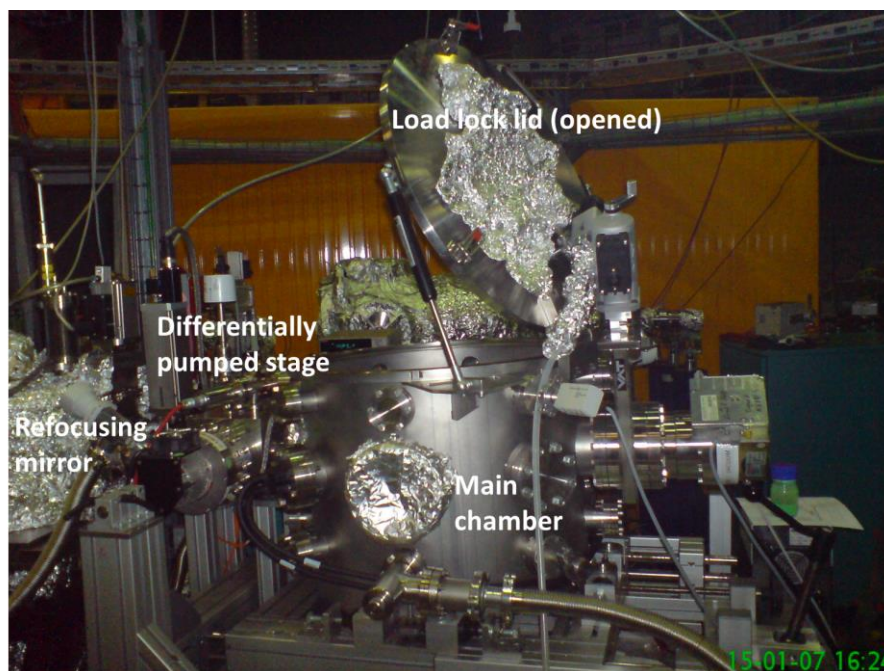


Figure 22 Experimental chamber; note the amount of tin foil used to ensure that the photodiode does not detect any background light.

Additional pictures showing the experimental setup inside the high pressure chamber are given in Figure 23 and in Figure 24. An initial run of experiments was carried out using a simple open cell with stagnant solutions. Good quality data could readily be obtained over a wide range of concentrations (10^{-3} mol L^{-1} to saturation concentrations around 10 mol L^{-1}), but, as will be shown in a later section of this thesis, evidence for X-ray beam damage was observed and at high concentrations evaporation from the open solution surface led to the observation of crystallised solids, rather than of the desired solution.

XAS work in the 2nd year of the project therefore utilised a newly developed closed flow cell developed by our cooperation partners at BESSY.^[224] The solution to be sampled flows, pumped by a peristaltic pump, through a closed cell (Figure 25), which enables the surrounding main chamber to be pumped to high vacuum. The X-rays impinge through a

Si_3N_4 membrane onto the sample. Florescence yield detection is carried out with a GaAsP $5 \times 5 \text{ mm}^2$ photodiode. As the cell membrane easily bursts when too much internal is applied during pumping of the liquid it is possible to contaminate the beam line. To ensure that this does not occur a pressure sensor is connected to the differential pump if a pressure rise occurs a fast-closing valve is triggered and immediately isolates the end station from the beamline.

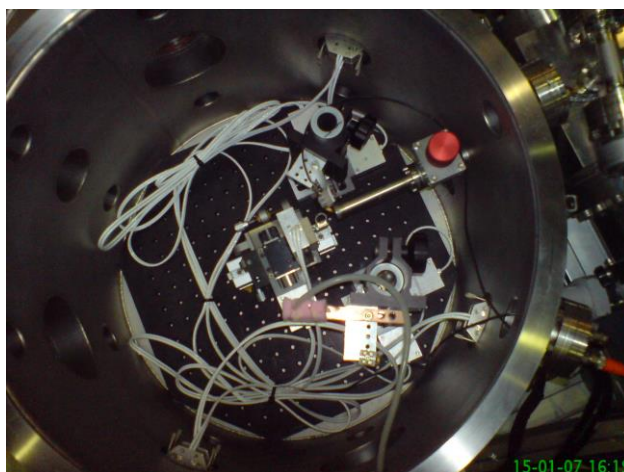


Figure 23 Inside the chamber; three x, y, and z stages control and align the X-rays, photo-diode, digital camera and sample holder.

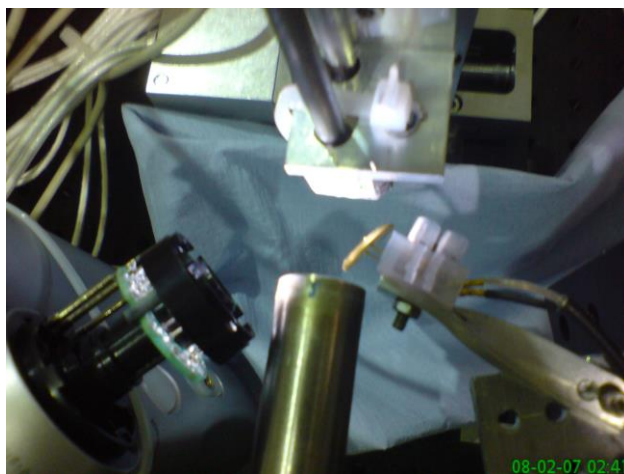


Figure 24 This is the position at which the X-rays are aligned to the sample holder. Note the digital camera on the left; this was useful for recognising leaks or crystallisation.

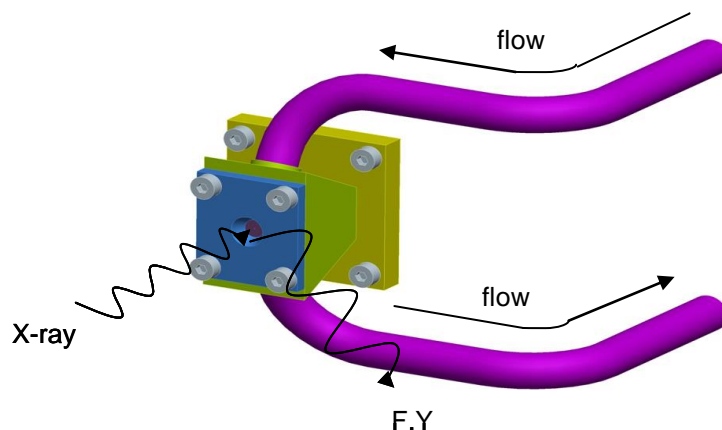


Figure 25 Flow cell used during flow experiments.^[224]

The flow cell setup allows multiple samples to be analysed without the need to open the analysis chamber. As the sample is introduced by continuous pumping from an external reservoir it is possible to maintain temperature and flow rate of a homogeneous solution, while the volume of the reservoir is stirred and heated. During a sample change the system was purged for 30 min with deionised water. Then a control measurement of the spectrum was performed to ensure that the cell was clean. The low rate was typically set to 40 mL s^{-1} and allowed to flow for at least 20 min to let the system equilibrate. Three NEXAFS spectra, each taking about 20 min to acquire, were then measured.

2.6 Raman Spectroscopy

Raman spectroscopy is a scattering technique that probes molecular vibrations by light scattering. Raman spectroscopy uses laser photons to interrogate the sample. The photons then lose or gain energy with the sample interaction. This loss or gain is characteristic of a specific bond or functional group. Spectra produced are precise and are specific for that sample under analysis. Some advantages of the technique include:

- It can be used to analyse aqueous solutions, as it does not suffer from water absorption.
- Intensities of functional groups represented by bands are directly related to the concentration of that particular functional group.
- Little or no sample preparation.

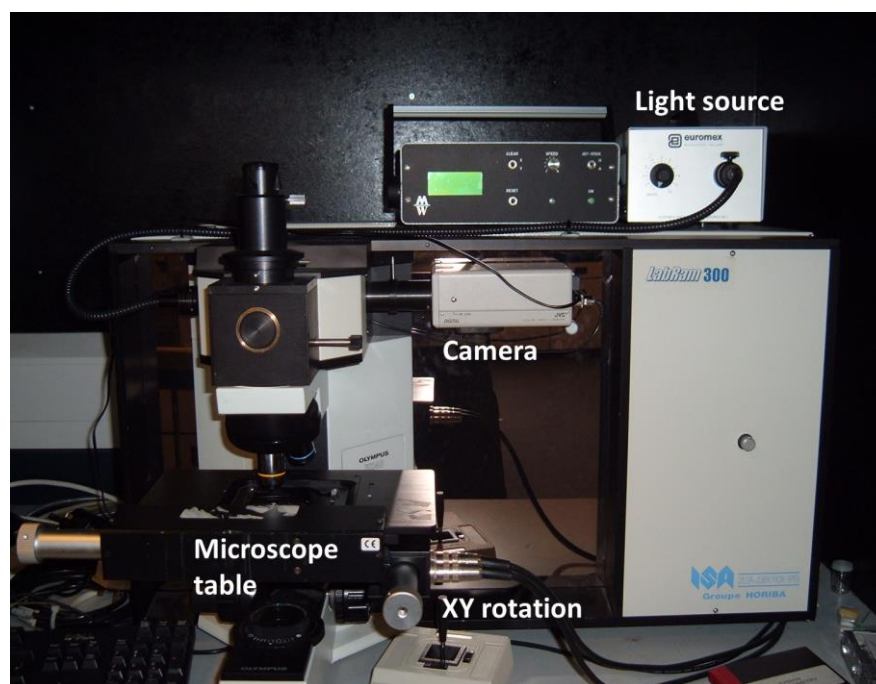


Figure 26 Horiba Jobin-Yvon LabRam 300 Raman spectrometer used for this study

The Raman analysis of imidazole solutions was carried out using a Horiba Jobin-Yvon LabRam 300 spectrometer. All solutions were sampled with a small pipette, removing 4 ml from the stock solution and applying a single drop to a glass microscope slide. The plate was placed on the microscope table and the laser beam carefully focused onto the surface of the sample.

2.7 StoBe DeMon Software

This software uses a hybrid density functional theory (DFT)^[158,225,226] with a double zeta, local spin density exchange and correlation function by Vosko and Wilk.^[227] The software itself has been described in detail in several papers.^[225,226,228-230] One study^[229] concentrates on the calculation of X-ray emission spectra (XES) of molecules and surface adsorbates by density functional theory. A modification of DFT is proposed and applied to the study of X-ray emission spectra. The theory addresses the issue of attaining a correct charge transfer between the surface and the adsorbate. The Stockholm-Berlin (StoBe) computational software uses ground state orbitals to analyse transition intensities and calculate transition potential. The valence orbital binding energies are evaluated and a X-ray emission spectra generated. Further work^[231-233] has demonstrated the capacity of DFT in computing near-edge X-ray absorption spectra. The study therefore aims to investigate the application of DFT based calculations to x-ray emission spectra. Overall

comparing the DFT approach alongside Hartree-Fock the spectra are similar and however when surface adsorbates are computed the DFT spectra demonstrate a significant improvement. A detailed study of pyridine^[228] at the C1s and N1s thresholds demonstrated the suitability of the DFT based StoBe approach. Experimentally high resolution near-edge X-ray fine structure (NEXAFS) was investigated. Alongside the DFT approach ab initio techniques were also calculated to interpret the experimental data. StoBe calculates XANES spectra by utilising Kohn-Sham orbitals. This is a transitional potential approach, where only half of a core electron is excited. StoBe employs a double basis set where a standard basis set is combined with a large basis set utilising additional functions. The unoccupied excited levels are generated from using the core hole density alongside the extended basis set. The transitions generated from the transition potential optimisation are then related to ground and excited states. This computational method has demonstrated sensible theoretical results for adsorbates and various molecules.

To generate theoretical XANES spectra for imidazole StoBe requires an input file that contains a sensible geometry in either Cartesian or z-matrix format, also the necessary basis sets for the atoms need to be included.

2.8 Gaussian

Gaussian^[234] is able to predict properties of molecules, as well as possible pathways of chemical reactions. Here is a list of calculations that the Gaussian programme can carry out

- Molecular energies and structures
- Energies and structures of transition states
- Bond and reaction energies
- Molecular orbitals
- Atomic charges and electrostatic potentials
- Vibrational frequencies
- Thermochemical properties

The version Gaussian 03^[234] was used for the work described in this dissertation. It allows various solvation fields to be applied to molecules and modelled. Although

Gaussian was not used extensively in my thesis, I was able with advice from collaborators to calculate simple geometry optimisations of imidazole clusters. The following summarises what calculations can be carried out with the program.

2.8.1 *Single point energy calculation*

The total energy of the molecule is the sum of electronic energy, nuclear repulsion and kinetic energy. The accuracy of Gaussian energy calculations is ultimately determined by the initial input properties. Comprehensive and accurate energy predictions require a thermal or zero-point energy correction. Single point energy calculations are used to determine the following:

- Molecular orbitals of a given molecular system
- Geometry optimisation for further advanced calculations.
- Accurate energies of a geometry obtained using a lower level of theory

Single point energy calculations can accommodate either large or small basis sets at various levels of theory.

2.8.2 *Geometry Optimisation*

A potential energy surface of a molecular system is dependent on its structure; it relates the energy of the system to the parameters defining the geometric structure of the molecular system. The minimum of the potential energy surface can be found by using geometry optimization calculations. These calculations determine the energy at that specific point on the surface and the gradient of the surface; these results are then used to for further optimisation. The gradient is a measure of how rapidly the energy changes between two points on the potential energy surface.

2.8.3 *Frequency calculations*

This calculation is not directly relevant to the experimental techniques used in this dissertation, but it predicts useful reference data such as frequencies and intensities of vibrational bands, force constants, stationary points on the potential energy surface, zero-point vibration and thermal energy corrections, thermodynamic quantities such as enthalpy and entropy.

Frequency and zero-point energy (ZPE) values computed at the Hartree-Fock level contain known systematic errors due to the neglect of electron correlation, resulting in overestimates of about 10%-12%. Therefore, it is common to scale frequencies predicted

at the Hartree-Fock level by an empirical factor of 0.8929. The use of this factor has been demonstrated to produce very good agreement with experiment for a wide range of systems.^[235] Frequencies and ZPEs computed with methods other than Hartree-Fock are scaled similarly to eliminate known systematic errors in calculated frequencies. Table 7 lists the recommended scale factors for frequencies and for ZPE.

Method	Scale Factor	
	Frequency	ZPE/Thermal
HF / 3-21G	0.9085	0.9409
HF / 6-32G (d)	0.8929	0.9135
MP2 (Full) / 6-31G (d)	0.9427	0.9646
MP2 (FC) / 6-31G (d)	0.9434	0.9676
SVWN / 6-31G (d)	0.9833	1.0079
BLYP / 6-31G (d)	0.9940	1.0119
B3LYP / 6-31G (d)	0.9613	0.9804

Table 7 Scale factors for frequencies and zero-point energies (ZPEs) in Gaussian.

2.8.4 Modelling systems in solution

Gaussian03 is able to model solution systems with varying degrees of accuracy. Methods include the following.

Self-Consistent Reaction Field (SCRF) methods are based on the Onsager reaction field model.^[236] The solute is placed in a spherical cavity of radius a_0 in the solvent field. Dipoles in the solution are induced by any dipoles present in the molecules, and a net stabilisation of fields results from the interaction between the electric dipole field of the solution and the molecular dipoles.

Tomasi's Polarized Continuum Model (PCM)^[237] is a popular model that is commonly used. This models the solution and molecules as a series of interlocking spheres around the atoms. The molecular dipole influence on the solvent is given by numerical values.

There are two isodensity surface SCRF models.^[238,239] They define the solvent through numerical values. The first model, the isodensity PCM (IPCM), uses an SCRF that is iteratively refined until it converges on the isodensity of the surface of molecules in

solution. The Self-Consistent Isodensity Polarized Continuum Model (SCI-PCM) is an extension of this model that also takes electron density effects into account.

3. N K-edge NEXAFS of Imidazole: A Comparative Computational Analysis of Gas Phase Monomer and Solid State Spectra

3.1 Introduction

There is considerable interest in understanding the interactions of imidazole in aqueous media due to its biological importance as the side chain of the amino acid histidine, which plays, for example, an important role in catalytic conversions in metalloproteins. Experimental evidence for very high self-association of imidazole in aqueous solutions at all concentrations above 10^{-4} mol L⁻¹ has been accumulated for more than 70 years (see section 1.7.2) and is therefore well documented. As summarised in section 1.7.2, all previous interpretations of experimental evidence have relied on structure models that include strong imidazole-imidazole interactions through hydrogen bonding. Additionally, the likely presence of π - π interactions is usually invoked to generate structure models of planar molecule stacks.^[199,200] These stack models contrast with the well-known chain-structure of solid imidazole^[168,169] and the question arises whether similar chain formation could also take place in larger 3-dimensional aggregates of imidazole in concentrated solutions where the availability of solvent molecules for the solvation of smaller structures may become limited (the reader is reminded of the graph presented in Figure 5). Indeed, recent molecular dynamics simulations for high concentrations (> 0.5 mol L⁻¹) of imidazole in aqueous solutions indicate that there is a concentration-dependent balance between π - π -assisted hydrogen-bonded stack structures and chains of hydrogen-bonded imidazole molecules^[202] that are similar to those found in liquid^[201] and solid^[168,169] imidazole. Moreover, apart from the molecular dynamics study of Liem *et al.*^[202] the expected concomitant influence of solvent molecules on the solute molecules has not been explicitly addressed in previous work, even though it would seem very likely that self-association is the result of significant synergy between imidazole-imidazole *and* imidazole-solvent interactions.

In a reversal of the approach taken in most previous studies, recent photoelectron spectroscopy investigations^[145-147] of concentrated (> 1 mol L⁻¹) aqueous imidazole solutions omitted imidazole-imidazole interactions and self-association effects from the analysis, while focusing on imidazole-water interactions in considerable detail. Valuable insight into the electronic structure of imidazole molecules in aqueous solution as a

function of pH was gained. The sensitivity of C 1s and N 1s core level spectroscopy to pH-induced protonation of imidazole was clearly demonstrated by detection of electronically equivalent N atoms in the imidazolium cation formed by protonation of imidazole under strongly acidic conditions.^[146,147] It was also attempted to explain the electronic structure of neutral imidazole species in solution through calculations of the electronic properties of microsolvated gas-phase clusters comprising a single imidazole molecule and up to five water molecules,^[145] providing insight into the effect of the nearest-neighbour water coordination shells on dissolved imidazole molecules. However, no quantitative agreement between predicted calculated electronic structure and experimental data was found. The study concluded that longer-range effects in the solvent probably need to be taken into account to obtain better agreement between theory and experiment. However, it would also be interesting to additionally include the influence of imidazole-imidazole interactions in the solution to the analysis of the core level spectra through the use of more complex structure models in the calculation of electronic properties. Such work will be reported in chapters 4 and 5 of this dissertation.

The N 1s core level excitation spectra of gas phase and solid imidazole have previously been determined experimentally and are therefore a useful reference for taking the first step towards understanding the electronic structure variations arising from imidazole-imidazole interactions. Apart from the results of a StoBe^[158] calculation of the N 1s core level shift between the N1 and N3 moieties in the gas phase imidazole monomer^[147] they have previously not been addressed in more detail by a calculation of the N K-edge spectra. The aim of the investigations to be presented here is to establish whether available methods for electronic structure calculations, especially StoBe, correctly reproduce the known experimental spectra, and whether such computational analysis of experimental core level spectra can realistically provide quantitative insight into condensed matter systems. One important question arising in this context is to establish whether the electronic transitions in the experimental excitation spectra are dominated by ground state ('initial state') properties of the imidazole molecules or whether excited state properties ('final state effects') influence the spectra significantly. Comparison will therefore be made also to ground state properties generated through state-of-the-art calculations using the CASTEP^[240,241] code by a collaboration partner at the University of Leeds.

3.2 Gas phase and solid state N K-edge spectra of imidazole

The N K-edge core level excitation spectra of imidazole in the gas phase and in the solid state have previously been published by Apen et al.^[170] They measured the fluorescence-yield (FY) and electron-yield (EY) NEXAFS spectra of solid imidazole as well as the gas phase inner-shell electron energy loss spectrum (ISEELS) of gas phase imidazole. Their data are reproduced in Figure 27.

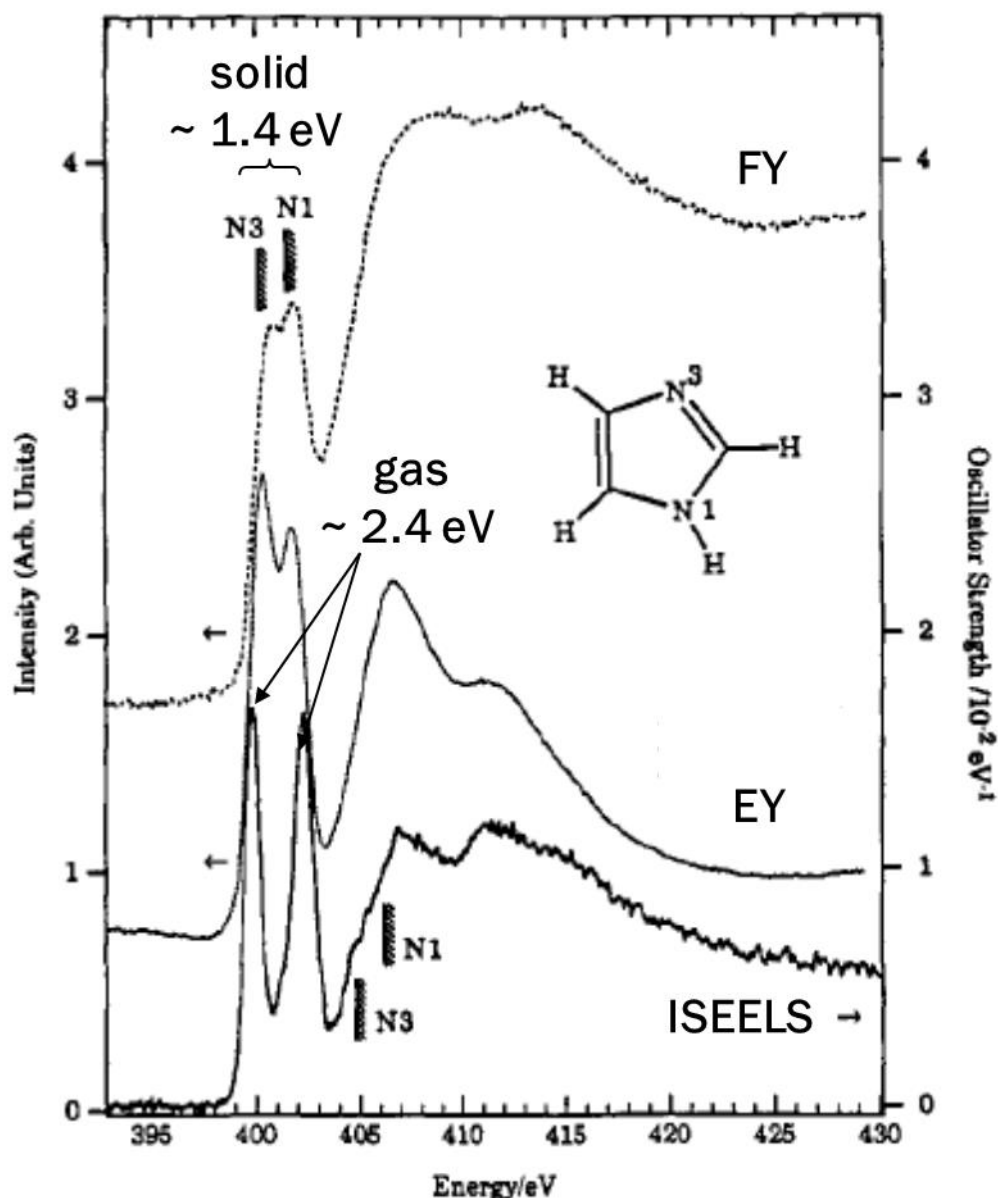


Figure 27 Fluorescence-yield (FY) and electron-yield (EY) NEXAFS spectra of solid imidazole in comparison with the gas phase inner-shell electron energy loss spectrum (ISEELS) of gas phase imidazole. Modified version of a figure taken from the paper by Apen et al.^[170]

We will omit fluorescence-yield data from further discussion, as it seems likely that these data of a pure solid phase are strongly affected by self-absorption effects^[96,101,242-247] that non-linearly reduce the intensity of all features in the spectra, but particularly the strong near edge resonances seen at energies of approximately 400-402 eV.

It can be seen that the most prominent features in the electron-yield and ISEELS data are the two strong near edge resonance which arise from the excitation of N 1s electrons from the N1 and the N3 moiety of the imidazole ring to unoccupied anti-bonding π^* -orbitals of aromatic ring system. The transition arising from the excitation of the N3 species always appear at a lower energy than that of the N1 atom, due to the transfer of electron density from H to N1 in the polarised N-H bond. As indicated in Figure 27, the energy shift between the two transitions is 1.4 eV in the case of the solid and 2.4 eV for the gas phase species. Also indicated are the ionisation potentials (IPs), which correspond to the N 1s binding energies relative to the energy of a free electron in vacuum. The differences between the N1 and N3 IPs of the solid and the gas are 1.35 eV and 1.3 eV, respectively. All these data are summarised in Table 8, which has been taken from the publication by Apen et al.^[170]

	XAS			assignment	
	FY	EY	ISEELS	N1	N3
1	400.6	400.4	399.9		1 π^*
2			401.3		2 π^*
3	401.7	401.8	402.3	1 π^*	
IP (solid)				401.5	400.15
IP (gas)				406.2	404.9
4			405.0 (sh)	Rydberg	
5	408.0	406.8	406.8	C-N σ^*	C-N σ^*
6	413.3	411.5	411.4	C-N σ^*	C-N σ^*
7			415	C-N σ^*	C-N σ^*

^a Estimated from IPs of like materials. ^b ISEELS energy scale calibration: -1.26(3) relative to N₂ 1s \rightarrow π^* .

Table 8 N 1s peak positions and assignments for the solid state and gas phase imidazole spectra shown in Figure 27. Adapted table taken from the paper by Apen et al.^[170].

3.3 Methodology

Calculations of the N K-edge core level spectra of gaseous and solid imidazole were carried out using the StoBe^[158] and CASTEP^[240] density functional theory (DFT) codes.

The StoBe code has already been introduced in section 2.7. The calculations were carried out as previously described by Aziz^[224] as well as Nolting et al.^[147] For the monomer structure a geometry-optimised imidazole monomer from Gaussian 03^[234] was used, which was obtained using the B3LYP/6-31G* basis set. This calculation also provided ground state molecular orbital energies and populations for the molecule. For the StoBe calculation of the solid state absorption spectrum a cluster cut-out from the crystal structure of imidazole was used, which is illustrated in Figure 31. All results for imidazole presented in the latter study could be reproduced quantitatively, providing confidence in the reliability and comparability of the independent calculations reported here. It should be noted that no energy-dependent progressive broadening was applied to the calculated spectra. Such energy-dependent broadening is often applied to calculate absorption edge spectra, to model the lifetime broadening that is experimentally observed. However, for the present study it was deemed more important that all predicted spectral features were clearly identifiable in the plots of the calculated results, to aid interpretation of the experimental data.

CASTEP calculations were carried out by C.R. Seabourne at the University of Leeds. CASTEP is based on the linear-augmented plane-wave (LAPW) methodology and originally used pseudopotentials to represent atomic core level wavefunctions because the strength of the code was intended to be the generation of highly accurate and detailed electronic structure in valence region of a material. Recent additions to the code permit to also calculate the electronic structure in the region of atomic core level.^[248-250] Seabourne used the generalized gradient approximation (GGA)^[251,252] for the calculation, applying his methodology previously developed in the context of analysing Al K-edges.^[253] Details of the calculation will be described in a forthcoming joint publication.^[254]

3.4 Results and Discussion

3.4.1 Imidazole gas phase monomer

The results of the StoBe calculation for the gas phase monomer are shown in Figure 28. Clearly visible are the two distinct near-edge peaks that stem from the calculated N1 and N3 contributions. It can be seen that the N3 moiety has a main peak at 400.1 eV and a notable additional peak at 401.2 eV (see below for a discussion of its origin). There is a split of 2.1 eV to the N1 main peak contribution at 402.3 eV, again with a noticeable

second peak contribution at 403.4 eV (see below). The corresponding core level binding energies calculated for both nitrogen atoms are 404.4 eV for N3 and 406.6 eV for N1.

These results are summarised in Table 9 and compared to the experimental data of Apen et al (Figure 27, Table 8).^[170]

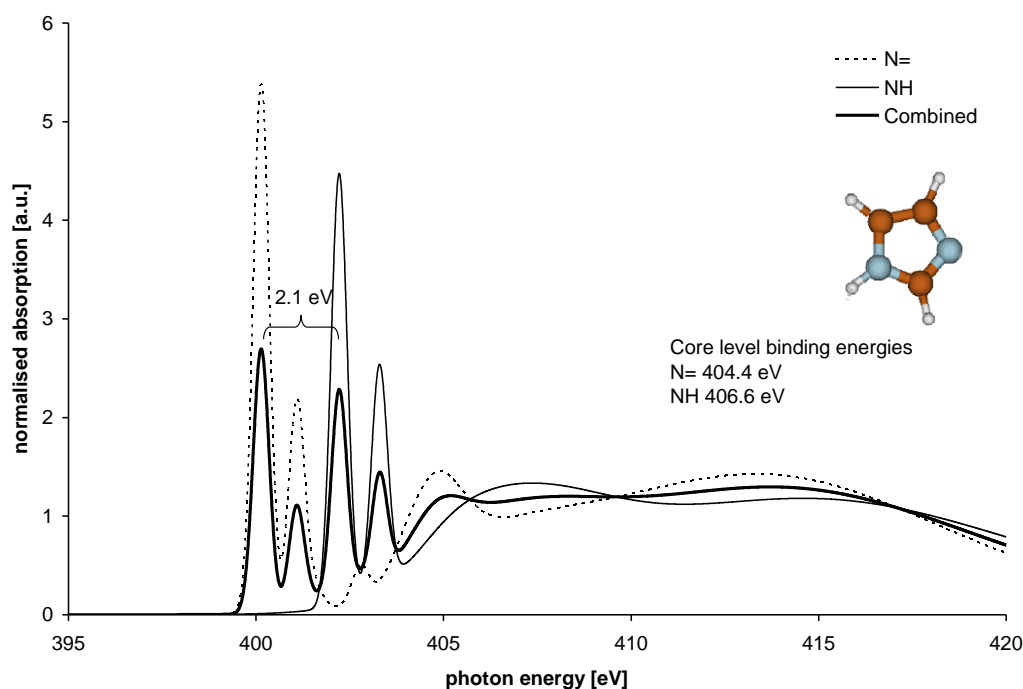


Figure 28 N K-edge NEXAFS spectrum of a gas phase imidazole monomer, as calculated with the StoBe code. Shown are the two individual absorption spectra of the two nitrogen moieties N1 (NH) and N3 (N=) in the molecule, and the combined spectrum, which can be compared to the experimentally observed ISEELS spectrum in Figure 27.

It can be seen that there is good agreement between the magnitude of the core level shift observed by ISEELS and that of the calculated spectrum. The IPs for the gas phase molecule reported by Apen et al deviate significantly from those predicted by StoBe, and especially the previously reported experimental value^[170] for the energy difference between the two IPs is only approximately half the predicted value. However, given that Apen et al state that their experimental IP values have only been estimated from “IPs of like materials” it would appear that this discrepancy should not be overemphasised. The almost quantitative agreement between the core level shift of 2.2 eV calculated by StoBe and the calculated splitting of 2.1 eV between the $1s \rightarrow \pi^*$ transitions of the two nitrogen atoms suggests that the difference between the calculated N 1s binding energies of the molecule explains the experimentally observed data, and that differential core hole

relaxation in the isolated molecule, as invoked by Apen et al for the explanation of the discrepancy between their experimental IP and $1s \rightarrow \pi^*$ shifts,^[170] may not be necessary to explain the discrepancy to their estimated IPs.

	Experimental / eV	Calculated (StoBe) / eV	Calculated (Gaussian) /eV
IP(N1)	406.2	406.6	n/a
IP(N3)	404.9	404.4	n/a
Δ IP	1.3	2.2	2.3
$E(\text{N1 } 1s \rightarrow 1\pi^*)$	402.3	402.3	392.5
$E(\text{N3 } 1s \rightarrow 1\pi^*)$	399.9	400.1	390.2
$\Delta E(1\pi^*)$	2.4	2.2	2.3
$E(\text{N1 } 1s \rightarrow 2\pi^*)$	n/a	401.2	393.7
$E(\text{N3 } 1s \rightarrow 2\pi^*)$	401.3	403.4	391.4
$E(2\pi^*) - E(1\pi^*)$	1.4	1.1	1.2

Table 9 Calculated and experimental IPs and $1s \rightarrow \pi^*$ transition energies for gas phase imidazole monomers.

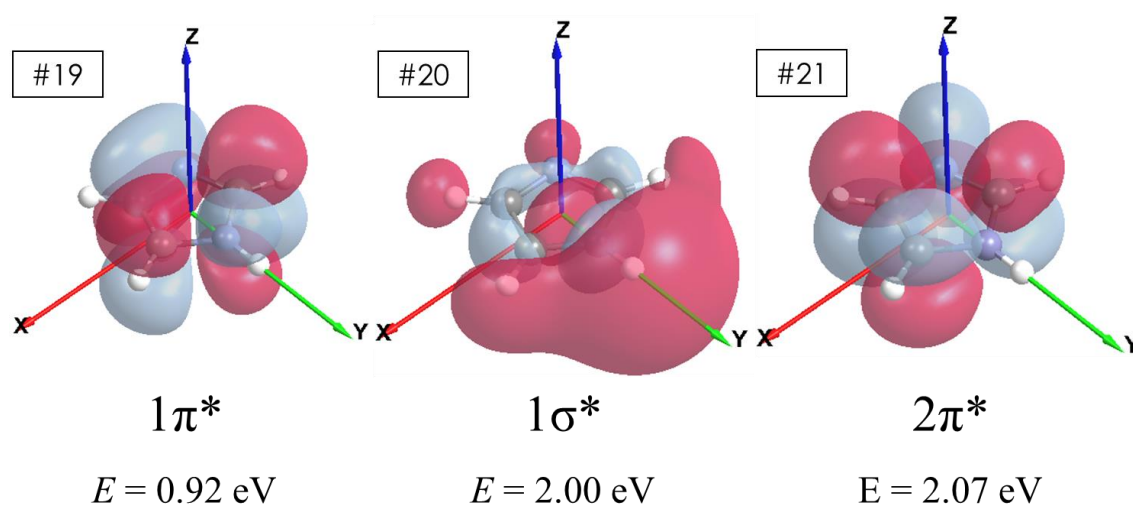


Figure 29 Electron density maps for the lowest unoccupied molecular orbital (LUMO) of imidazole #19 (left), the second-lowest unoccupied molecular orbital #20 (middle), and the third-lowest unoccupied molecular orbital #21 (right). Orbital energies are noted below each orbital.

The main observed N $1s \rightarrow \pi^*$ transitions correspond to the excitation of the $1s$ core electron into the lowest unoccupied molecular orbital (LUMO) of imidazole and should therefore be labelled N $1s \rightarrow 1\pi^*$. The ground state atomic and molecular orbital energies

of the imidazole molecule are summarised in Table 10. It can be seen that the N1-N3 1s core level shift in the ground state of imidazole is 2.3 eV, in good agreement with both the observed energy shift between the N 1s \rightarrow $1\pi^*$ transitions in the experimental data (2.4 eV) and with the results of the StoBe calculation (2.1 eV). It should be noted that the $1\pi^*$ state is the LUMO, which is visualised in Figure 29 together with the Gaussian-derived second- (#20) and third-lowest (#21) unoccupied MOs of the imidazole monomer.

Orbital #	Assignment	Energy / eV	
1	N1 1s	-391.602	
2	N3 1s	-389.337	
3	C2 1s	-278.531	Atomic core orbitals
4	C4 1s	-277.833	
5	C5 1s	-277.349	
6	σ	-27.449	
7	σ	-23.540	
8	σ	-20.117	Occupied molecular orbitals
9	σ	-16.638	
10	σ	-15.952	
11	σ	-15.265	
12	σ	-11.869	
13	σ	-11.761	
14	π	-11.549	
15	σ	-11.059	
16	π	-7.529	
17	σ	-7.101	
18	π	-6.129	Virtual (unoccupied) molecular orbitals
19	$1\pi^*$ (LUMO)	0.921	
20	$1\sigma^*$	1.998	
21	$2\pi^*$	2.065	

Table 10 Ground state molecular orbitals and their energies for an isolated imidazole molecule, as calculated by Gaussian 03.

Electronic transitions from the N 1s core levels to the σ^* orbital #20 should be weak and are therefore unlikely to be evident in experimental X-ray absorption spectra. However, the almost degenerate $2\pi^*$ orbital #21 could provide a final state with a high oscillator strength and provides an explanation for the occurrence of the secondary additional peaks seen in the data calculated with StoBe. The predicted ground state shift of 1.2 eV relative

to the $1\pi^*$ state matches excellently with the StoBe result for the difference between these two peaks (1.1 eV, Table 9). Because of lifetime broadening these transitions will probably be less conspicuous in the experimental data than the StoBe calculation suggests, but Apen et al did indeed notice a weak shoulder at around 401.3 eV between the main $1s \rightarrow 1\pi^*$ transitions in the ISEELS spectrum (Figure 27, Table 8) of gaseous imidazole, which they assigned to transitions to the $2\pi^*$ state. The energetic position of this feature was approximately 1.4 eV above the corresponding $N3 \rightarrow 1s 1\pi^*$ transition, which is in good agreement with the shift predicted by either StoBe or the Gaussian ground states (Table 9).

Overall, therefore, we can conclude from the analysis presented here that the relative energetic positions of all features observed in the experimental ISEELS spectrum are dominated by ground state electronic properties of the molecule. The deviations between predicted and experimentally observed energetic shifts are typically on the order of 0.2 eV to 0.3 eV, suggesting that the maximum magnitude of final state effects such as differential core hole relaxation are likely to be within this range as well.

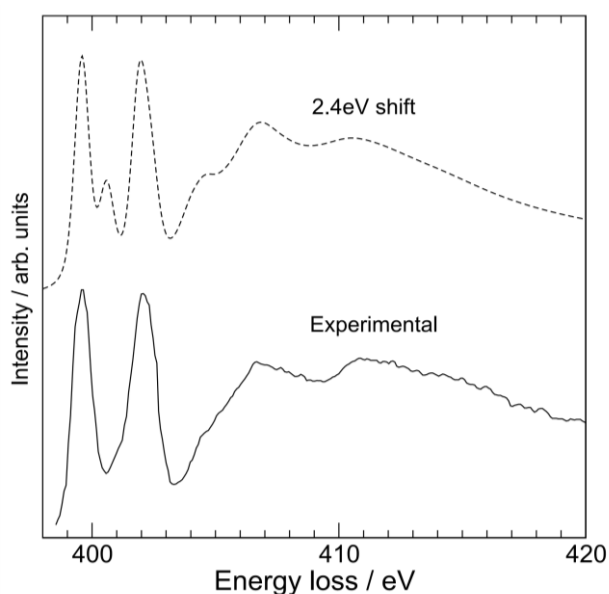


Figure 30 Comparison of experimental ISEELS^[170] and predicted N K-edges for an imidazole monomer, with an energetic shift of 2.4 eV between the two N 1s core level binding energies applied, as taken from experiment/StoBe. The theoretical spectrum was calculated with energy-dependent lifetime broadening and has been energetically shifted relative to the experimental result to obtain best energy match.^[255]

This conclusion is also borne out by the more advanced CASTEP analysis of the imidazole electronic by Seabourne.^[255] As can be seen in Figure 30, a calculated

spectrum based on the CASTEP ground state MO analysis and applying a core level binding energy shift of 2.4 eV leads to excellent agreement with the whole experimental spectrum of Apen et al.^[170], suggesting that ground state properties are the main determinant for the appearance of the spectrum. The secondary peak visible at about 401 eV in the calculated spectrum is again due to an overestimated transition to the $2\pi^*$ MO.

3.4.2 Crystalline imidazole

The most noticeable difference between the experimental spectra of gas phase and solid imidazole was the strong reduction of the energy split between the $1s \rightarrow 1\pi^*$ transitions of the N1 and the N3 moieties, which is 1.4 eV in the spectrum of the solid and 2.4 eV in the ISEELS spectrum of the gas phase (Figure 27, Table 8). The difference arises from the intermolecular N-H...N hydrogen bonding in the crystal structure, causing intermolecular redistribution of electron density from N3 to N1 sites through weakening of the N1-H bond, and a partial levelling of the electronic structure difference around the two N centres.

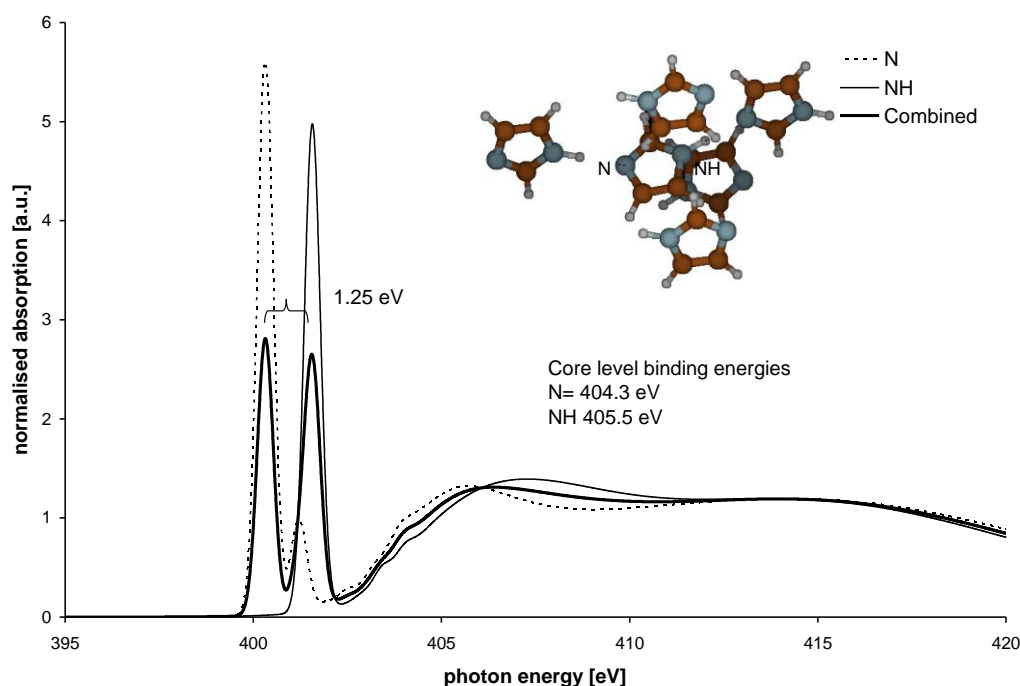


Figure 31 Calculated N K-edge NEXAFS spectrum of solid imidazole, as predicted by the StoBe code for the central molecule in a cluster of 6 molecules cut out from the crystal structure of imidazole. Shown are the two individual absorption spectra of the two nitrogen moieties N1 (NH) and N3 (N=) in the central molecule, as indicated in the cluster structure shown, and the combined spectrum, which can be compared to the experimentally observed electron-yield XAS spectrum in Figure 27.

The spectrum predicted by StoBe for the six-molecule cluster from the imidazole crystal structure is shown in Figure 31. The cluster of six molecules is shown in the figure as well. The calculated spectrum of the central imidazole molecule has an N3 (N=) $1s \rightarrow 1\pi^*$ transition at an energy of 400.0 eV and a small shoulder due to the $1s \rightarrow 2\pi^*$ transition at 400.8 eV. The N1 (NH) $1s \rightarrow 1\pi^*$ transition is evident as a single peak at 401.3 eV, with no noticeable shoulder contributions. Compared to the imidazole gas phase monomer the calculated $1s \rightarrow 2\pi^*$ transitions are weak, suggesting that the π - π interactions between the hydrogen-bonded chains of imidazole molecules in the crystal modify the π^* MOs of the molecules significantly.

The parameters describing the features in the experimental^[170] and calculated spectra are summarised in Table 11. Remarkable is the overall agreement between calculated and experimental data. The experimentally observed energy split $\Delta E(1\pi^*)$ of 1.4 eV between the two $1s \rightarrow 1\pi^*$ transitions is reproduced almost quantitatively. Comparing the StoBe results to those obtained for the gas phase monomer reveals further that most of the reduction in the energy split is due to a decrease of the IP of N1 (its N 1s core level binding energy) by 1.1 eV, from 406.6 eV to 405.5 eV. This indicates that the formation of intermolecular hydrogen bonds weakens the N1-H bond considerably, leading to the donation of electron density to the N1 centre and making it more electropositive. The IP of the N3 centre is much less affected, which may be evidence that the redistribution of electron density from the Brønsted acceptor to the N1 centre is in part compensated for also by a supply of electron density through the π - π interactions in the crystal structure. More systematic studies will be needed to elucidate this point further.

	Experimental / eV	Calculated (StoBe) / eV	Gas phase (Stobe) / eV
IP(N1)	401.5	405.5	406.6
IP(N3)	400.15	404.3	404.4
Δ IP	1.35	1.2	2.2
$E(\text{N1 } 1s \rightarrow 1\pi^*)$	401.8	401.3	402.3
$E(\text{N3 } 1s \rightarrow 1\pi^*)$	400.4	400.0	400.1
$\Delta E(1\pi^*)$	1.4	1.3	2.1

Table 11 Calculated and experimental^[170] IPs and $1s \rightarrow 1\pi^*$ transition energies for solid imidazole. For comparison the calculated gas phase monomer values previously reported in Table 9 are also included.

However, recent core level spectroscopy work from our group has found an N 1s core level shift of 1.6 eV for the two nitrogen ring moieties in the neutral imidazole side chain of solid histidine.^[256] This shift is larger than the IP difference observed in the experimental and calculated NEXAFS of solid imidazole. In the crystal structure of histidine both N centres of the imidazole ring take part in hydrogen bonding, albeit with the N1 centre donating its hydrogen to a more electronegative carboxylate acceptor (O), resulting in a shorter NH...O overall bond length of 2.77 Å, while the N3 centre is accepting from a the protonated primary amine group of the zwitterion with an overall NH...N distance of 2.88 Å.^[257] It is interesting that the overall stronger hydrogen bonding of the imidazole ring in this system does not seem to lead to an equally strong, or indeed stronger, levelling of the electron density at its N1 and N3 centres, supporting a view that all interactions in the crystal structure need to be taken into account to arrive at firm conclusions about the origin of differences between the N1 and N3 IPs in imidazole rings. Finally a more advanced CASTEP analysis of the imidazole electronic by Seabourne shall be shown for comparison.^[255] As can be seen in Figure 32, a calculated spectrum based on the CASTEP ground state MO analysis and applying a core level binding energy shift of 1.3 eV leads to excellent agreement with the experimental electron-yield NEXAFS spectrum of Apen et al.^[170], suggesting that ground state properties are the main determinant for the appearance of the spectrum in a similar way as they were in the case of the gas phase monomers.

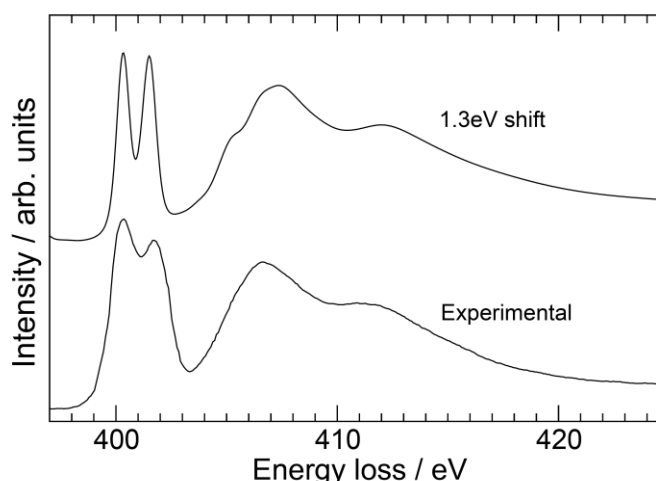


Figure 32 Comparison of experimental electron-yield XAS^[170] and predicted N K-edges for solid imidazole, with an energetic shift of 1.3 eV between the two N 1s core level binding energies applied. The theoretical spectrum was calculated by Seabourne^[255] with energy-dependent lifetime broadening and has been energetically shifted relative to the experimental result to obtain best energy match.

3.5 Conclusions

The N K-edge core level spectra of the gas phase monomer and of crystalline imidazole were found to be well reproduced by StoBe simulations of the experimental spectra as well as by ground state molecular orbital analysis based on Gaussian (gas phase monomer) and CASTEP (gas phase monomer and crystalline state). The main difference between the spectra of the gas phase monomer and crystalline imidazole is a reduction of the energy difference between the $1s \rightarrow 1\pi^*$ transitions at the two nitrogen centres of the aromatic ring in the crystal. The N1s core level binding energies (IPs) predicted by StoBe indicate that the main contributor to the reduction in the energy difference is the redistribution of electron density to the N1 site in the crystalline form. It appears that the redistribution of electron density in the solid state is complex, with the expected contributions from intermolecular hydrogen bonding but also contributions from π - π interactions between the hydrogen-bonded chains in the crystal. It was found to be unnecessary to invoke differential core hole relaxation in the gas phase monomers as an explanation for the observed difference. StoBe predicts weak $1s \rightarrow 2\pi^*$ transitions in the gas phase monomer, which appear to be in line with experimental observations and the energetic position of the ground state $2\pi^*$ orbital in Gaussian calculations. StoBe also reproduces the absence of such $2\pi^*$ features in the core level spectrum of solid imidazole. The success of the computational studies reported in this chapter provides a firm basis for the analysis of the even more complex interactions expected for aqueous imidazole solutions.

4. N K-edge NEXAFS of concentrated aqueous imidazole solutions ($c > 1 \text{ mol L}^{-1}$)

4.1 Introduction

Imidazole has a very high solubility in water, with concentrations up to almost 10 mol L^{-1} achievable^[187] and strong self-association effects well documented (see section 1.7.2). The structural properties of solutions with such high concentrations of solutes are an interesting topic for study in its own right and may provide insight into the self-assembly processes that take place just prior to the phase separation of solutes from solvents during nucleation and crystallisation processes. Imidazole is at the same time a hydrogen bond donor and acceptor, and previous investigations of imidazole solutions have therefore discussed their structure in terms of imidazole-imidazole interactions by hydrogen bonding, with additional π - π interactions often invoked to generate stacked structures.^[199,200] As already pointed out in section 3.1, these stack models contrast with the well-known chain-structure of solid imidazole^[168,169] and while the structural motif of hydrogen bonding and π - π interactions is plausible, there is little structural evidence supporting it, with the best available data coming from an X-ray scattering study by Gontrani et al.^[200] Most importantly, water can be expected to compete with imidazole for interaction by hydrogen bonding and the question arises whether the existing models are a complete representation of the local interactions that take place during the formation of the structure of concentrated imidazole solutions. The molecular dynamics simulations of Liem et al.^[202] indicated that in solutions of neutral imidazole species there is a concentration-dependent balance between π - π -assisted hydrogen-bonded stack structures and *chains* of hydrogen-bonded imidazole molecules similar to those in the crystalline imidazole solid.^[168,169] Recent photoelectron spectroscopy investigations^[145-147] of concentrated ($> 1 \text{ mol L}^{-1}$) aqueous solutions of neutral imidazole species at pH ~ 10.5 focused on imidazole-water interactions in considerable detail. The electronic structure of neutral imidazole species was examined through computational simulation of the experimental data with microsolvated gas-phase clusters of imidazole molecules surrounded by up to five water molecules.^[145] Quantitative agreement between predicted calculated electronic structure and experimental data was not achieved and it was

concluded that longer-range effects may have to be included to obtain better agreement between theory and experiment.

As already pointed out in section 3.1, an alternative approach to the interpretation of the photoelectron spectroscopy data may be to include additionally the imidazole-imidazole interactions that are well documented in the literature. Knowing the N 1s core level binding energies from the XPS study of Nolting et al.^[147] we can now apply NEXAFS to probe the electronic structure of imidazole in solution even more incisively.

In an extension of the previous work by photoelectron spectroscopy, this chapter therefore reports a NEXAFS study of concentrated imidazole solutions that contain neutral imidazole species. NEXAFS sensitively probes the local chemical environment around the X-ray absorbing atoms in the sample, so the aim of this study was to examine whether it is possible to gain additional evidence about the presence of imidazole-imidazole or imidazole-water interactions from these data by using the computational microsolvation cluster approach developed by Jagoda-Cwiklik et al.^[145,146] Through a computational examination of the core level spectra of hydrogen bonded imidazole-water dimers it was also examined how the hydrogen bond length to each of the two nitrogen centres in the imidazole ring affects the electronic structure of the molecule.

To support the analysis of the NEXAFS data an additional analysis of the solutions was carried out by Raman spectroscopy, with the aim of possibly obtaining evidence for changes in local interactions in the solution through analysis of the vibrational bands of imidazole.

4.2 Methodology

The imidazole solutions were prepared without adding any additives or adjustments of pH as described in section 2.1. The pH of the resulting solutions was already reported and discussed in section 2.2.3. It was found to be in the range around 10.5 where the speciation is expected to be 100% neutral imidazole.

Raman analysis was carried out as described in section 2.6. Solutions were dosed with a small pipette applying a single droplet onto a glass microscope slide. The slide was placed on the microscope table and spectroscopically examined as prepared.

NEXAFS measurements were carried out at BESSY-II as described in section 2.5, using the flow cell shown in Figure 25. Calculations of N K-edge NEXAFS spectra were

carried out using the StoBe^[158] code, which has already been introduced in section 2.7. The calculations were carried out as previously described by Aziz^[224] as well as Nolting et al.,^[147] using geometry-optimised imidazole-water dimers obtained with Gaussian 03^[234] (B3LYP/6-31G* basis set) and the microsolvated clusters previously examined by Jagoda-Cwiklik et al.^[145]

No energy-dependent progressive broadening was applied to the StoBe-calculated spectra. Energy-dependent broadening can be applied to model the lifetime broadening observable in the experimental spectra, but it was deemed more important that all predicted spectral features were clearly identifiable in the plots of the calculated results, rather than achieving best fit with the overall spectral envelope of the experimental data.

4.3 Results

4.3.1 Raman spectroscopy of imidazole solutions

As summarised in section 1.7.2, the Raman vibrational spectrum of imidazole is well known since the 1960s.^[179,258,259] A reference spectrum with an assignment of the most prominent vibrational bands is presented in Figure 33 and summarised in Table 12.

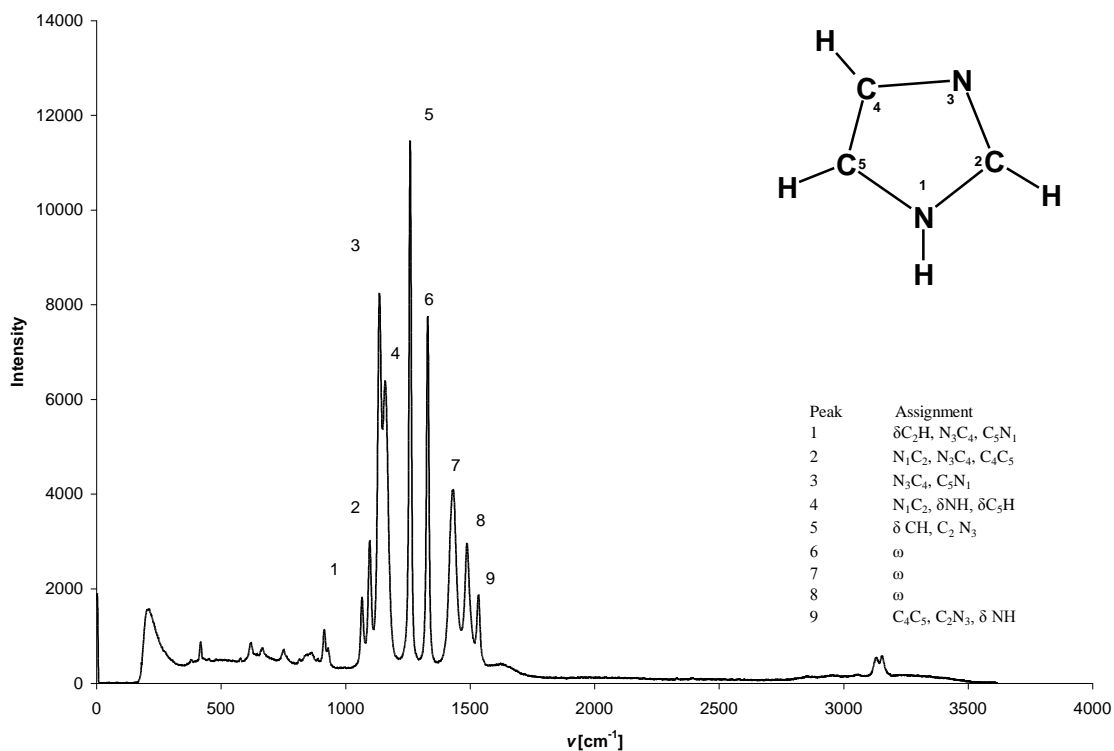


Figure 33 Raman assignments^[179,258,259] for bands between 1000 cm⁻¹ to 1800.cm⁻¹. See also table below. In plane vibrations ω = ring stretching, δ = bending ν = stretching, Δ = ring bending out of plane vibrations T = ring bending

ν [cm ⁻¹]	Assignment
626	T
674	T
917	Δ
1068	δ C ₂ H, N ₃ C ₄ , C ₅ N ₁
1098	N ₁ C ₂ , N ₃ C ₄ , C ₄ C ₅
1137	N ₃ C ₄ , C ₅ N ₁
1161	N ₁ C ₂ , δ NH, δ C ₅ H
1260	δ CH (bending), C ₂ N ₃
1331	ω
1434	ω
1490	ω
1536	C ₄ C ₅ , C ₂ N ₃ , δ NH
3149	V
3161	C ₅ H, C ₄ H, C ₂ H

Table 12 Summary of Raman vibrational bands^[179,258,259] including small spectral features at 626 cm⁻¹ and 3149 cm⁻¹

The results of the measurement are presented in Figure 34 and in Figure 35. The results obtained for the low concentrations of imidazole show that vibrational bands of imidazole are noticeable already at concentrations as low as 0.03 M. The intensities of all vibrational bands increase as the concentration of imidazole is increased.

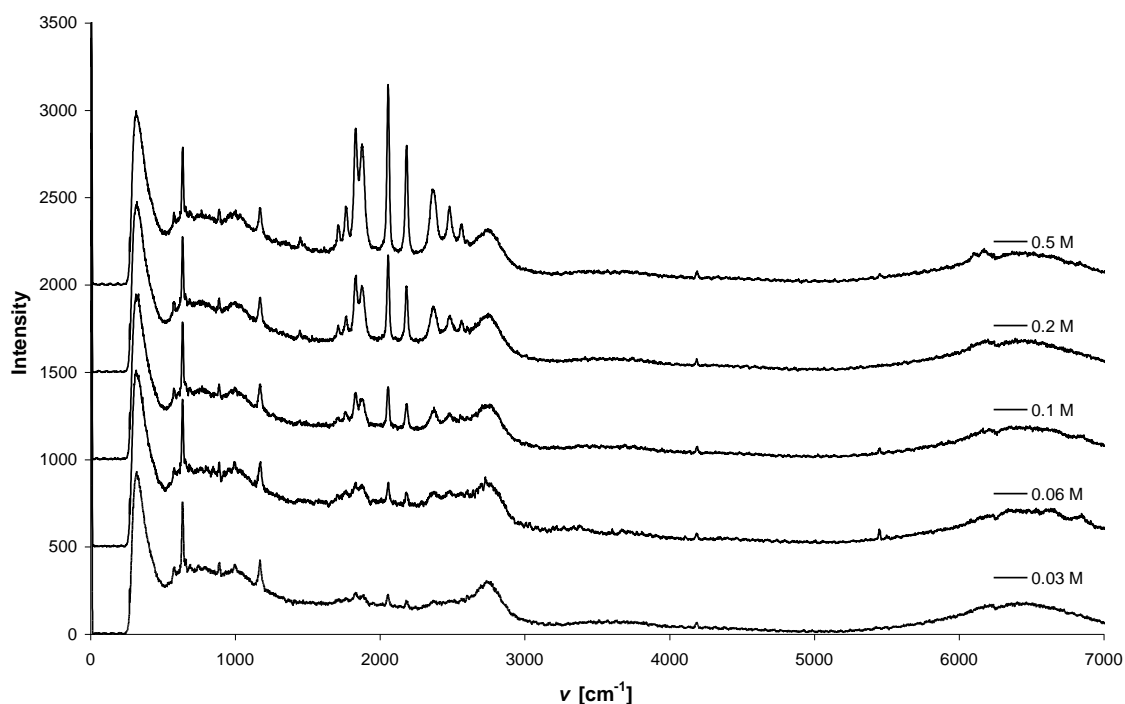


Figure 34 Raman spectra of aqueous imidazole solutions from 0.03 M to 0.5 M

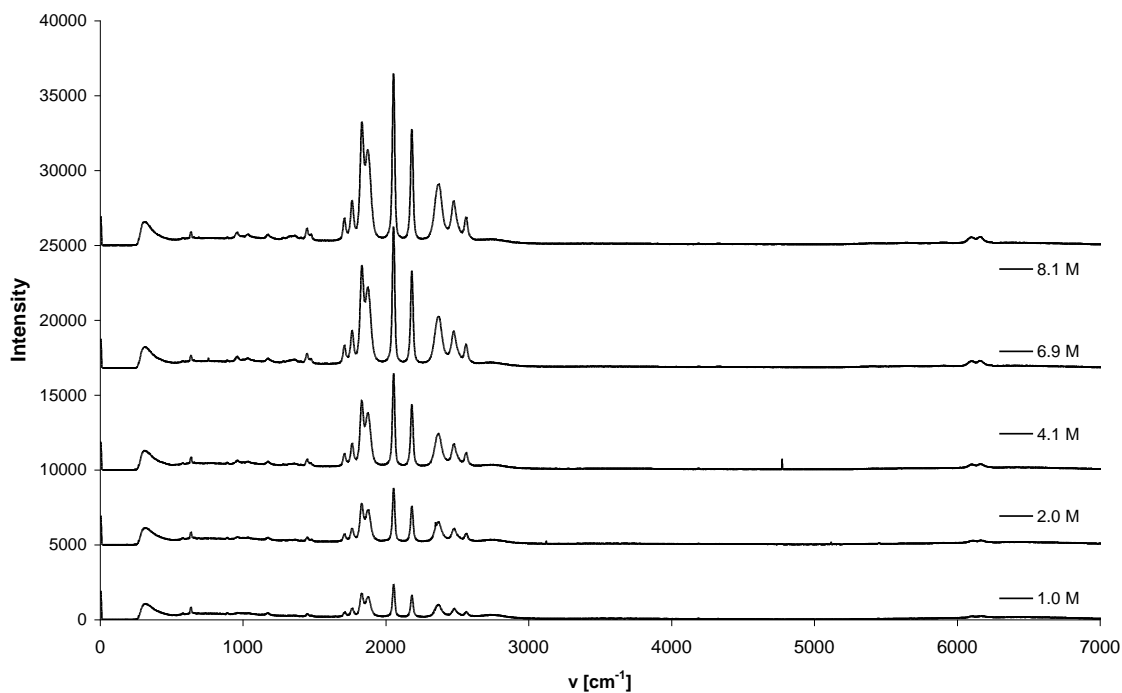


Figure 35 Raman spectra of aqueous imidazole solutions from 1.0 M to 8.1 M

Increasing the imidazole concentration further leads a gain in intensity for all vibrational bands, but their frequencies compare well with each other. Each band is equally well represented in all the solutions and there are no significant changes observable. These results suggest either that the local structure around imidazole molecules does not change significantly as the concentration is varied, or the vibrational modes detected by Raman scattering are not sensitive to local bonding variations.

4.3.2 N K-edge NEXAFS

Shown in Figure 36 are the obtained aqueous imidazole N K-edge near edge X-ray absorption fine structure (NEXAFS) spectra covering the concentration range from 0.50 mol L^{-1} ($\sim 100 \text{ H}_2\text{O}$ molecules per imidazole molecule, see Figure 5) to the saturation concentration of 8.20 M ($\sim 7 \text{ H}_2\text{O}$ molecules per imidazole molecule, see Figure 5). It can be seen that just as for the Raman analysis, any variations between the spectra at all examined concentrations are minor, indicating that the local coordination of imidazole molecules in this concentration range does not vary fundamentally.

The Raman and NEXAFS observations may have two explanations. The progressive self-association at higher concentration may involve only secondary interactions between

individually hydrated imidazole molecules, which do not manifest themselves in the N K-edge spectra; or very large assemblies of self-associated clusters are formed already at the lower end of the concentration range investigated here, in a quasi-phase separation process, so that any imidazole molecules added to the solution only increase the volume fraction of this phase. Both scenarios are of course not mutually exclusive and may occur simultaneously.

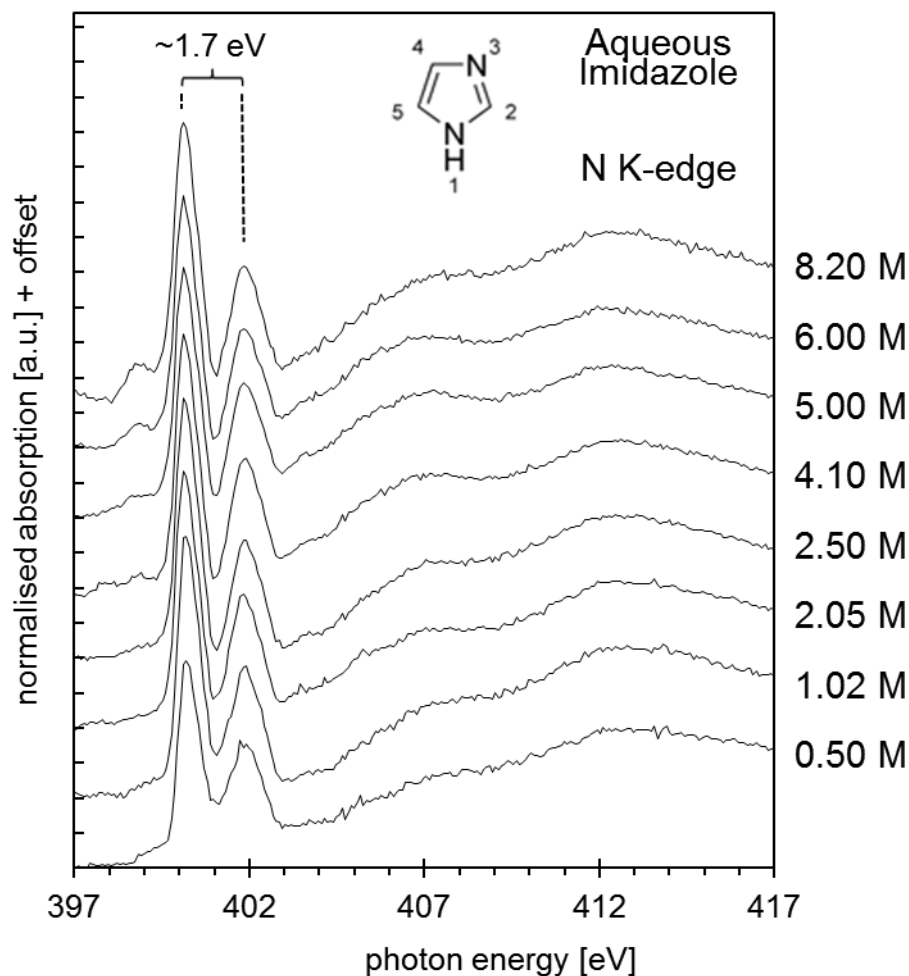


Figure 36 N K-edge near edge X-ray absorption fine structure (NEXAFS) spectra of aqueous imidazole solutions as a function of concentration from 0.5 mol L^{-1} to 8.2 mol L^{-1}

However, some more light can be shed on the possible structural nature of the solutions by examining the measured NEXAFS spectra in more detail. The NEXAFS spectra are dominated by two $1s \rightarrow 1\pi^*$ transitions of the N1 and N3 moieties in the imidazole ring, which appear at photon energies of approximately 400.3 eV and 402.0 eV (Figure 36). As discussed for monomeric and crystalline imidazole in chapter 3, the energy shift between these two transitions can be interpreted in terms of the 1s core level binding energy (BE)

difference between the two N atoms in the imidazole heterocycle.^[170] In line with this, it has also been shown that full protonation of imidazole in aqueous solutions leads to the equalisation of the two N 1s binding energies in the entirely symmetric imidazolium cation.^[147] At the time, the equivalence of the N 1s binding energies was supported by a calculation of its value with the StoBe code.^[147] The corresponding NEXAFS spectrum has been calculated for the present work and is shown in Figure 37 below. Note from the data in the inset that the N 1s binding energy value (412.5 eV) reported by Nolting et al.^[147] is almost quantitatively reproduced. The N 1s core level binding energy is approximately 8 eV higher than for the non-protonated monomer examined in section 3.4.1. This is due to the unshielded positive charge on the isolated gas phase cation, which would be strongly reduced by electrostatic and/or bonding stabilisation in the presence of a polar and/or protic solvent, respectively.

The photon energy difference for the appearance of the two N 1s \rightarrow $1\pi^*$ transitions in Figure 36 is 1.7 eV. This value differs from the previously observed energy shift between the two peaks in both gas phase imidazole monomers and the solid state of imidazole. These reference values were already examined in detail in chapter 3, where it was shown that calculations of the N K-edge absorption spectra with StoBe^[109] reproduce them near-quantitatively. The solid state value for the energy difference is \sim 1.4 eV^[170], which is lower than the value of 1.7 eV observed in the solution. The gas phase monomer value is \sim 2.4 eV^[170], which is much higher than the solution value. That the solution value is closer to that of the strongly hydrogen-bonded solid state structure suggests that significant intermolecular interactions with surrounding water or imidazole molecules take place. Since the extent of proton transfer is insignificant in the pH range of the solutions (pH \sim 10.5, see Figure 6 and Figure 17) it is reasonable to suggest that the observed energy difference of 1.7 eV must be due to imidazole-water and imidazole-imidazole interactions, most likely through hydrogen bonding.

It is worthy to note at this point that the observed split of 1.7 eV between the N 1s \rightarrow $1\pi^*$ transitions at the N1 and N3 centres matches perfectly with the previously reported^[147] difference between the N 1s photoemission peaks of an 1 mol L⁻¹ imidazole solution (Figure 16). This observation would be entirely in line with the conclusion drawn in chapter 3, that chemical shifts observed in the N 1s NEXAFS spectra of imidazole are dominated by the chemical shifts in the associated core level binding energies, and that the influence of final state effects is secondary.

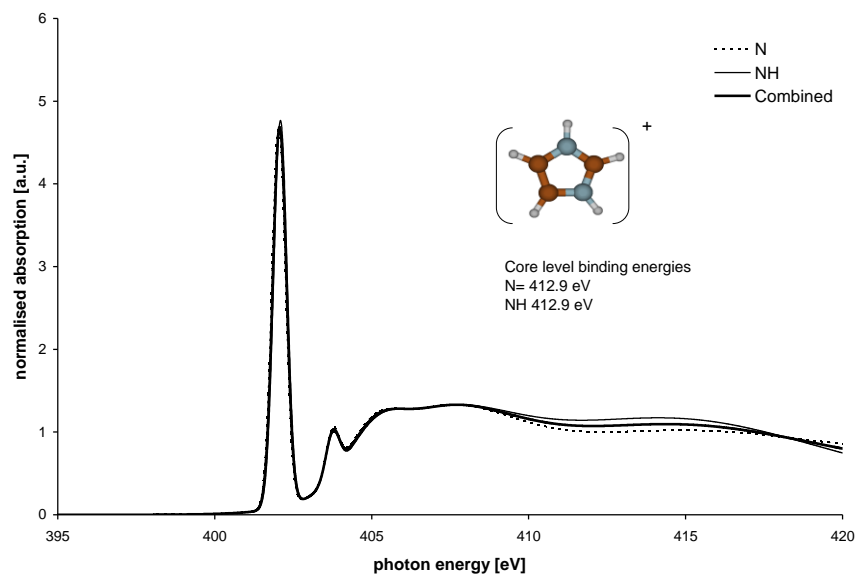


Figure 37 Calculated N K-edge absorption spectrum of the imidazolium cation.

The effect of imidazole-imidazole interactions on the NEXAFS of the crystalline state has already been discussed in some detail in section 3.4.2. A combination of hydrogen-bonding and π - π interactions was found to lead to the strong reduction of the energy difference between the N $1s \rightarrow 1\pi^*$ transitions from the two nitrogen centres in the imidazole ring, with electronic modification of the N1 site being the dominant contributor to the observed changes. For the remainder of this chapter the effect of imidazole-water interactions shall therefore be explored more systematically, in a similar way to the approach taken in previous XPS work on aqueous imidazole.

4.3.3 Imidazole-water dimers: influence of the donor-acceptor bond length

StoBe simulations were carried out for imidazole water dimers including a water molecule either bound to the N1 or the N3 centres of the imidazole ring. First, geometry optimised equilibrium structures were obtained using Gaussian, and then the distance between water and imidazole varied to examine its effect on the core levels and the NEXAFS spectrum.

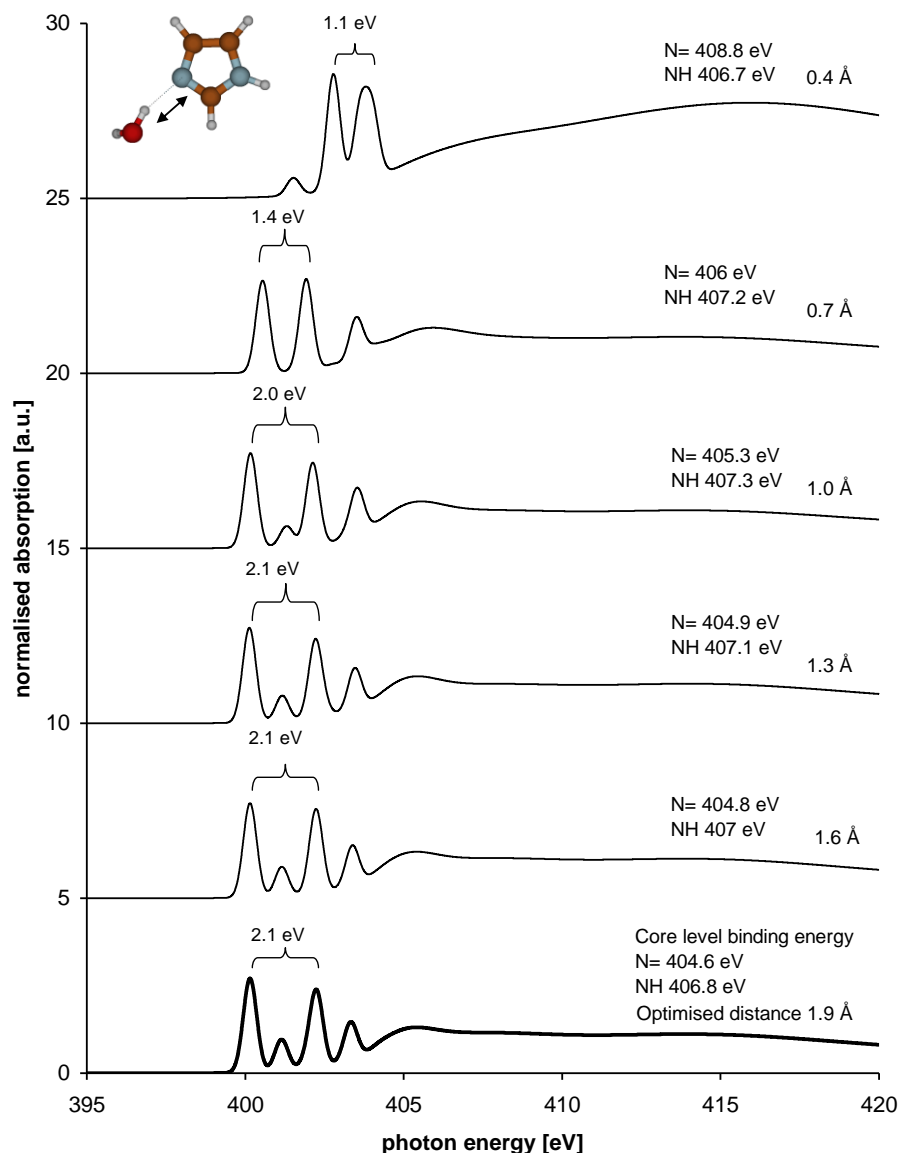


Figure 38 Calculated N K-edge NEXAFS spectra of imidazole·H₂O gas phase clusters under variation of the HOH...N₃ (N=) distance. Corresponding N 1s core level binding energies of the two N atoms are noted alongside each spectrum.

The results calculated during variation of the HOH...N₃ (N=) distance are displayed in Figure 38. It can be seen that the absorption spectrum is significantly affected only when the H...N₃ distance becomes shorter than about 1 Å, which is much shorter than one would expect for a hydrogen bond. Examination of the N₁ 1s and N₃ 1s core level binding energies (Figure 39) reveals that this on first sight surprising result stems from the fact that for distances larger than 1 Å any modification of the electronic state of the N₃ centre is equally exhibited by the N₁ centre in the ring. It appears that any charge withdrawn from the N₃ centre by hydrogen bonding to water is delocalised across the whole imidazole ring, resulting in a zero net effect on the energy difference between the

two N 1s \rightarrow $1\pi^*$ transitions. The small magnitude of the shifts in the absolute N3 1s binding energy is also entirely in line with the observation made in section 3.4.2 that the electronic state of the N3 centre in the solid state is quite insensitive to the effect of intermolecular imidazole-imidazole hydrogen bonding to the H-N1 centres of neighbouring imidazole molecules. The hydrogen...N3 distance in the imidazole crystal structure is 1.83 Å, which, according to Figure 39, is almost certainly out of the range in which significant modification of the electronic state of the N3 centre is expected to take place.

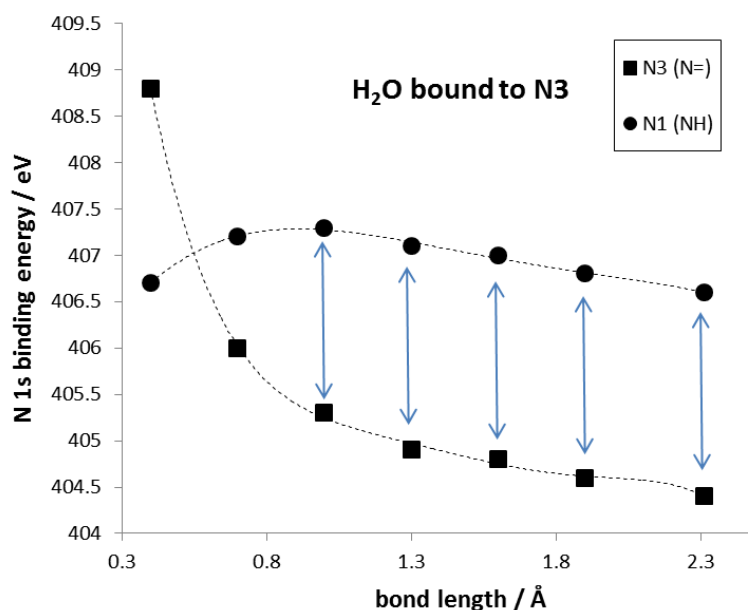


Figure 39 Calculated N 1s core level binding energies of the N-atoms in imidazole·H₂O gas phase clusters under variation of the HOH...N3 (N=) distance.

When calculations are performed as a function of the variation of the H₂O...N1 (NH) distance, different behaviour is observed (Figure 40). It can be seen that the absorption spectrum is significantly affected already when the O...N1 distance becomes shorter than about 1.6 Å, which is within the range one would expect for a hydrogen bond. Examination of the N1 1s and N3 1s core level binding energies (Figure 41) reveals that the 1s binding energy of the N1 centre strongly reduces as the H₂O molecule is brought closer, while the N3 centre is quite insensitive to its presence, suggesting that the electron density variation is delocalised through the aromatic system of the imidazole ring, resulting in a significant net effect on the energy difference between the two N 1s \rightarrow $1\pi^*$ transitions. Again, the small magnitude of shifts seen in the absolute N3 1s binding energy is entirely in line with the previous observations.

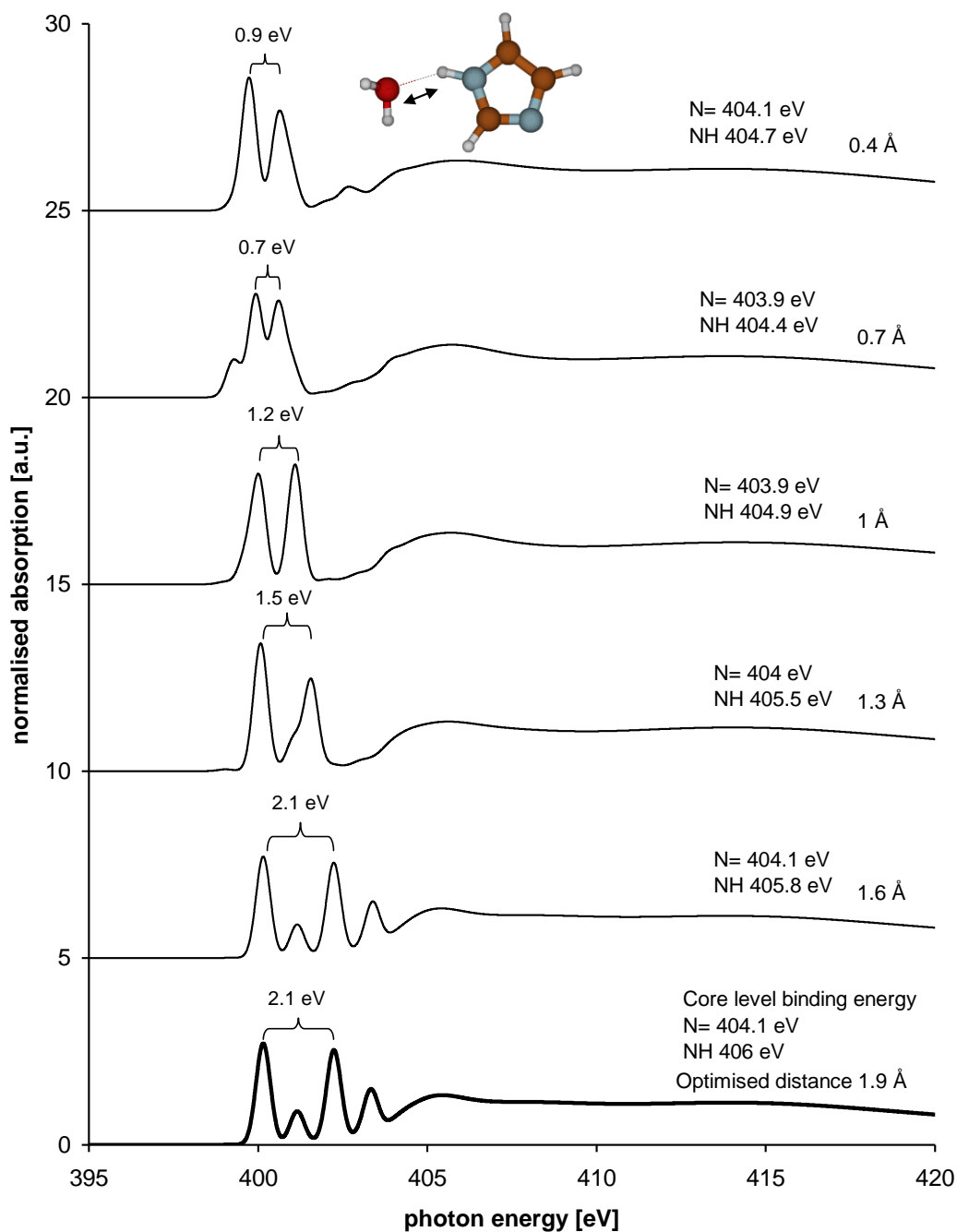


Figure 40 Calculated N K-edge NEXAFS spectra of imidazole·H₂O gas phase clusters under variation of the H₂O...HN distance. Corresponding N 1s core level binding energies of the two N atoms are noted alongside each spectrum.

Any hydrogen donor approaching the N3 centre in the imidazole ring plane will experience interaction with the electron density of the imidazole molecule at a similar distance as an acceptor approaching the N1-H centre. It seems likely, however, that the emerging pattern of different donor-acceptor effects at the two N centres has its roots in the fact that interaction with the N1-H centre takes place primarily by modification of the

localised N-H σ -bond, while the interaction at the N3 centre takes place through the sp^2 electron density of the lone pair that is located at the N3 atom. Consequently intra-atomic charge redistribution can take place at N3, permitting the distribution of charge into the aromatic ring system. In contrast, redistribution of charge from the N-H σ -bond at N1, which is entirely decoupled from the aromatic system, would require significant changes in molecular geometry and does therefore not take place as readily.

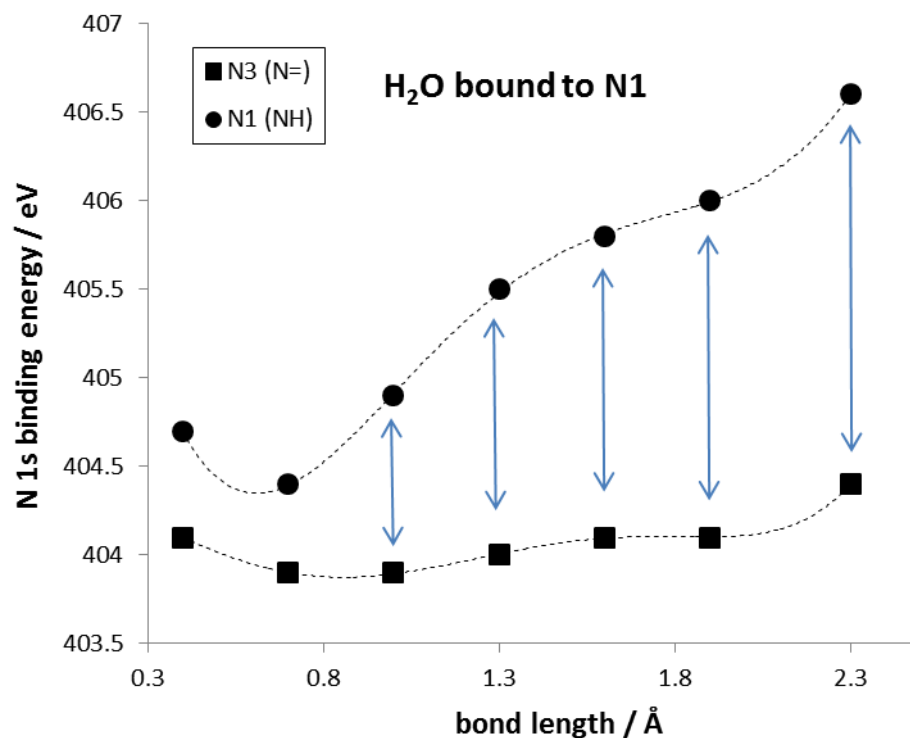


Figure 41 Calculated N 1s core level binding energies of the N-atoms in imidazole·H₂O gas phase clusters under variation of the H₂O...HN1 distance.

4.3.4 Analysis using microsolvation clusters

Going beyond the simple dimer studies in the previous section, the microsolvated cluster structures reported by Jagoda-Cwiklik et al.^[145] shall now be examined. We start with the hydrogen-bonded HOH ...N3 1.9 Å ('N=') dimer ('Imi 1 wat v5') that was already the basis for some of the investigations in the previous section. In line with the previous results it can be seen (Figure 42) that the effect on the calculated NEXAFS spectrum is negligible: the N1/N3 1s → 1π* peak energy difference, and the overall shape of the calculated spectrum, are essentially the same, with all spectral features being almost identical to that of the imidazole monomer reported in chapter 3 (Figure 28). The core level binding energies of the N3 (N=) and N1 (NH) centres remain very similar to the monomer binding energies with only a slight shift of 0.3 eV to 406.9 eV for N1 and 404.7 eV for N3.

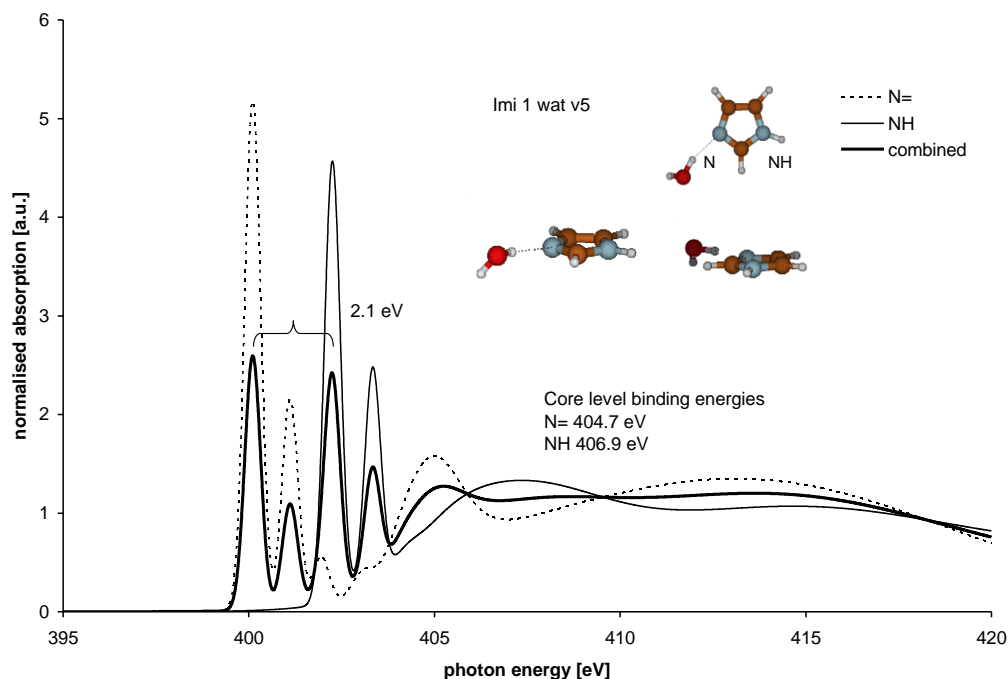


Figure 42 Calculated N K-edge NEXAFS spectrum of the geometry-optimised imidazole·H₂O gas phase imidazole/water cluster 'Imi 1 wat v5' of Jagoda-Cwiklik et al.^[145] The inset shows the cluster along the three Cartesian axes and reports the 1s core level binding energies of the two N atoms.

Addition of another water molecule leads to the cluster 'Imi 2 wat v7' which exhibits some subtle differences to the monomer (Figure 43). Although again the spectral features are similar there is a reduction of the N1/N3 1s → 1π* peak energy difference by 0.1 eV

compared to the monomer. Interestingly it appears that the N1 contribution has shifted by 0.1 eV with the addition of the extra bound water in the vicinity of the N3 centre.

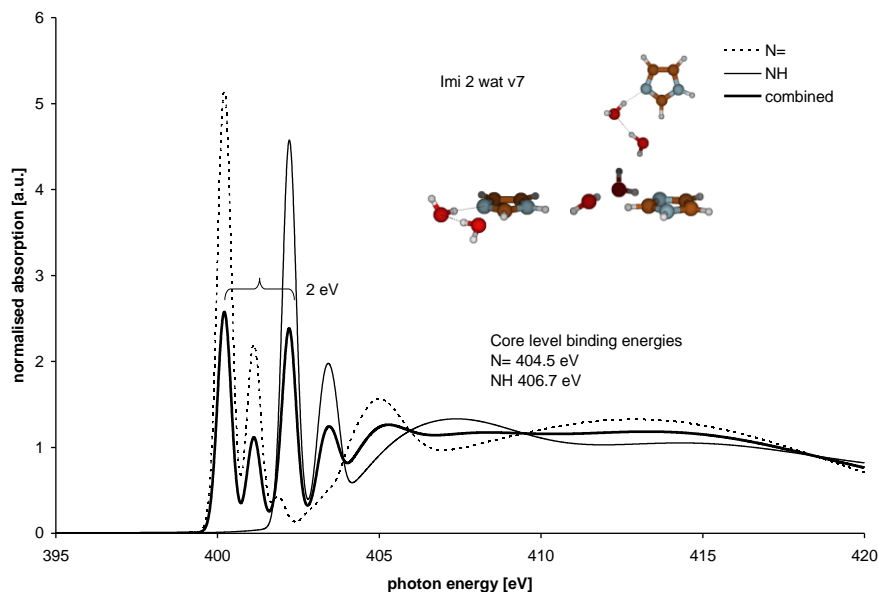


Figure 43 Calculated N K-edge NEXAFS spectrum of the geometry-optimised imidazole·2H₂O gas phase imidazole/water cluster ‘Imi 2 wat v7’ of Jagoda-Cwiklik et al.^[145] The inset shows the cluster along the three Cartesian axes and reports the 1s core level binding energies of the two N atoms.

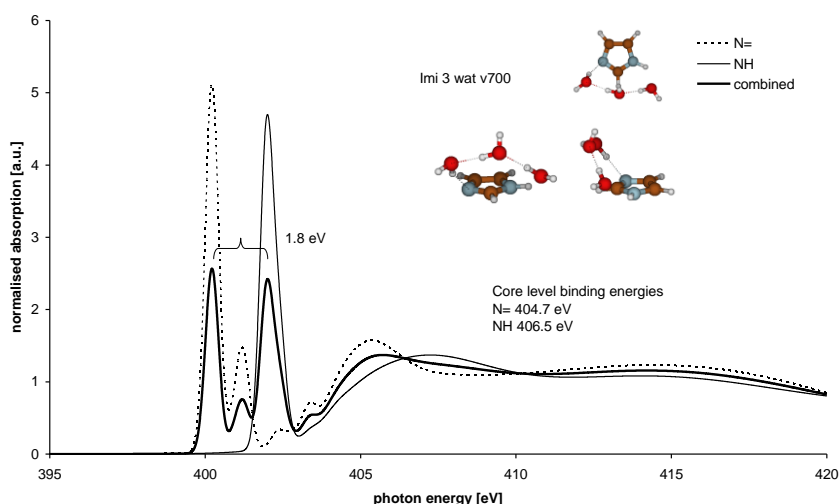


Figure 44 Calculated N K-edge NEXAFS spectrum of the geometry-optimised imidazole·3H₂O gas phase imidazole/water cluster ‘Imi 3 wat v700’ of Jagoda-Cwiklik et al.^[145] The inset shows the cluster along the three Cartesian axes and reports the 1s core level binding energies of the two N atoms.

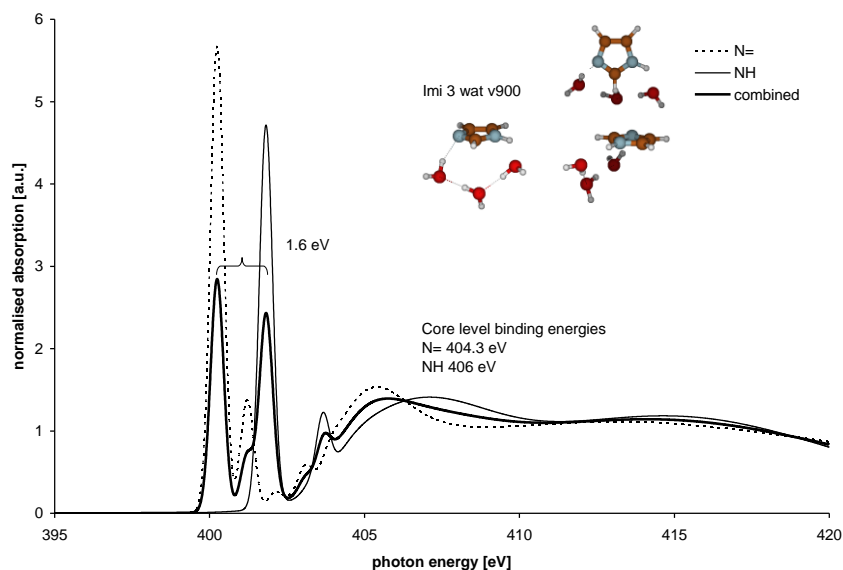


Figure 45 Calculated N K-edge NEXAFS spectrum of the geometry-optimised imidazole·3H₂O gas phase imidazole/water cluster ‘Imi 3 wat v900’ of Jagoda-Cwiklik et al.^[145] The inset shows the cluster along the three Cartesian axes and reports the 1s core level binding energies of the two N atoms.

Adding a third water molecule to the cluster led Jagoda-Cwiklik et al to two equilibrium structures, ‘Imi 3 wat v700’ (Figure 44) and ‘Imi 3 wat v900’ (Figure 45). These spectra show first significant changes compared to the monomer. The secondary peaks arising from the N1/N3 1s \rightarrow 2 π^* transitions are barely visible in these spectra now, indicating that aromatic π system of the imidazole molecule is significantly modified by the presence of three water molecules. The calculated N1/N3 1s \rightarrow 1 π^* peak energy differences are reduced significantly from the monomer value of 2.1 eV, to 1.8 eV and 1.6 eV, respectively. These values, along with the corresponding N 1s core level binding energy differences of 1.8 eV and 1.7 eV, are actually in excellent agreement with our NEXAFS data and with the N 1s binding energies previously reported.^[147] However, this seemingly excellent result should not be overinterpreted. First, the electronic structure of these clusters did not satisfactorily model the vertical ionisation potentials observed in the previous photoemission study.^[145] Second, it seems unlikely that imidazole in aqueous solution will be solvated by only three water molecules; and third, as we will see over the following pages, adding more water molecules to the microsolvation clusters continues the trend towards a levelling of the binding energy difference between the N1 and the N3 centres. All this indicates that the found agreement with the energetic positions of the observed core level features is serendipitous.

As can be seen in the progression of figures on the following pages (Figure 46 to Figure 50), adding additional water molecules to yield solvate shells with 4 and 5 solvent molecules has the effect of further reducing the N1/N3 $1s \rightarrow 1\pi^*$ peak energy difference, with the 5 water hydration shell producing a peak split of 1.3 eV. The combined spectra are summarised once more in Figure 51, while Table 13 summarises the calculated core level binding energies and $1s \rightarrow 1\pi^*$ transition energies obtained from the StoBe cluster calculations.

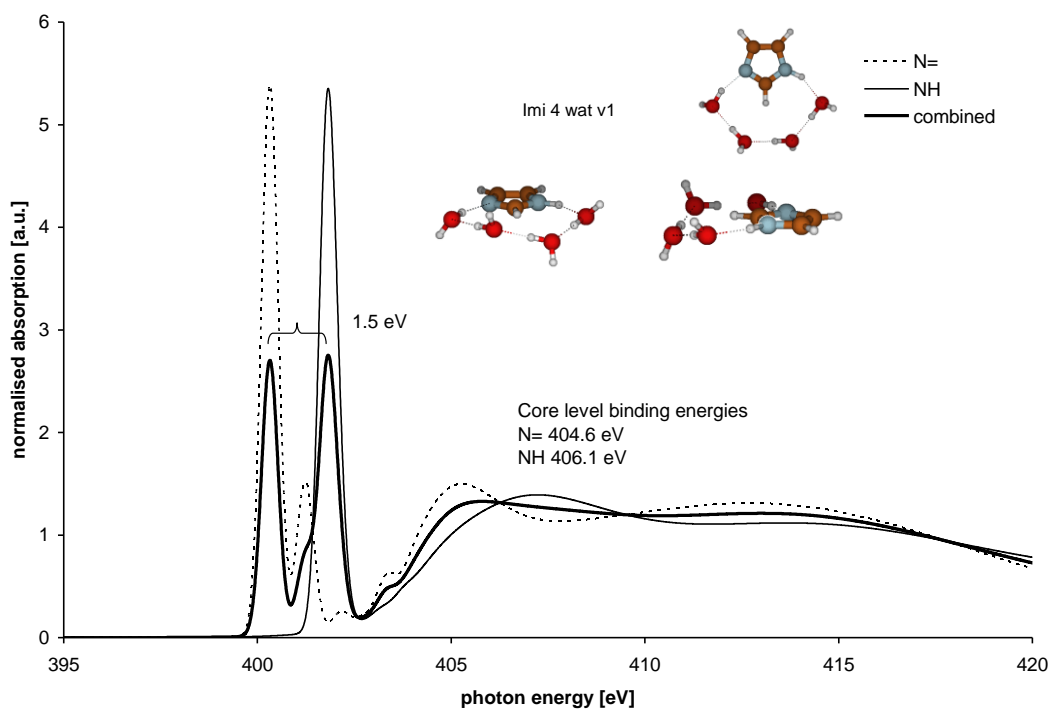


Figure 46 Calculated N K-edge NEXAFS spectrum of the geometry-optimised imidazole·4H₂O gas phase imidazole/water cluster 'Imi 4 wat v1' of Jagoda-Cwiklik et al.^[145] The inset shows the cluster along the three Cartesian axes and reports the 1s core level binding energies of the two N atoms.

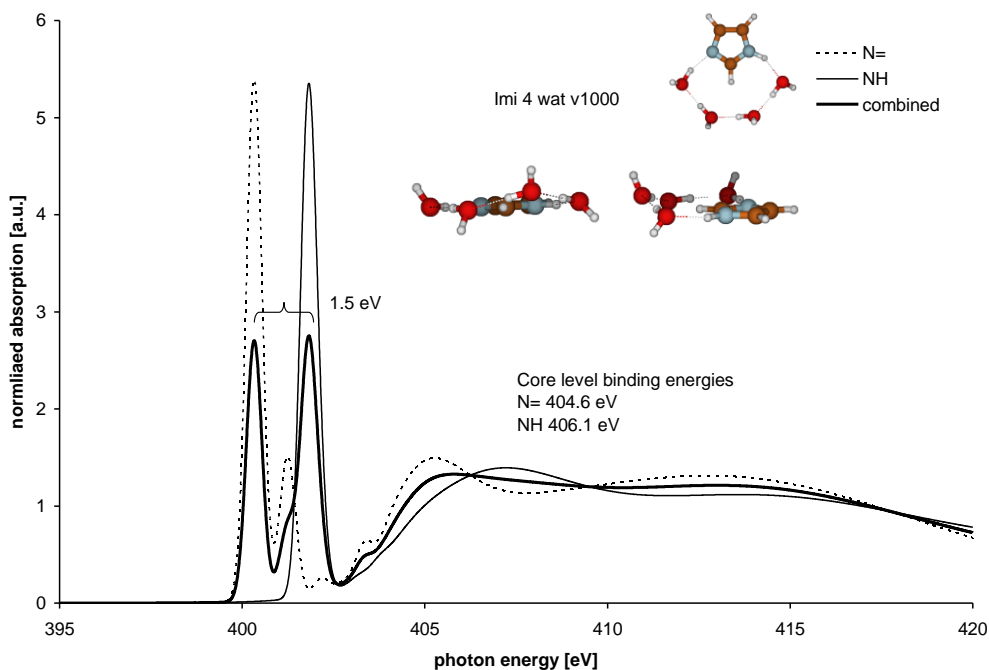


Figure 47 Calculated N K-edge NEXAFS spectrum of the geometry-optimised imidazole·4H₂O gas phase imidazole/water cluster ‘Imi 4 wat v1000’ of Jagoda-Cwiklik et al.^[145] The inset shows the cluster along the three Cartesian axes and reports the 1s core level binding energies of the two N atoms.

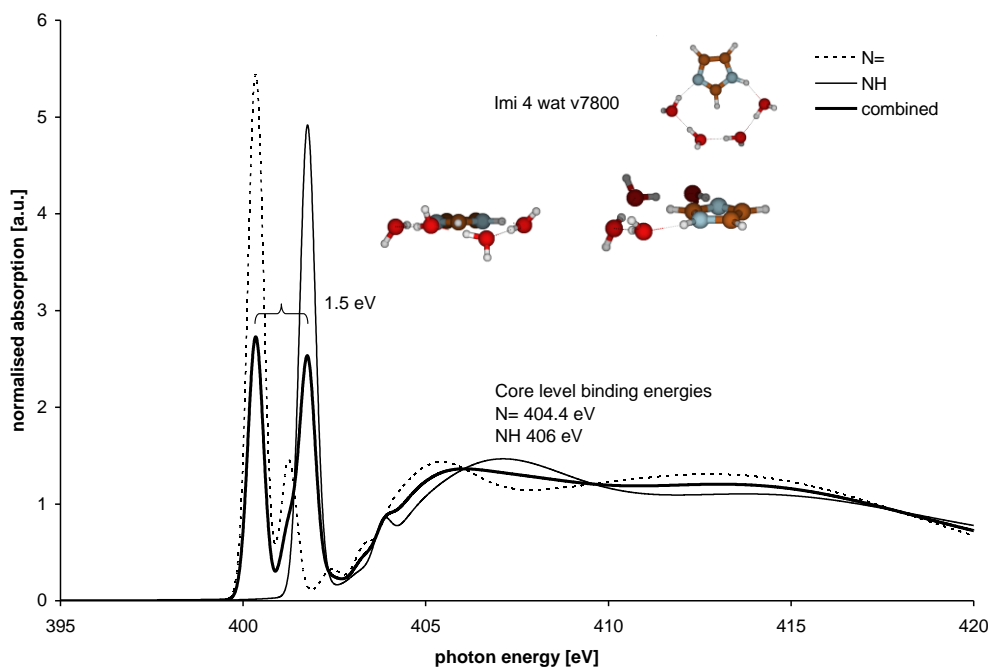


Figure 48 Calculated N K-edge NEXAFS spectrum of the geometry-optimised imidazole·4H₂O gas phase imidazole/water cluster ‘Imi 4 wat v7800’ of Jagoda-Cwiklik et al.^[145] The inset shows the cluster along the three Cartesian axes and reports the 1s core level binding energies of the two N atoms.

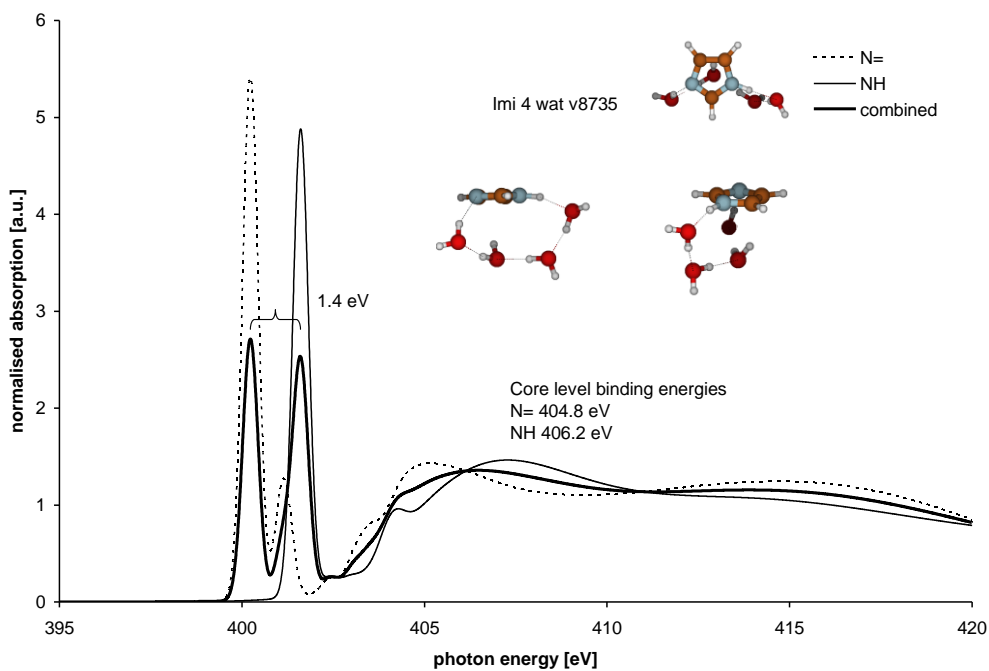


Figure 49 Calculated N K-edge NEXAFS spectrum of the geometry-optimised imidazole·4H₂O gas phase imidazole/water cluster ‘Imi 4 wat v7835’ of Jagoda-Cwiklik et al.^[145] The inset shows the cluster along the three Cartesian axes and reports the 1s core level binding energies of the two N atoms.

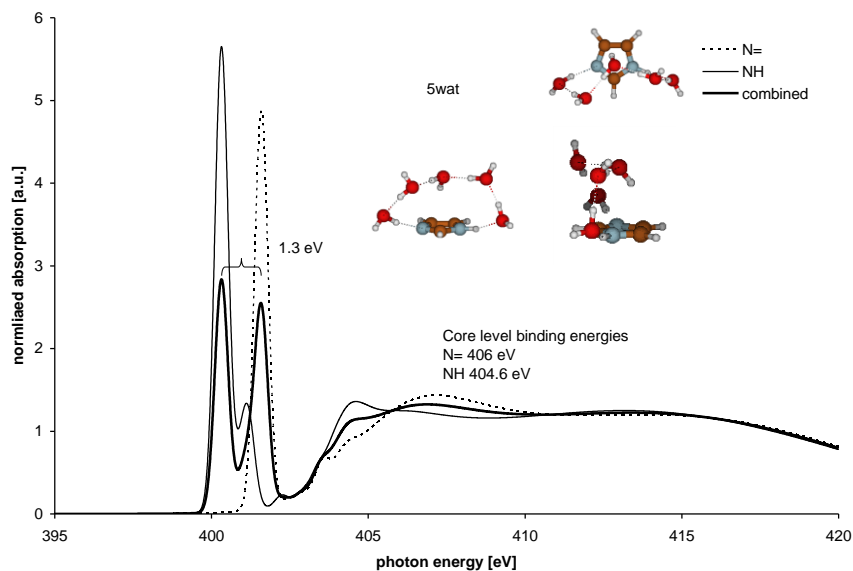


Figure 50 Calculated N K-edge NEXAFS spectrum of the geometry-optimised imidazole·5H₂O gas phase imidazole/water cluster ‘5wat’ of Jagoda-Cwiklik et al.^[145] The inset shows the cluster along the three Cartesian axes and reports the 1s core level binding energies of the two N atoms.

Composition	Name	N 1s BE		Δ N 1s	NEXAFS
		N1	N3	BE	E(N1) – E(N3)
imidazole·H ₂ O	Imi 1 wat v5	406.9	404.7	2.2	2.1
imidazole·2H ₂ O	Imi 2 wat v7	406.7	404.5	2.2	2.0
imidazole·3H ₂ O	Imi 3 wat v700	406.5	404.7	1.8	1.8
	Imi 3 wat v900	406.0	404.3	1.7	1.6
imidazole·4H ₂ O	Imi 4 wat v1	406.1	404.6	1.5	1.5
	Imi 4 wat v1000	406.1	404.6	1.5	1.5
	Imi 4 wat v7800	406.0	404.4	1.6	1.5
	Imi 4 wat v7835	406.2	404.8	1.4	1.4
imidazole·5H ₂ O	Imi 5 wat	406.0	404.6	1.4	1.3

Table 13 Calculated N1s core level binding energies and energy difference between the N1 ('NH') and N3 ('N=') 1s \rightarrow 1 π^* NEXAFS bands for the imidazole N atoms in the geometry-optimised gas phase imidazole/water clusters of Jagoda-Cwiklik et al.^[145].

It is evident from these data that inclusion of larger hydration shells leads to a stronger than experimentally observed effect on the levelling of the N 1s core level energy difference between the two nitrogen centres. It may be speculated that one contribution to this result may be the asymmetric and incomplete coordination of the imidazole molecules in models invoking so few water molecules. It may be that in real solutions electron density variations induced by hydrate coordination from one side of the molecule are counterbalanced by coordination from the other, leading to an overall weaker net effect on the electronic structure of the central imidazole molecule. This idea shall be explored next. Furthermore, as has been pointed out a few times already, it is known that self-association of imidazole in solutions takes place, making it likely that either secondary interactions between hydrated clusters have to be additionally taken into account, or that direct imidazole-imidazole interactions exist, perhaps in hydrogen-bonded chain and stack structures as those recently found in molecular dynamics simulations by Liem et al.^[202]

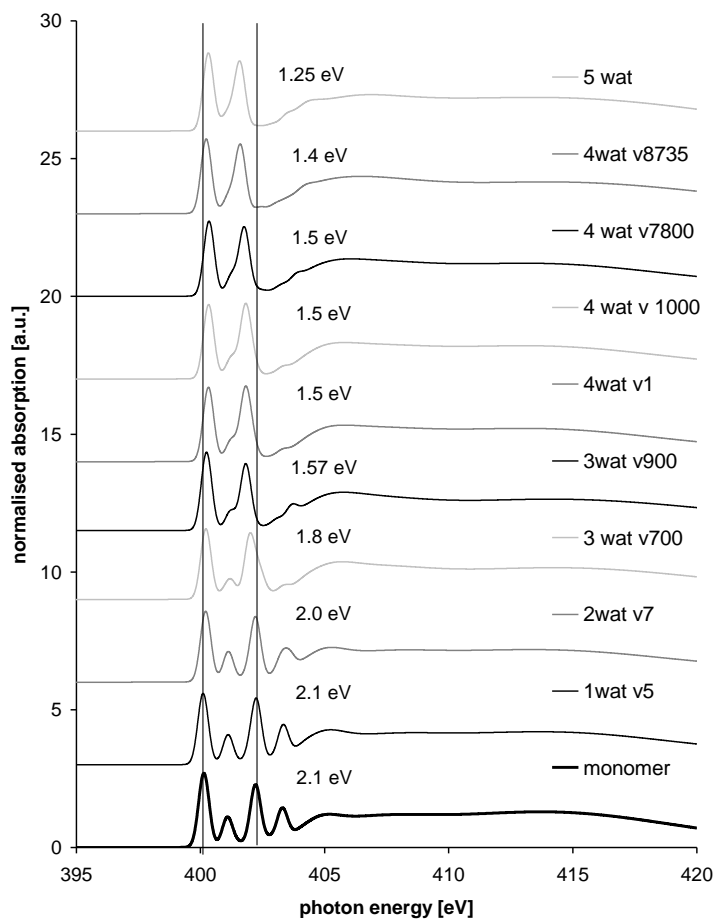


Figure 51 Summary stacked plot showing all calculated N K-edge NEXAFS spectrum of the geometry-optimised gas phase imidazole/water clusters of Jagoda-Cwiklik et al.^[145]

In any case, the poor agreement between experimental data and spectral predictions based on microsolvated cluster results confirms the conclusion drawn by Jagoda-Cwiklik et al.^[145] That more realistic models of hydration may be necessary to recover experimental behaviour in models. More complex models are needed especially to account for long-range polarisation effects in the solvent. Ultimately, models bringing together imidazole-water as well as imidazole-imidazole interactions in a synergistic way should be explored, and an attempt at such an analysis will be carried out in chapter 5. Currently the only known study that has attempted to explicitly include both water and imidazole atomic positions in a molecular model has been the study of Gontrani et al.^[200] Before moving on to the next chapter I wish to explore more complex models for the solvation of imidazole by water and attempt to come to conclusions about how a hydration structure model may correctly recover the electronic properties at the nitrogen absorbers.

4.3.5 From partial to full hydration: larger clusters

Additional cluster structures involving single imidazole molecules surrounded by a microhydration shell were obtained by molecular dynamics simulations by M. Shaik in the group of P.L.A. Popelier. Some microhydrated clusters similar to those of Jagoda-Cwiklik et al.^[145] were examined. An example, a cluster containing imidazole coordinated by five water molecules, is shown in Figure 52. It is comparable in complexity to the cluster presented in Figure 50, but it generates a StoBe spectrum with a N 1s \rightarrow 1 π^* energy split of 1.4 eV, which is still too low but in better agreement with experimental value of 1.7 eV.

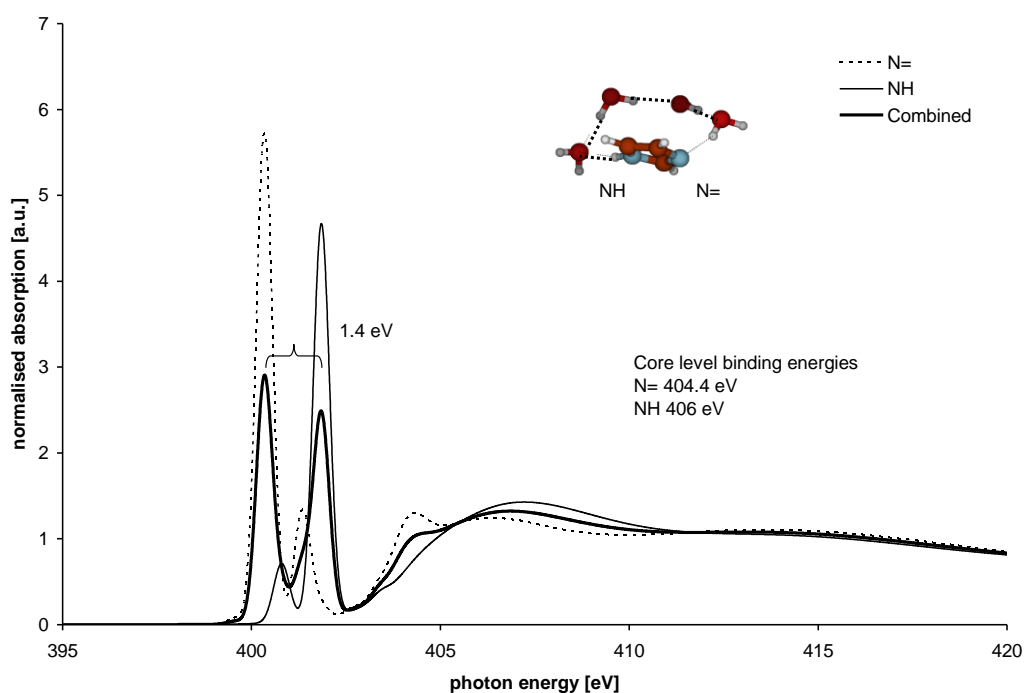


Figure 52 Calculated N K-edge NEXAFS spectrum of an imidazole·5H₂O gas phase imidazole/water cluster obtained from an MD simulation.

The remaining difference may have its origin in inaccuracies of the modelling of the valence electronic structure that provides the π^* final state. It was concluded earlier that final state effects may contribute a few tenths of an eV to energetic variations in the NEXAFS resonances. In line with this argument, despite an imperfect match of the calculated NEXAFS, the initial state N 1s core level binding energies of the two nitrogen atoms are actually 1.6 eV apart, which is in good agreement with the experimental value of 1.7 eV observed by Nolting et al.^[147] The magnitude in the disagreement to the

between experimental and calculated NEXAFS therefore appears to stem from an incorrect final state contribution.

Generally, it was found that energy-minimised microsolvated clusters did not produce sufficiently good agreement with experiment. It was therefore attempted to isolate a large cluster with complex three-dimensional solvation of an isolated imidazole molecule from a molecular dynamics simulation. A maximum cluster size was imposed by the software limit in the compiled Microsoft Windows version of StoBe that was used.

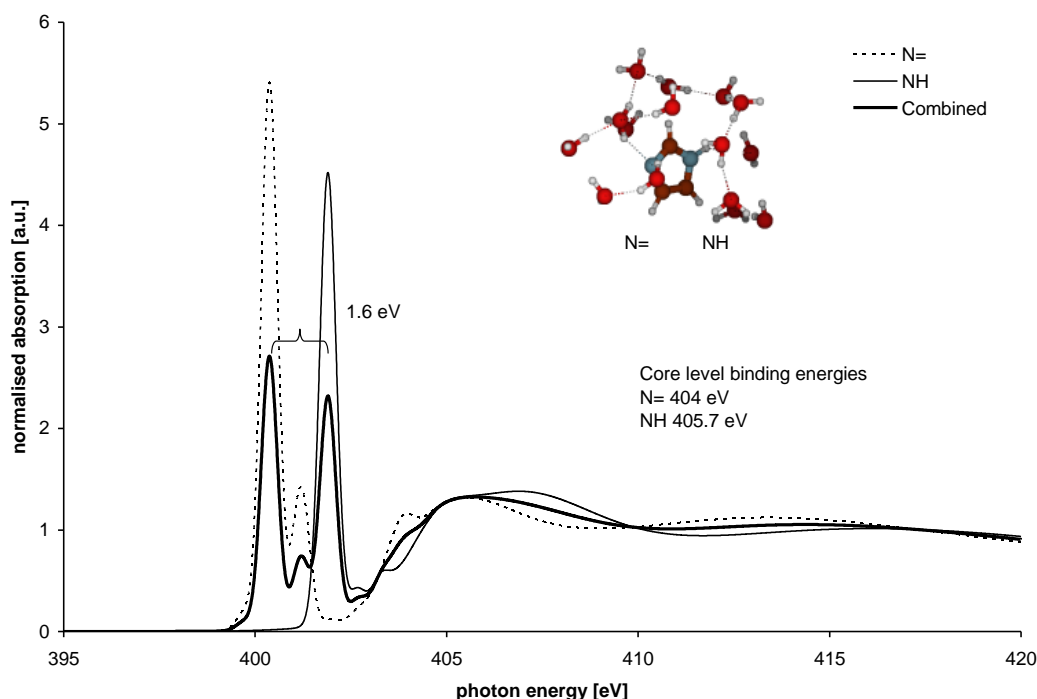


Figure 53 Calculated N K-edge NEXAFS spectrum of an imidazole·15H₂O gas phase imidazole/water cluster obtained from an MD simulation.

Finally, a cluster containing one imidazole molecule and 15 water molecules was isolated from a molecular dynamics result of Shaik. This structure and the calculated N K-edge absorption spectrum are shown in Figure 53. It can be seen that the predicted N 1s core level binding energy shift between N1 and N3 is 1.7 eV ($E_{N1} = 405.7$ eV, $E_{N3} = 404.0$ eV), in perfect agreement with the experimental value reported by Nolting et al.^[147] The observed split between the two N 1s $\rightarrow 1\pi^*$ transitions is 1.6 eV, which is also in almost perfect agreement with the value we have observed in our spectra. It appears that sufficiently large solvation clusters with one imidazole molecule at the centre are able to reproduce the experimental data very well.

4.4 Discussion

Based on the final result, it seems worthwhile to now return to the original research questions asked in section 4.3.2, before embarking on the data analysis, namely: *are we dealing with a scenario in which progressive self-association at higher concentration may involve only secondary interactions between individually hydrated imidazole molecules, which do not manifest themselves in the N K-edge spectra, thereby explaining the invariability of the NEXAFS and Raman spectra throughout the whole concentration range?*

The result that a large solvated cluster with an imidazole monomer at its centre reproduces the experimental X-ray absorption spectrum seems to lend support to the view that self-association at high concentrations does indeed take place between solvated imidazole monomers, rather than through direct hydrogen or π - π bonding between imidazole molecules. Interaction between such clusters through secondary forces may take place mediated by the network of loosely held water molecules and thereby lead to the formation of self-associated structures without further modification of the electronic structure of imidazole in the centre of the clusters.

It would be interesting to explore the properties of such clusters further to form a few hypotheses for testing. For example, it is noteworthy that our model appears to be consistent with the conclusions of Gontrani et al.^[200] who found from radial distribution functions obtained by energy-dispersive X-ray diffraction that imidazole self-association is mediated by hydrogen-bonded water molecules interleaving the imidazole molecules. It should be checked whether our model is compatible with the radial distribution functions obtained in this study.

It should be mentioned that an attempt was made to also measure rheological differences between concentrated aqueous imidazole solutions as a function of their concentration, but no measurable changes in viscosity were detectable, even close to saturation concentration. This suggests that the hydration shells around the imidazole do not lead to significant immobilisation of water molecules, again in agreement with the conclusions of Gontrani et al.^[200]

The second question asked in section 4.3.2 was: *do we have very large assemblies of self-associated clusters that are formed already at the lower end of the concentration range*

investigated here, in a quasi-phase separation process, so that any imidazole molecules added to the solution only increase the volume fraction of this phase?

The failure to detect any rheological differences and the interpretation of the spectroscopic results in terms of the formation of loosely held hydration shells around the solute molecules would suggest that strong phase separation does not take place, and that friction between the formed solvate clusters is negligible. The mobility of the solvated imidazole associates seems to be high enough to prevent an increase in viscosity, indicating that the secondary interactions holding the self-associated solution together are indeed quite weak.

However, two further observations were made in the analysis of the NEXAFS data that deserve a little more attention and should probably be pursued further in future work.

First, for several concentrations of imidazole we carried out measurements also after stopping the flow through the spectroscopic cell, on a stagnant solution. These results will be presented in chapter 6. At lower concentrations ($< 0.5 \text{ mol L}^{-1}$) it was found that the experimental NEXAFS obtained under flow, which resembled the data at higher concentrations, gave way to a broad unresolved N 1s $\rightarrow 1\pi^*$ spectrum with no discernible individual peaks, perhaps suggesting that some sort of assembly or ordering process took place in the absence of flow. This result should not be over-interpreted, as it may be induced by radiation damage or the formation of deposits on the Al_3N_4 windows of the flow cell under stagnant conditions, but it may be worth pursuing further whether it is reproducible.

Second, closer inspection of the spectra in Figure 36 reveals the appearance of a weak peak in the energy region around 399 eV in the spectra of the most concentrated solutions. The origin of this spectral feature is currently not clear, but its position would suggest it stems from a nitrogen species with a low N 1s binding energy, possibly structures with more direct imidazole-imidazole interactions. It is interesting to note in this context that its appearance at about 4 mol L^{-1} concentration coincides with the point where less than 15 water molecules are available per imidazole molecule in the solution. The increasing scarcity of hydrating water may facilitate additional interactions not currently captured by our structure model.

4.5 Conclusions

The invariability of the NEXAFS and Raman scattering results across the whole range of concentrations from 0.5 mol L^{-1} to saturation indicates that the local environment around imidazole molecules does not change as the imidazole concentration in water is increased. The 1.7 eV energy spacing between the N 1s $\rightarrow 1\pi^*$ transitions observed in the NEXAFS spectrum is identical to the previously reported N 1s binding energy shift between the nitrogen atoms in uncharged imidazole molecules in aqueous solution. This indicates that core level chemical shifts are the main factor determining the energetic positions of the NEXAFS features.

The results obtained by analysis with small microsolvated clusters found that coordination of imidazole with small and incomplete hydration shells does not reliably reproduce the observed lowering of the N 1s BE difference relative to gas phase imidazole monomers, in agreement with a previous study. In fact, solvation shells with 4 and 5 water molecules overestimate the experimentally observed effect on the energy shift between the two N 1s $\rightarrow 1\pi^*$ transitions. The evaluation of hydrogen bonding between 1:1 imidazole-water clusters indicates that electron density variations induced by hydrogen bonding to the N3 centre of the heterocycle are delocalised across the ring and also affect the electronic structure of the N1 moiety. The reverse is not taking place due to localisation of interactions at the N1-H σ bond.

The calculated NEXAFS spectrum of a larger cluster of water molecules surrounding an imidazole molecule at the centre is in excellent agreement with the experimental spectrum. As discussed, this model is compatible (i) with the observed invariability of the NEXAFS data as a function of concentration, (ii) with local structure in the molecular model concentrated aqueous imidazole solutions proposed by Gontrani et al, and (iii) with the absence of any rheological changes in imidazole solution even at the highest concentrations. Self-association may take place through interactions mediated by the hydrate shell surrounding the dissolved imidazole molecules.

5. Theoretical analysis of N K-edge NEXAFS of imidazole-imidazole aggregates and their interaction with water

5.1 Introduction

The previous chapter extensively explored solvated monomeric imidazole clusters as a model for understanding the experimentally observed NEXAFS of concentrated imidazole solutions. Other alternative interaction models have also been considered and will be summarised in this section.

First, molecular dynamics simulations of concentrated solutions and liquid imidazole^[201,202] have indicated that imidazole-imidazole chain formation may take place in the imidazole liquid and in its solutions, so we explored the effect of imidazole chain formation on the N K-edge absorption spectrum.

Second, stacked imidazole structures, as a supposed structure model for solutions with low concentrations in many previous studies (see section 1.7) were examined.

Third, and finally, more complex structures involving both direct imidazole-imidazole and imidazole-water interactions was inspired by molecular dynamics simulations results for liquid imidazole and concentrated aqueous imidazole solutions.^[201,202] The results suggested that structure formation in concentrated solutions proceeds synergistically, bringing together imidazole-imidazole and imidazole-water interactions. The output from such simulations provided complex model structures the NEXAFS spectra of which were additionally evaluated with StoBe.

5.2 Methodology

Gaussian 03^[234] and StoBe^[158] calculations were performed as described in the methodology sections of previous chapters.

5.3 Results and Discussion

5.3.1 Imidazole–imidazole interactions: chains

To examine the influence of imidazole-imidazole hydrogen bonding on the NEXAFS in the absence of the π - π bonding present between layers in the crystal structure a series of hydrogen-bonded imidazole chains was generated from the crystal structure of imidazole

and fed into the StoBe code. The resulting StoBe-calculated spectra are shown in Figure 54. From bottom to top, we observe first the by now familiar spectrum of the imidazole monomer, with its 2.1 eV split between the N 1s \rightarrow $1\pi^*$ transitions from the two nitrogen centres in the heterocycle.

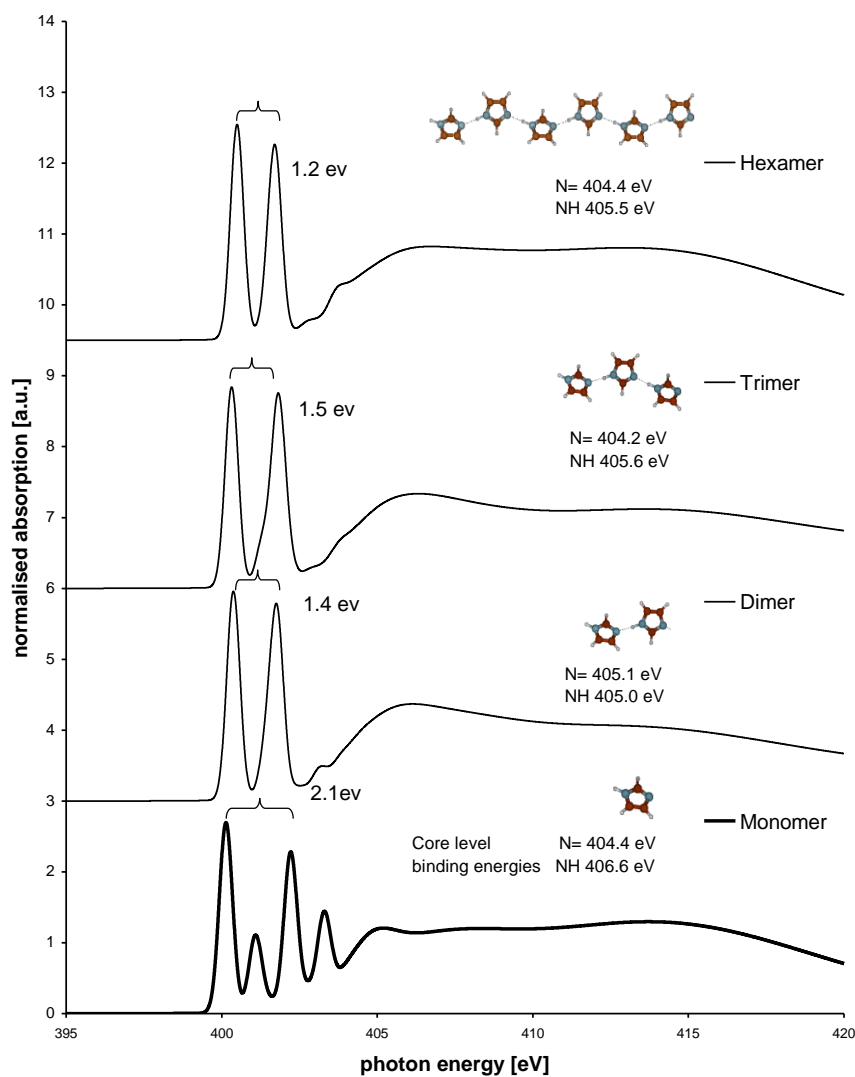


Figure 54 Calculated N K-edge absorption spectra for the monomer and hydrogen bonded chains of imidazole molecules taken out of the crystal structure of imidazole. The spectra were always calculated for the two nitrogen atoms closest to the centre of the molecule.

Dimer formation immediately reduces the split between the N 1s \rightarrow $1\pi^*$ transitions to 1.4 eV, mainly by reducing the N 1s binding energy at the N1 (NH) centre participating in the hydrogen bond. As observed previously, the electronic state of the N3 site is much less affected due to its ability to delocalise charge across the whole molecule (see section 4.3.3). In the trimer, the observed N 1s \rightarrow $1\pi^*$ transition split has a very similar value of

1.5 eV, presumably because the two N sites in the central molecule actually experience the same interactions as the two N atoms interacting in the dimer, with little electronic delocalisation across the NH bond to the additional neighbouring molecule. Extending to the hexamer appears to permit better delocalisation of charge and we find a value of 1.2 eV for the energy shift between the N $1s \rightarrow 1\pi^*$ transitions.

These results suggest that the observed difference of 1.4 eV between the N $1s \rightarrow 1\pi^*$ transitions of the N1 and N3 moieties in crystalline imidazole actually stems predominantly from the hydrogen bonding interactions, rather than from additional interactions between the imidazole chains in the crystal, which appear to influence the energy shifts between the N $1s \rightarrow 1\pi^*$ only to within a few tenths of an eV.

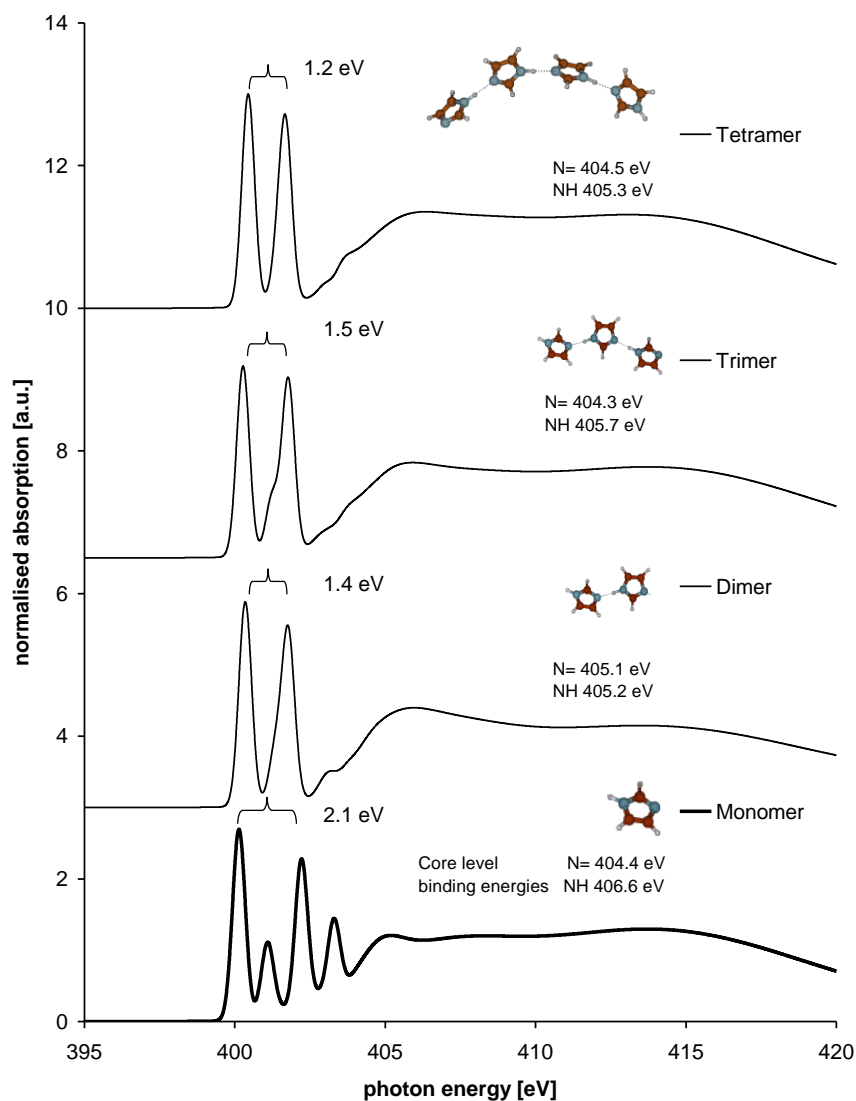


Figure 55 Calculated N K-edge absorption spectra for the monomer and hydrogen bonded chains of imidazole molecules taken from gas phase structures. The spectra were always calculated for the two nitrogen atoms closest to the centre of the molecule.

To check whether this conclusion was robust against variation in chain conformations and hydrogen bond lengths, a series of geometry-optimised gas phase structures of imidazole chains was also investigated. The structures were provided by M. Shaik from P.L.A. Popelier's research group. Molecular dynamics computational methods^[201] had been applied to obtain a set of structures that could be evaluated with StoBe. Results are presented in Figure 55. The main difference to the crystal derived chains of molecules is the formation of a bent arrangement, which minimises the total energy of the system slightly. Despite the modified geometry the spectra calculated for the dimer, trimer and tetramer gas phase molecules are almost identical to those for the crystal-derived linear chains.

5.3.2 Imidazole–imidazole interactions: trimeric stacks

Evidence for trimeric stacks of imidazole molecules has previously been reported from NMR studies of solutions in chloroform.^[198] To examine the effect of π - π stacking on the electronic structure of imidazole a geometry-optimised stack structure was generated using Gaussian 03 at the BHANDH/6-311G** level of theory, in collaboration with B. Sattelle. The stack is visualised in Figure 56 alongside the output of the StoBe calculation of its N K-edge spectrum. It can be seen that stacking leads to complex changes in the spectra, as follows. The core level binding energies are both within 0.5 eV of the monomer values. However, stacking significantly affects the N 1s \rightarrow 1 π^* peak split arising from excitation from N3 (N=) and N1 (NH), from 2.1 eV for the monomer to 1.2 eV for the stacked model. The NEXAFS spectrum also shows several shoulders and peaks for both the N3 (N=) and N1 (NH) contributions. The N3 (N=) contribution has a main peak at 400.3 eV and a small shoulder contribution at 401.0 eV, as well as a very small peak at 402.4 eV. The N1 (NH) main resonance is at 401.5 eV, with a significant shoulder not previously seen in any calculation at 400.9 eV and a small peak at 402.7 eV. Comparing to the monomer nitrogen peaks, as observed previously, the N3 (N=) contribution in the stack remains at approximately constant energy, whereas the NH contribution has shifted from 401.5 eV to 402.3 eV, by 0.8 eV. Clearly, the interactions involved in forming these stacks perturb the electronic structure of the central molecule significantly, presumably through the π - π interactions of the aromatic systems. The resulting absorption spectrum does not match well with experimental data in the concentration range above 0.5 mol L⁻¹, suggesting that such purely imidazole-imidazole bound structures are unlikely to be present in the system.

5.3.3 Combined imidazole-imidazole and imidazole-water interactions: microhydrated trimeric stacks

It seems clear that to be realistic models of self-association any trimeric stack model also needs to include the influence of solvent molecules. A more complex geometry-optimised structure model was therefore set up in Gaussian 03 as described in the previous section, involving additionally three water molecules coordinating the central imidazole molecule. The resulting structure and its predicted absorption spectrum are shown in Figure 57. It can be seen that the geometry-optimised cluster exhibits hydrogen bonding interactions of one of the water molecules linking two of the imidazole species. The observed interactions are similar to those predicted by Peral and Gallego^[199] for dilute aqueous imidazole solutions. The energy difference between the N 1s \rightarrow 1 π^* resonances in the spectra is 1.5 eV, significantly better in agreement with experiment than the value found for the non-hydrated trimer stack (Figure 56).

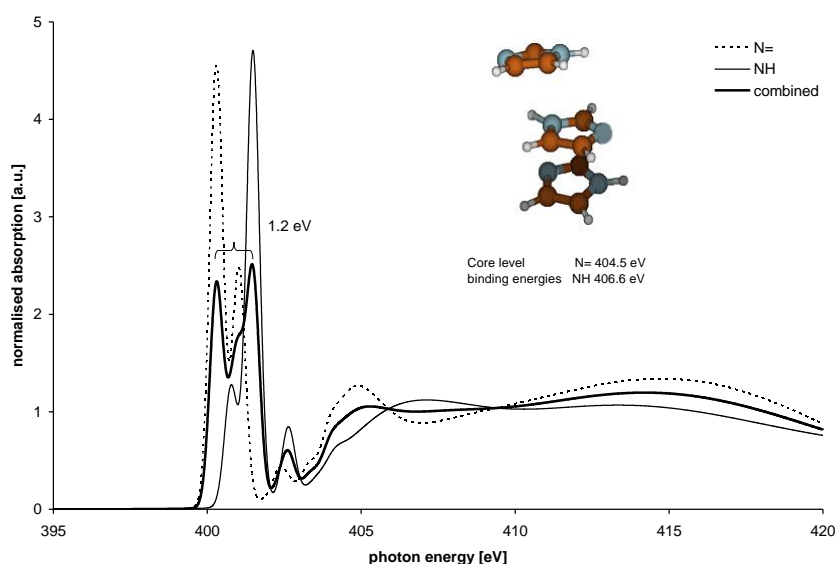


Figure 56 Calculated N K-edge absorption spectrum for the central molecule in a Gaussian 03 optimised stack of 3 imidazole molecules.

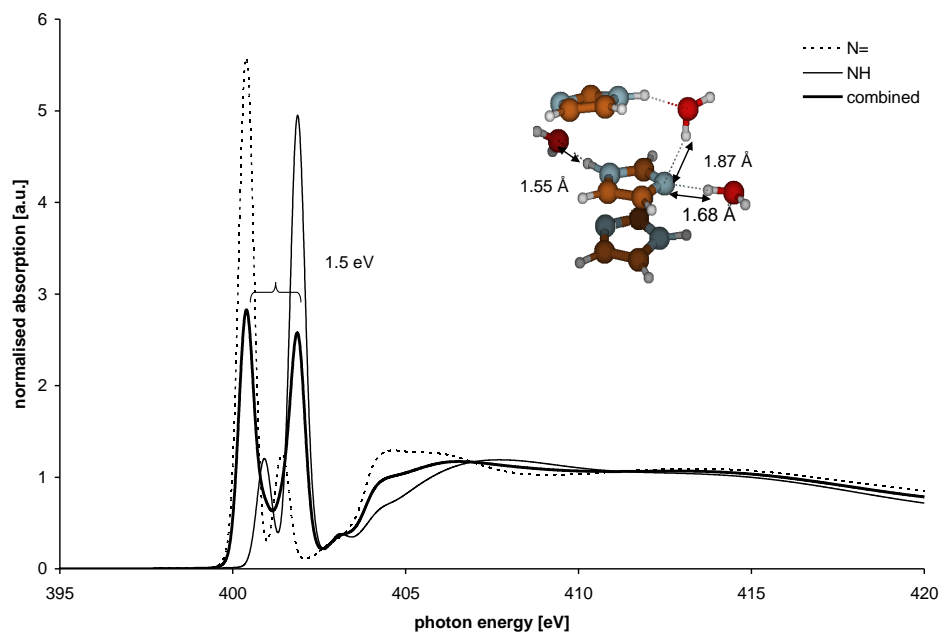


Figure 57 Calculated N K-edge absorption spectrum for the central molecule in a microhydrated Gaussian 03 optimised stack of 3 imidazole molecules.

As shown in Figure 58 an attempt was also made at examining the influence of the imidazole-water distances in this hydrated stack. In line with the results found for the water-imidazole dimer bond length variations in section 4.3.3, it was found that shortening of the imidazole-water distances further decreased the energy split between the $N\ 1s \rightarrow 1\pi^*$ absorption bands.

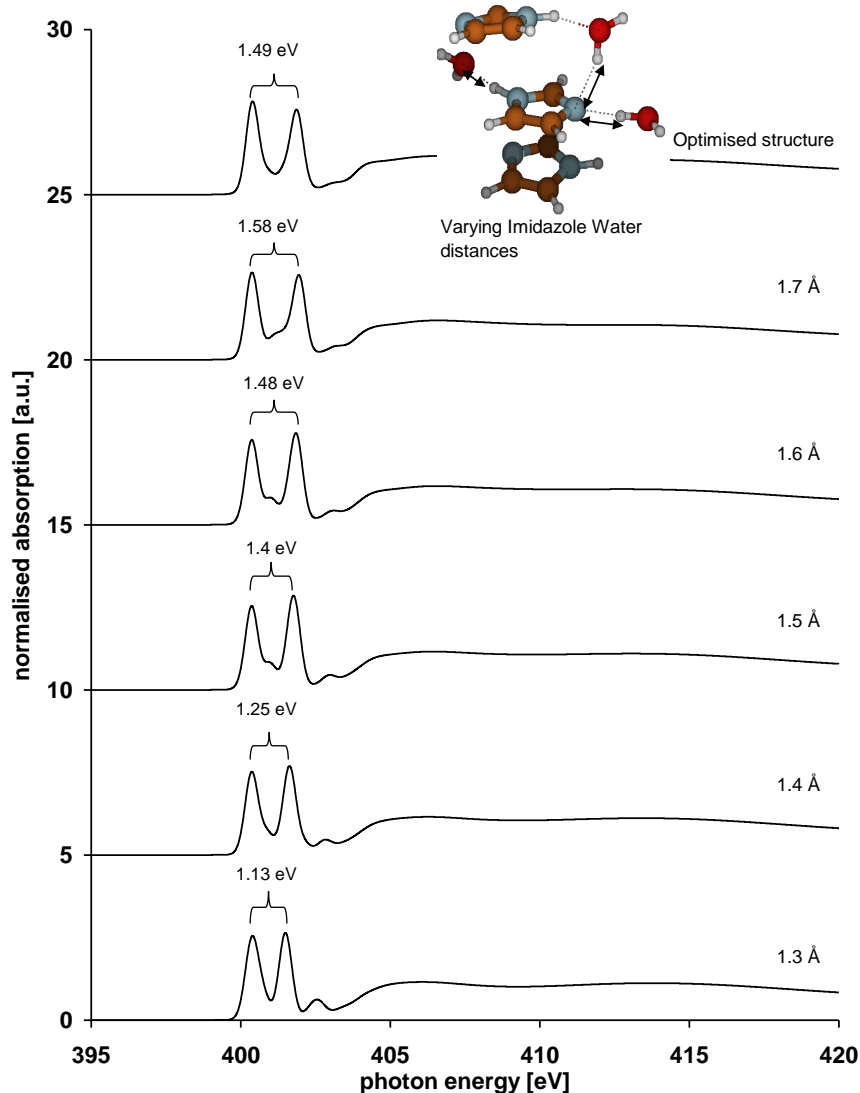


Figure 58 Calculated N K-edge spectra for water-coordinated trimer stacks under variation of the imidazole-water distances in the Gaussian 03-derived imidazole stack

5.3.4 Optimised molecular dynamics imidazole trimer and 8 waters

The most complex model involving both imidazole-imidazole and imidazole-water interactions was taken as a 3imidazole 8H₂O cluster from the outputs of molecular dynamics runs on the self-assembly process in concentrated aqueous imidazole solutions.^[202] The optimisation process involved 300 MD steps starting from an initially geometry-optimised imidazole trimer. The process of optimisation was followed by StoBe-calculated N K-edge absorption spectra of the central imidazole molecule by

evaluating the initial trimer structure and then the structures present after 4 additional intervals, 75, 150, 225 and 300 steps. The results are shown in Figure 59 to Figure 63.

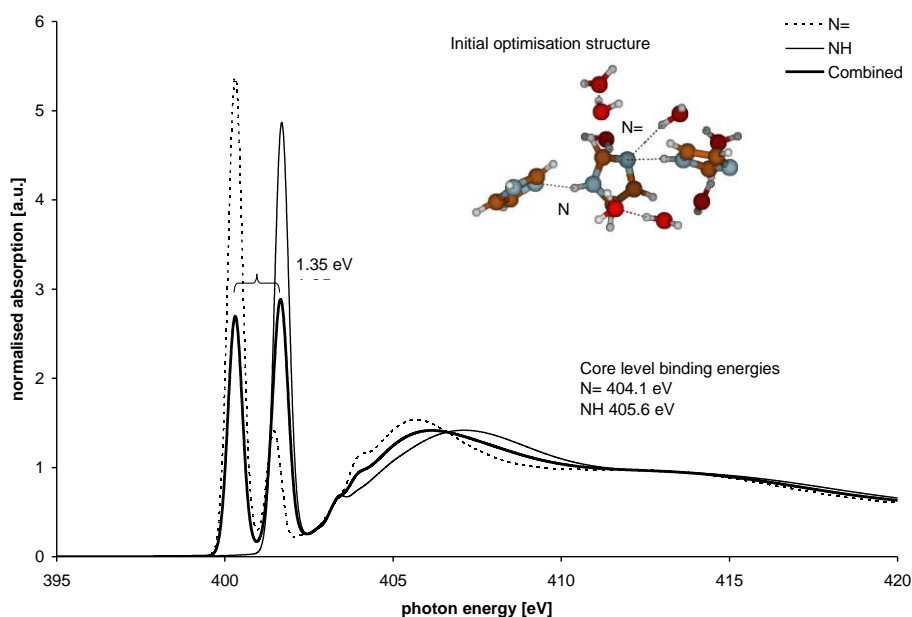


Figure 59 Calculated N K-edge absorption spectrum for the central molecule in a microhydrated cluster of 3 imidazole molecules and 8 water molecules. Shown are the structure and the associated spectrum before optimisation by molecular dynamics.

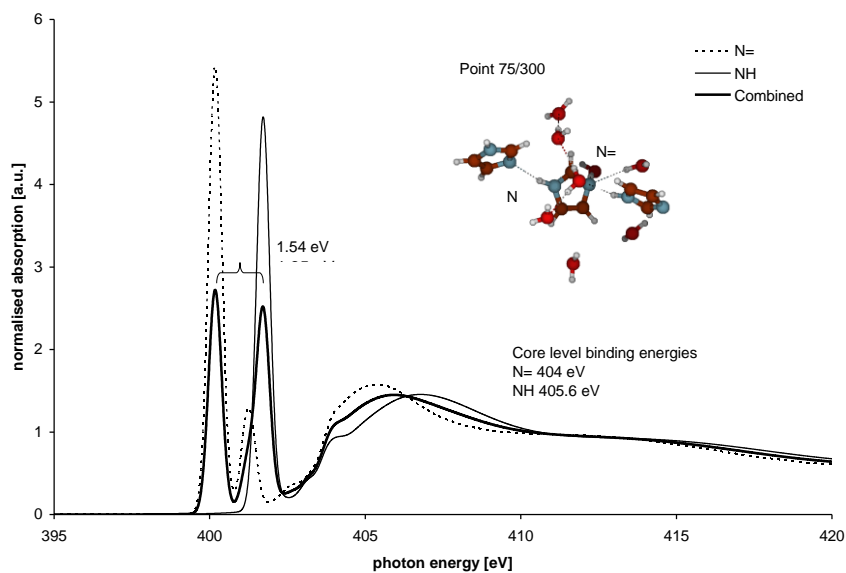


Figure 60 Calculated N K-edge absorption spectrum for the central molecule in a microhydrated cluster of 3 imidazole molecules and 8 water molecules. Shown are the structure and the associated spectrum after 75 molecular dynamics optimisation steps.

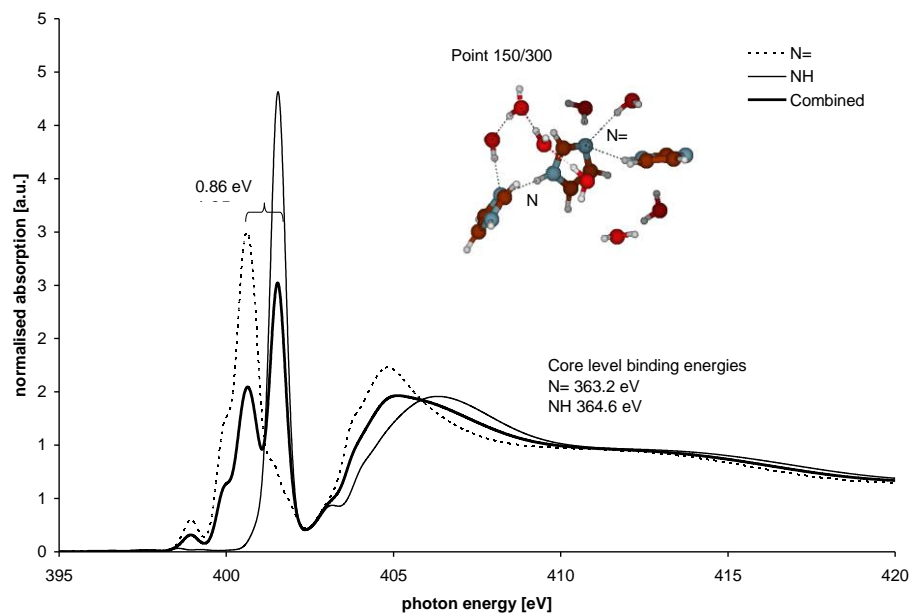


Figure 61 Calculated N K-edge absorption spectrum for the central molecule in a microhydrated cluster of 3 imidazole molecules and 8 water molecules. Shown are the structure and the associated spectrum after 150 molecular dynamics optimisation steps.

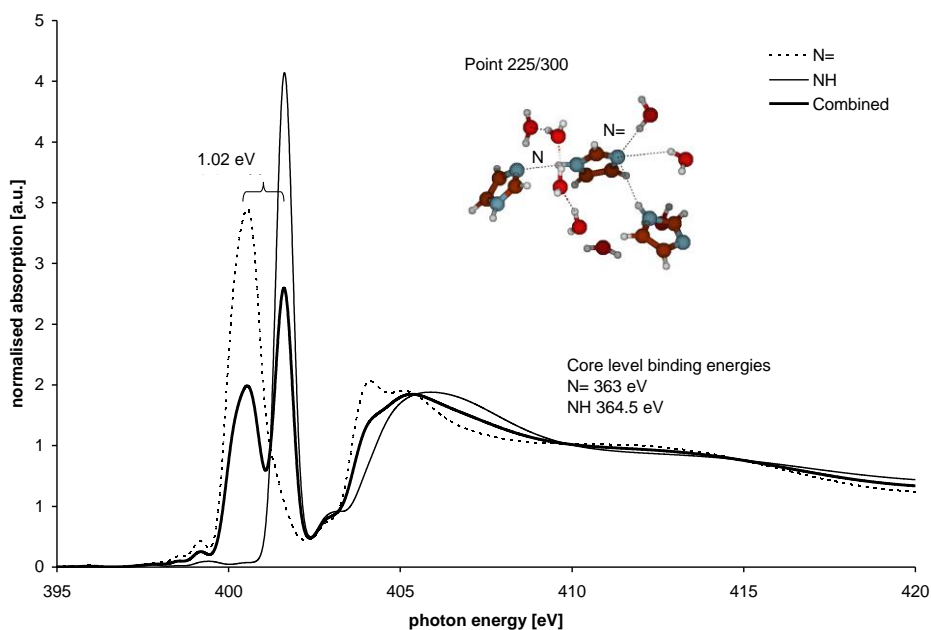


Figure 62 Calculated N K-edge absorption spectrum for the central molecule in a microhydrated cluster of 3 imidazole molecules and 8 water molecules. Shown are the structure and the associated spectrum after 225 molecular dynamics optimisation steps.

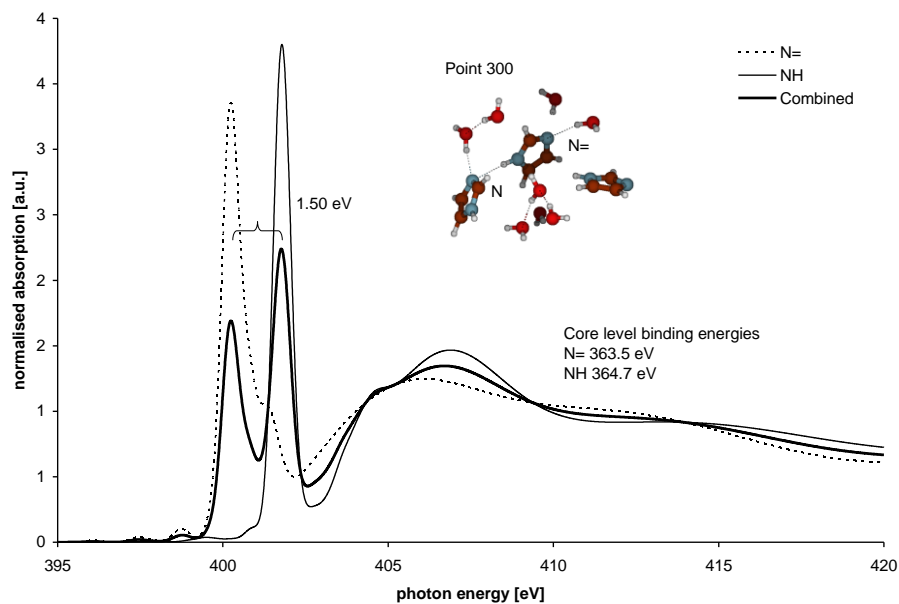


Figure 63 Calculated N K-edge absorption spectrum for the central molecule in a microhydrated cluster of 3 imidazole molecules and 8 water molecules. Shown are the structure and the associated spectrum after 300 molecular dynamics optimisation steps.

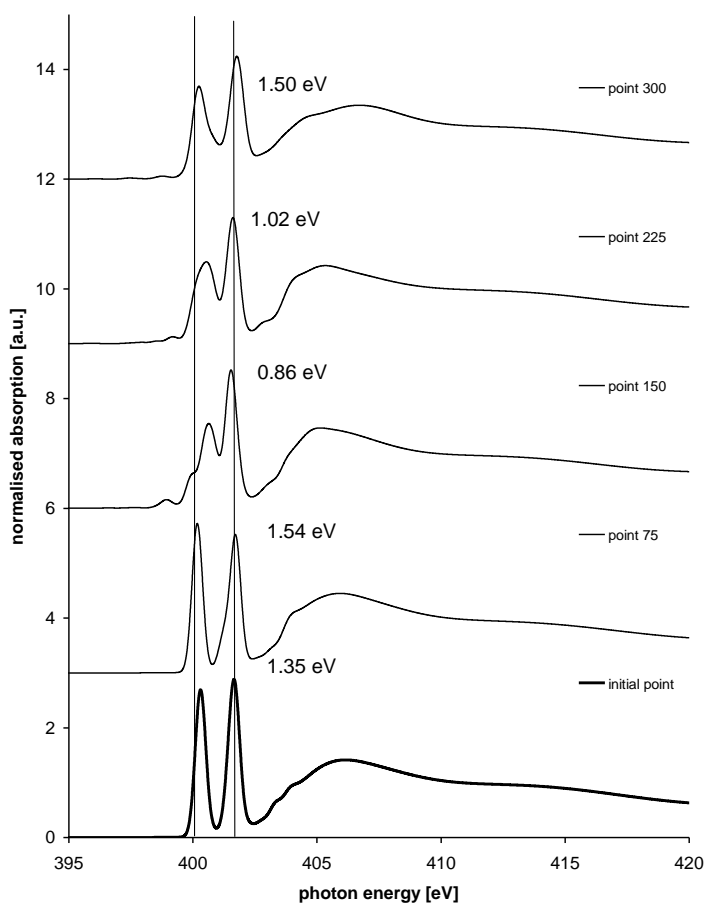


Figure 64 Summary plot of all calculated spectra during MD optimisation of the imidazole trimer·8H₂O structure

Figure 64 summarises the spectra that were obtained throughout the simulation. It can be seen that the hydrated trimer exhibits N $1s \rightarrow 1\pi^*$ energy splittings of approximately 1.35 to 1.50 eV. These values are substantially lower than the observed experimental value of 1.7 eV (Figure 36), indicating that the model is either not representative of the structure examined by experiment, or the complexity, especially the number of water molecules included in the StoBe calculation of the absorption spectrum, is insufficient to model the experimental results. In any case, however, the data show that the absorption spectrum is sensitive to the conformational changes involved in the molecular dynamics optimisation process.

5.4 Conclusions

Various additional models with increasing complexity for imidazole-imidazole and imidazole-water interactions have been examined. It is seen that the energetic difference between the N $1s \rightarrow 1\pi^*$ transitions in crystalline imidazole actually stem predominantly from the hydrogen bonding interactions, rather than from additional interactions between the imidazole chains in the crystal, such as π - π interactions. The influence of these secondary interactions is estimated to contribute at most a few tenths of an eV to the energetic position. Trimeric π - π -bonded stacks of imidazole do not lead to spectra in agreement with experimental data, though the addition of a small hydrate shell improves the result significantly. The N K-edge spectra of trimeric imidazole chains surrounded by 8 water molecules were calculated at various steps during a molecular dynamics optimisation of the structure. It was found that the absorptions spectra of the central imidazole in these structures are quite sensitive to conformational detail in the evaluated cluster, yielding reasonable but not quite satisfactory agreement with experimental data. It is concluded that more complex structure models, including more water molecules, need to be evaluated before firm conclusions about the applicability of the complex system modelling can be drawn.

6. Aqueous imidazole solutions at low concentrations (< 1M): Comparative N K-edge NEXAFS measurements in water and in chloroform

6.1 Introduction

The investigations of concentrated ($> 0.5 \text{ mol L}^{-1}$) aqueous imidazole solutions in chapter 4 concluded that they consist of hydrated imidazole monomers that significantly interact with each other through hydrogen bonding of the water molecules in their hydration shells. As already summarised in section 1.7.2, the self-association of imidazole solutions at lower concentrations in any solvent is well documented. However, the structure model developed in chapter 4 is significantly at odds with previously derived structure models for dilute solutions, which tend to conclude that imidazole forms stacked self-associated trimer structures at low concentrations. Solvents that have been investigated extensively are water,^[199] chloroform,^[196,198] carbon tetrachloride^[190,197] and benzene.^[197] Clear evidence was found already in early IR studies of chloroform^[196] and carbon tetrachloride^[190] solutions. It was concluded that chains of hydrogen-bonded imidazole oligomers were present in these solutions. Later IR studies of benzene and carbon tetrachloride revealed a high degree of self-association through hydrogen-bonding down to concentrations of $2 \times 10^{-3} \text{ mol L}^{-1}$. ^1H NMR as a function of temperature established that imidazole forms trimers in chloroform solutions.^[198] The UV-vis study of dilute aqueous imidazole solutions by Peral and Gallego,^[199] which clearly indicated substantial self-association in hydrogen-bonded stacked structures even at concentrations as low as the $10^{-4} \text{ mol L}^{-1}$ range, has been mentioned several times throughout this work, as it is particularly relevant for the interpretation of the NEXAFS of concentrated solutions described in chapters 4 and 5. It has been summarised in detail in section 1.7.2.

The aim of the NEXAFS experiments on dilute solutions was to establish whether evidence could also be obtained about the nature of self-associates at lower concentrations than 0.5 mol L^{-1} . In particular, it was similar to those observed at higher concentrations. As previous studies had suggested that the nature of imidazole associates in water was similar to those found in chloroform, the NEXAFS characterisation of the related system imidazole in chloroform was performed as well. In addition, 1N-methyl imidazole, which cannot form hydrogen bonds, was characterised in chloroform to

determine whether NEXAFS was sensitive to the expected difference in solvation structure between the two solutes.

6.2 Methodology

Dilute imidazole solutions in water and in chloroform, as well as N-methyl imidazole solutions in chloroform, were prepared without adding any additives or, in the case of water, adjustments of pH as described in section 2.1. The pH of the aqueous solutions was already reported and discussed in section 2.2.3. As expected, the pH of the dilute aqueous solutions was found to be in the range around 10 where the speciation is expected to be nearly 100% neutral imidazole species.

NEXAFS measurements were carried out at BESSY-II as described in section 2.5, using the flow cell shown in Figure 25.

6.3 Results and Discussion

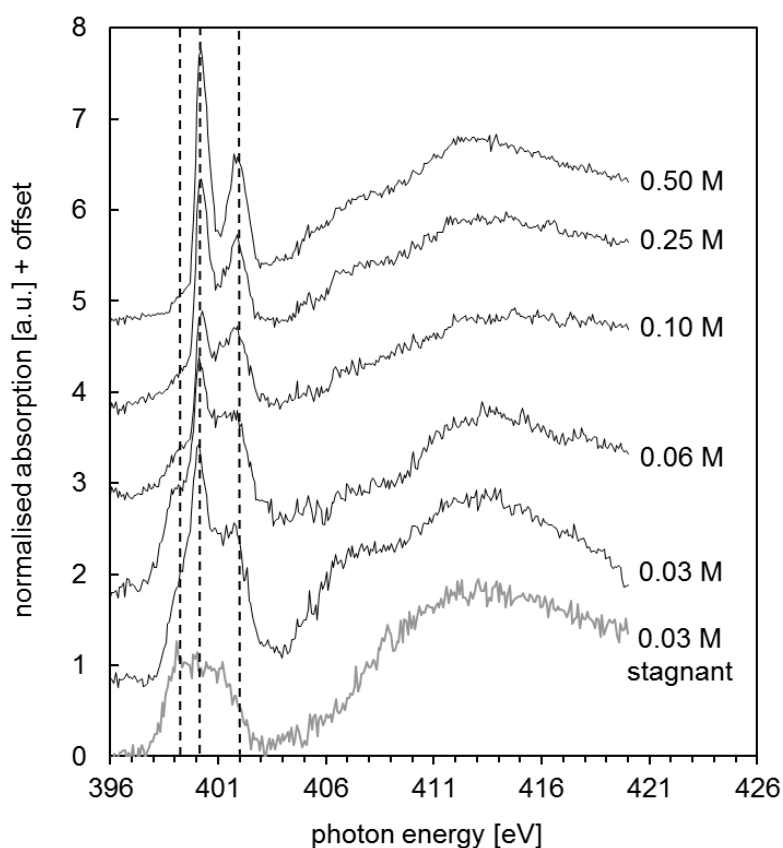


Figure 65 N K-edge near edge X-ray absorption fine structure (NEXAFS) spectra of flowing aqueous imidazole solutions as a function of concentration from 0.03 mol L^{-1} to 0.5 mol L^{-1} . Also included is a spectrum of a 0.03 mol L^{-1} stagnant solution.

6.3.1 N K-edge NEXAFS of dilute aqueous imidazole solutions

The N K-edge NEXAFS data of dilute aqueous imidazole solutions from Starting from 0.03 mol L⁻¹ to 0.5 mol L⁻¹ are presented in Figure 65. Starting our discussion of the data from the spectrum of the quite concentrated 0.5 mol L⁻¹ solution at the top of the figure, we observe the two already familiar N 1s → 1π* peaks from the N1 and N3 sites of what we previously suggested is a hydrated imidazole monomer. The vertical dashed lines indicate the energetic positions of both N 1s → 1π* transitions, which are located at photon energies of 400.2 eV and 402.0 eV.

As the concentration of imidazole is lowered, additionally a shoulder at 399.2 eV becomes increasingly apparent, and significant X-ray absorption takes place in the energy region between the two N 1s → 1π* transitions of the hydrated monomer. This clearly indicates the appearance of a different imidazole species in solutions of lower concentrations.

Interestingly, we observed during NEXAFS experiments on the most dilute solutions that the spectrum significantly changed when the flow was switched off and stagnant solutions were investigated. No significant effect was detectable at higher concentrations, and the reader may want to compare the data in Figure 66 to those in Figure 36. One such spectrum of a stagnant 0.03 mol L⁻¹ solution, obtained under otherwise identical conditions in the same flow cell, is shown in grey at the bottom of the figure. It can be seen that the two peaks arising from the N 1s → 1π* transitions of the hydrated monomer have vanished, and it appears that the spectrum obtained under these conditions is that of the imidazole species responsible for the shoulder in the flow data at low concentrations. It is evident that the broad band in the N 1s → 1π* region of this spectrum arises from at least two slightly shifted or strongly broadened transitions, possibly more, that are not resolved. It is currently not clear from what species this spectrum arises – more experimental work would be needed to elucidate its origin. The following hypothetical possibilities for its interpretation have been identified:

- It is the spectrum of aggregates different from the hydrated monomers seen at higher concentrations, possibly the stacked structures identified in previous studies. Assuming that the broad band arises from two broadened peaks, one estimates an N 1s → 1π* N1/N3 energy split of approximately 1.5 eV, which may be in line with the values found for the hydrated stacked structures in section 5.3.

- Soft X-ray radiation damage leads to the accumulation of decomposition products in the stagnant solution, giving the observed spectrum. This possibility would have to be investigated with further NEXAFS measurements.
- Deposition of solid, possibly amorphous, imidazole on the Si_3N_4 window of the flow cell takes place in the absence of a flow field. This possibility seems unlikely, given the low concentration of imidazole in the solution, which is several orders of magnitude away from the saturation concentration. Moreover, we have observed the appearance of similar low-energy shoulders in windowless experiments on stagnant imidazole/water solutions (see Figure 69 in Appendix I).

In any case, the spectra in Figure 65 indicate that at low concentration two types of associates or imidazole species may coexist. Clearly, more studies are needed to elucidate all these possibilities in more detail. However, some additional pointers for the interpretation arise from an examination of the NEXAFS acquired for chloroform solutions of imidazole and N-methyl imidazole.

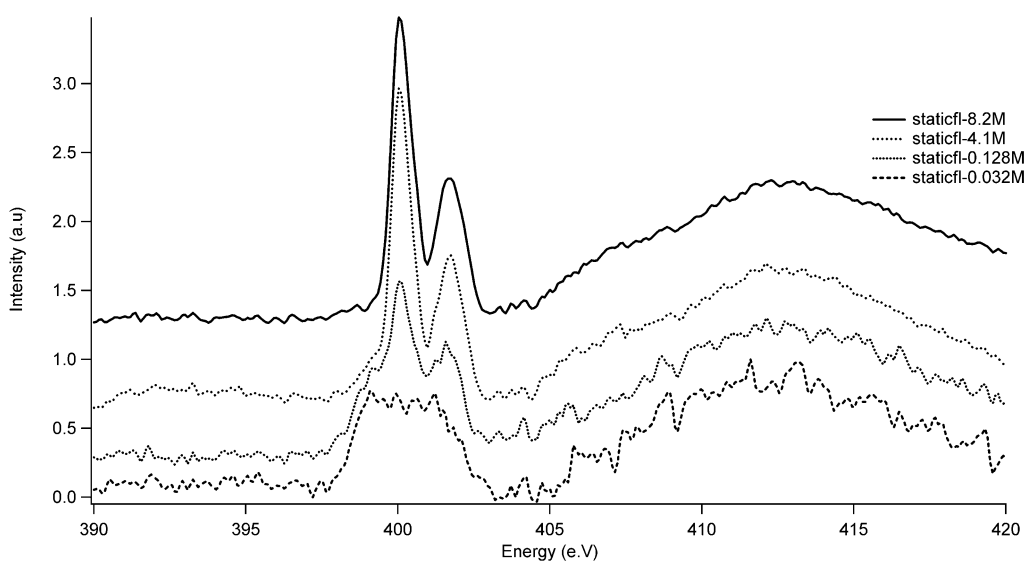


Figure 66 N K-edge near edge X-ray absorption fine structure (NEXAFS) spectra of four stagnant aqueous imidazole solutions, measured in the flow cell as a function of concentration from 0.03 mol L^{-1} to 8.2 mol L^{-1} .

6.3.2 Self-association in the absence of imidazole-solvent hydrogen bonds: NEXAFS of imidazole in chloroform

As reported above, there is strong evidence that imidazole assumes an imidazole-imidazole hydrogen-bonded trimer associate structure in chloroform solutions. To obtain a spectrum of such trimeric species we measured N K-edge NEXAFS spectra of imidazole in chloroform for three concentrations: 0.5 mol L⁻¹, 1.0 mol L⁻¹, and 2.0 mol L⁻¹. The data are shown in Figure 67. The noise quality of the spectra is not as good as that obtained for aqueous solutions because chloroform has a high absorption coefficient in the soft X-ray energy region because of its high chlorine content. It is therefore optically dense and does not permit as deep penetration of the X-rays into the sample as water, thereby limiting the signal that can be obtained from the solute molecules. It can be seen that the N 1s → 1π* region of the spectra is very similar to that observed for 0.03 – 0.10 mol L⁻¹ aqueous solutions: there is a low energy shoulder, followed by a sharp peak and a broader, less intense peak at higher energy. The energy spacing between the three features matches well with that reported for the aqueous solutions.

Assuming that these spectra indeed represent the trimer structures previously postulated for chloroform solutions this finding would indicate that the imidazole also assumes such trimer associates in dilute aqueous solution.

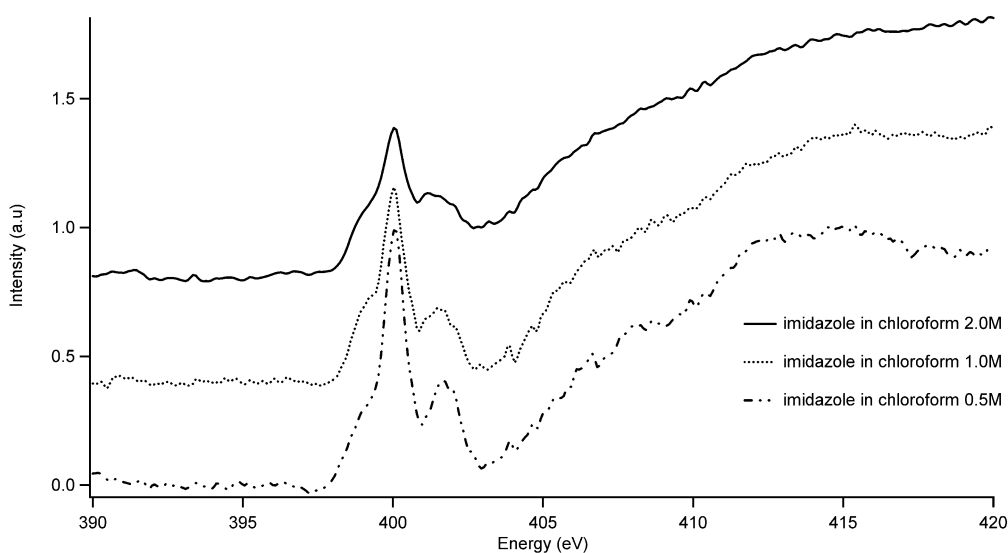


Figure 67 N K-edge near edge X-ray absorption fine structure (NEXAFS) spectra of flowing imidazole solutions in chloroform as a function of concentration, from 0.5 mol L⁻¹ to 2.0 mol L⁻¹.

6.3.3 Self-association in the absence of any hydrogen bonding: NEXAFS measurements of N-methyl imidazole dissolved in chloroform

Interestingly, similar, though not identical, spectra are observed also for N-methyl imidazole in chloroform, as shown in Figure 68. As for the spectra of imidazole in chloroform the quality of the spectra is affected by the short detection length in the X-ray-optically dense chlorinated solvent. Because the N1 site of N-methylimidazole is blocked from participating in hydrogen bonding, any self-association in this system must rely entirely on interactions between the π systems of the aromatic rings, as neither chloroform nor the solute provide sites for hydrogen bonding interactions. A more detailed analysis of the spectra in Figure 68 should be undertaken to elucidate this point. However, the obtained data indicate that imidazole-imidazole hydrogen bonding does not play a dominant role in the formation of self-associated structures.

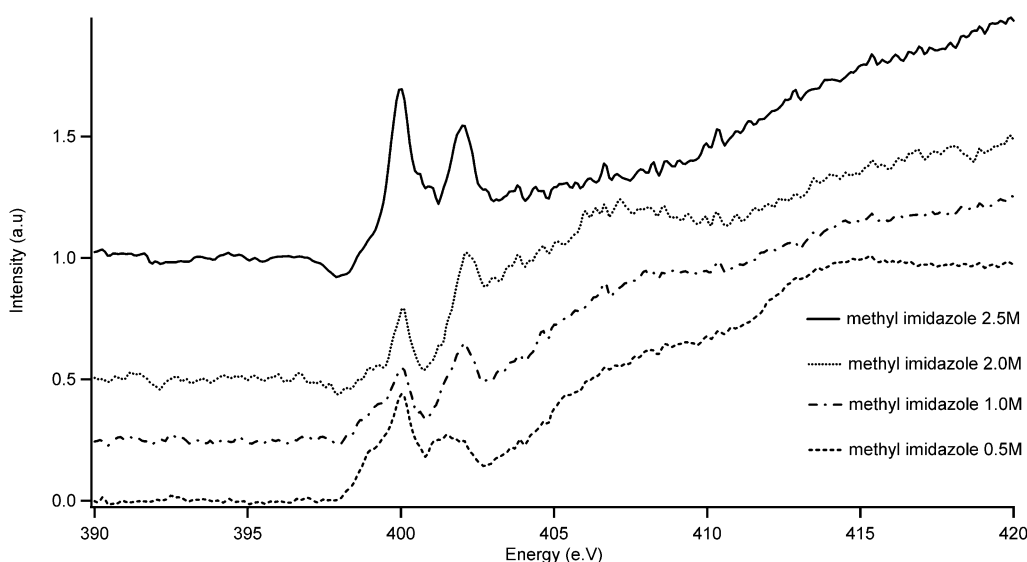


Figure 68 N K-edge near edge X-ray absorption fine structure (NEXAFS) spectra of flowing N-methylimidazole solutions in chloroform as a function of concentration, from 0.5 mol L^{-1} to 2.5 mol L^{-1} .

6.4 Conclusions

N K-edge NEXAFS investigations of lower concentrations of aqueous imidazole solutions indicate that a second, probably self-associated, imidazole species exists at lower concentrations, which is different from the hydrated monomer species seen at higher concentrations. The driving force for the formation of the latter may be the increasing scarcity of available water molecules at higher concentrations, which may help to overcome the entropic penalty associated with ordering of the solvent.

The similarity of the spectra of the known trimer species in chloroform and the imidazole species in dilute aqueous solutions suggests that such trimers may also be formed in water, in line with the suggestion of Peral and Gallego. No computational analysis of the obtained spectra has been carried out yet, though it is noted that the spectra may be compatible with the outputs obtained from the hydrated stacked structures in chapter 5.

Experiments with stagnant dilute solutions yield different data from those observed under flow, suggesting that structural changes may be induced by flow, though the possibilities of radiation damage or unwanted phase separation effects need to be investigated further.

7. Conclusions & Future Work

The work on imidazole solutions reported in this dissertation has sought to further develop the use of soft X-ray core level spectroscopy for the characterisation of local solutions structure by systematic measurements as a function of concentration. One important novel feature of this work is the successful application of more complex structure models for interpreting the N K-edge spectra of the imidazole system by *ab initio* simulation using StoBe.

The work built on previous work on aqueous imidazole with XPS, energy dispersive XRD and UV-vis. A structure model of interacting hydrated imidazole monomers that self-associate via their hydration shells has been proposed. The application of NEXAFS for the development of this model benefitted significantly from the information already available in the mentioned complementary studies. Comparative measurements with other solvents were useful for forming hypotheses about the structural nature of dilute aqueous solutions. It is perhaps too early to come to a final and definite conclusion about the veracity of the proposed structure model at high concentrations, but it can now be used as a starting point for forming hypotheses that will permit the development of understanding imidazole systems even further.

It has been shown that complex structure models in conjunction with NEXAFS allow to obtain deeper structural information about molecular solutes in solution system than previously accessible. Comparative measurements with other solvents were useful for forming hypotheses about the structural nature of dilute aqueous solutions.

All these results suggest that NEXAFS is, in combination with other techniques, a promising tool for obtaining information about the local structure of molecular solutes. The work can now be extended to applications related to crystallisation, for example for studying supersaturated solutions, nucleation phenomena and early stages of crystallisation.

Besides more NEXAFS work, future work on imidazole should be based around additional analytical studies of imidazole and its derivatives, including NMR studies with more complex pulse sequences as well as ^{15}N and solid state analysis. Neutron scattering analysis is another possibility for obtaining more information about the solution structure.

ATR probe UV/Vis should be carried out on concentrated solutions over the full pH range. Rheological measurements may for some systems supply useful pointers for structure formation.

More incisive spectroscopic probing, using advanced vibrational analysis may be able to provide deeper insight into the bonding in the imidazole system. For example, it has been found for solutions of pyrazole that hydrogen bonding induces spectral complexity in the NH stretching mode.^[260] It arises from combinations and overtones associated with a Fermi resonance involving aromatic ring modes. Hydrogen bonding brings them into resonance with the NH stretching chromophore, which leads to detectable vibrational overtones in linearly hydrogen-bonded trimers.^[260]

8. References

- [1] R. J. Davey, K. Allen, N. Blagden, W. I. Cross, H. F. Lieberman, M. J. Quayle, S. Righini, L. Seton, G. J. T. Tiddy, *Crystengcomm* **2002**, 257.
- [2] R. J. Davey, S. L. M. Schroeder, J. H. ter Horst, *Angew.Chemie - Int.Ed.* **2012**, in press.
- [3] N. Blagden, R. J. Davey, *Cryst.Growth Des.* **2003**, 3, 873.
- [4] M. Volmer, *Kinetik der Phasenbildung*, Steinkopff:Leipzig, Germany, **1939**.
- [5] P. G. Debenedetti, *Nature* **2006**, 441, 168.
- [6] A. C. Pan, T. J. Rappl, D. Chandler, N. P. Balsara, *J.Phys.Chem.B* **2006**, 110, 3692.
- [7] D. W. Oxtoby, *Acc.Chem.Res.* **1998**, 31, 91.
- [8] B. Hartke, *Angew.Chemie - Int.Ed.* **2002**, 41, 1468.
- [9] R. G. Cooks, D. X. Zhang, K. J. Koch, F. C. Gozzo, M. N. Eberlin, *Anal.Chem.* **2001**, 73, 3646.
- [10] J. A. R. P. SARMA, G. R. Desiraju, *Acc.Chem.Res.* **1986**, 19, 222.
- [11] A. Spitaleri, C. A. Hunter, J. F. McCabe, M. J. Packer, S. L. Cockroft, *Crystengcomm* **2004**, 6, 489.
- [12] C. A. Hunter, C. M. R. Low, M. J. Packer, S. E. Spey, J. G. Vinter, M. O. Vysotsky, C. Zonta, *Angew.Chemie - Int.Ed.* **2001**, 40, 2678.
- [13] D. Kashchiev, G. M. van Rosmalen, *Crystal Research and Technology* **2003**, 38, 555.
- [14] D. Kashchiev, *Nucleation: Basic Theory with Applications*, Butterworth-Heinemann:Oxford, **2000**.
- [15] P. G. Vekilov, *Cryst.Growth Des.* **2010**, 10, 5007.
- [16] D. Gebauer, H. Cölfen, *Nano Today* **2011**, 6, 564.
- [17] J. Bernstein, *Polymorphism in Molecular Crystals*, Clarendon:Oxford, **2002**.
- [18] J. Bernstein, R. J. Davey, J. O. Henck, *Angew.Chemie - Int.Ed.* **1999**, 38, 3441.
- [19] P. G. Vekilov, *Cryst.Growth Des.* **2004**, 4, 671.
- [20] K. G. Soga, J. R. Melrose, R. C. Ball, *J.Chem.Phys.* **1999**, 110, 2280.
- [21] V. Talanquer, D. W. Oxtoby, *J.Chem.Phys.* **1997**, 106, 3673.
- [22] P. R. ten Wolde, D. Frenkel, *Science* **1997**, 277, 1975.
- [23] H. G. Alison, R. J. Davey, J. Garside, M. J. Quayle, G. J. T. Tiddy, D. T. Clarke, G. R. Jones, *Phys.Chem.Chem.Phys.* **2003**, 5, 4998.
- [24] P. E. Bonnett, K. J. Carpenter, S. Dawson, R. J. Davey, *J.Chem.Soc.Chem.Comm.* **2003**, 698.

- [25] R. J. Davey, G. Dent, R. K. Mughal, S. Parveen, *Cryst.Growth Des.* **2006**, *6*, 1788.
- [26] I. Weissbuch, M. Lahav, L. Leiserowitz, *Cryst.Growth Des.* **2003**, *3*, 125.
- [27] M. Gardner, A. J. Guerin, C. A. Hunter, U. Michelsen, C. Rotger, *New Journal of Chemistry* **1999**, *23*, 309.
- [28] P. Jonkheijm, P. van der Schoot, A. P. H. J. Schenning, E. W. Meijer, *Science* **2006**, *313*, 80.
- [29] A. Gavezzotti, *Chem.Eur.J.* **1999**, *5*, 567.
- [30] A. Gavezzotti, G. Filippini, J. Kroon, B. P. vanEijck, P. Klewinghaus, *Chem.Eur.J.* **1997**, *3*, 893.
- [31] S. Hamad, C. Moon, C. R. A. Catlow, A. T. Hulme, S. L. Price, *J.Phys.Chem.B* **2006**, *110*, 3323.
- [32] C. Desgranges, J. Delhommelle, *J.Am.Chem.Soc.* **2006**, *128*, 15104.
- [33] P. G. Bolhuis, C. Dellago, D. Chandler, *Faraday Discuss.Chem.Soc.* **1998**, *110*, 421.
- [34] C. Dellago, P. G. Bolhuis, F. S. Csajka, D. Chandler, *J.Chem.Phys.* **1998**, *108*, 1964.
- [35] *X-ray Absorption. Principles, Applications, Techniques of EXAFS, SEXAFS and XANES (Chemical Analysis, Vol. 92)*, (Eds.: D. C. Koningsberger, R. Prins) Wiley:New York, **1988**.
- [36] G. Bunker, *Introduction to XAFS: A Practical Guide to X-ray Absorption Fine Structure Spectroscopy*, Cambridge University Press:Cambridge, **2010**.
- [37] B. K. Teo, *EXAFS: Basic Principles and Data Analysis*, Springer Verlag:Berlin, Heidelberg, New York, Tokyo, **1986**.
- [38] J. Stöhr, *NEXAFS Spectroscopy (Springer Series in Surface Sciences 25)*, Springer:Berlin, Heidelberg, **1992**.
- [39] R. Stumm von Bordwehr, *Ann.Phys.Fr.* **1989**, *14*, 377.
- [40] S. L. M. Schroeder, *personal communication* **2012**.
- [41] W. Kossel, *Z.Physik* **1920**, *1*, 119.
- [42] H. Fricke, *Phys.Rev.* **1920**, *16*, 202.
- [43] R. d. L. Kronig, *Z.Physik* **1931**, *70*, 317.
- [44] R. d. L. Kronig, *Z.Physik* **1932**, *75*, 191.
- [45] R. d. L. Kronig, *Z.Physik* **1932**, *75*, 468.
- [46] D. R. Hartree, R. d. L. Kronig, H. Petersen, *Physica* **1934**, *1*, 895.
- [47] H. Petersen, *Z.Physik* **1933**, *80*, 258.
- [48] J. D. Hanawalt, *Phys.Rev.* **1931**, *37*, 715.
- [49] B. Cioffari, *Phys.Rev.* **1937**, *51*, 0630.

- [50] T. Drynski, R. Smoluchowski, *Physica* **1939**, 6, 929.
- [51] M. Sawada, K. Tsutsumi, T. Shiraiwa, M. Obashi, *J.Phys.Soc.Jpn.* **1955**, 10, 459.
- [52] M. Sawada, K. Tsutsumi, T. Shiraiwa, M. Obashi, *J.Phys.Soc.Jpn.* **1955**, 10, 464.
- [53] T. Shiraiwa, T. Ishimura, M. Sawada, *J.Phys.Soc.Jpn.* **1957**, 12, 788.
- [54] W. F. Nelson, I. Siegel, R. W. Wagner, *Phys.Rev.* **1962**, 127, 2025.
- [55] O. Brummer, G. Drager, *Phys.Stat.Solidi* **1968**, 27, 513.
- [56] D. E. Sayers, E. A. Stern, F. W. Lytle, *Phys.Rev.Lett.* **1971**, 27, 1204.
- [57] B. M. Kincaid, P. Eisenberger, *Phys.Rev.Lett.* **1975**, 34, 1361.
- [58] P. Eisenberger, B. M. Kincaid, *Chem.Phys.Lett.* **1975**, 36, 134.
- [59] D. R. Sandstrom, H. W. Dodgen, F. W. Lytle, *J.Chem.Phys.* **1977**, 67, 473.
- [60] E. A. Stern, D. E. Sayers, F. W. Lytle, *Phys.Rev.B* **1975**, 11, 4836.
- [61] D. R. Sandstrom, *J.Chem.Phys.* **1979**, 71, 2381.
- [62] R. A. Howe, W. S. Howells, J. E. Enderby, *J.Phys.C* **1974**, 7, L111.
- [63] M. P. Fontana, G. Maisano, P. Migliardo, F. Wanderlingh, *Solid State Commun.* **1977**, 23, 489.
- [64] M. P. Fontana, G. Maisano, P. Migliardo, F. Wanderlingh, *J.Chem.Phys.* **1978**, 69, 676.
- [65] A. K. Soper, G. W. Neilson, J. E. Enderby, R. A. Howe, *J.Phys.C* **1977**, 10, 1793.
- [66] A. Fontaine, P. Lagarde, D. Raoux, M. P. Fontana, G. Maisano, P. Migliardo, F. Wanderlingh, *Phys.Rev.Lett.* **1978**, 41, 504.
- [67] P. Lagarde, A. Fontaine, D. Raoux, A. Sadoc, P. Migliardo, *J.Chem.Phys.* **1980**, 72, 3061.
- [68] H. Petersen, C. Kunz, *Journal of Physics F-Metal Physics* **1977**, 7, 2495.
- [69] H. Petersen, C. Kunz, *Phys.Rev.Lett.* **1975**, 35, 863.
- [70] E. D. Crozier, F. W. Lytle, D. E. Sayers, E. A. Stern, *Canadian Journal of Chemistry- Revue Canadienne de Chimie* **1977**, 55, 1968.
- [71] E. D. Crozier, J. J. Rehr, R. Ingalls, in *X-ray Absorption: Principles, Applications, Techniques of EXAFS, SEXAFS and XANES*, (Eds.: D. C. Koningsberger, R. Prins), Wiley-Interscience:New York, **1988**, p. pp. 373-472.
- [72] L. Ottaviano, A. Filipponi, A. DiCicco, *Phys.Rev.B* **1994**, 49, 11749.
- [73] A. Filipponi, A. DiCicco, *Nuclear Instruments & Methods in Physics Research Section B- Beam Interactions with Materials and Atoms* **1994**, 93, 302.
- [74] T. M. Seward, C. M. B. Henderson, J. M. Charnock, B. R. Dobson, *Geochimica et Cosmochimica Acta* **1996**, 60, 2273.
- [75] D. M. Pfund, J. G. Darab, J. L. Fulton, Y. J. Ma, *J.Phys.Chem.* **1994**, 98, 13102.

- [76] E. A. Stern, P. Livins, Z. Zhang, *Phys.Rev.B* **1991**, *43*, 8850.
- [77] A. DiCicco, *Phys.Rev.B* **1996**, *53*, 6174.
- [78] A. Filipponi, S. De Panfilis, A. Di Cicco, *Phys.Stat.Sol.B* **2000**, *219*, 267.
- [79] A. Filipponi, A. Di Cicco, S. De Panfilis, *Phys.Rev.Lett.* **1999**, *83*, 560.
- [80] S. De Panfilis, A. Filipponi, *J.Appl.Phys.* **2000**, *88*, 562.
- [81] P. D'Angelo, N. V. Pavel, D. Roccatano, H. F. Nolting, *Phys.Rev.B* **1996**, *54*, 12129.
- [82] P. D'Angelo, H. F. Nolting, N. V. Pavel, *Phys.Rev.A* **1996**, *53*, 798.
- [83] A. Filipponi, P. D'Angelo, N. V. Pavel, A. DiCicco, *Chem.Phys.Lett.* **1994**, *225*, 150.
- [84] P. D'Angelo, A. D'Inola, A. Filipponi, N. V. Pavel, D. Roccatano, *J.Chem.Phys.* **1994**, *100*, 985.
- [85] J. L. Fulton, D. M. Pfund, S. L. Wallen, M. Newville, E. A. Stern, Y. J. Ma, *J.Chem.Phys.* **1996**, *105*, 2161.
- [86] S. L. Wallen, B. J. Palmer, D. M. Pfund, J. L. Fulton, M. Newville, Y. J. Ma, E. A. Stern, *J.Phys.Chem.A* **1997**, *101*, 9632.
- [87] T. M. Seward, C. M. B. Henderson, J. M. Charnock, T. Driesner, *Geochimica et Cosmochimica Acta* **1999**, *63*, 2409.
- [88] S. L. Wallen, B. J. Palmer, J. L. Fulton, *J.Chem.Phys.* **1998**, *108*, 4039.
- [89] D. T. Bowron, A. Filipponi, C. Lobban, J. L. Finney, *Chem.Phys.Lett.* **1998**, *293*, 33.
- [90] A. Filipponi, D. T. Bowron, C. Lobban, J. L. Finney, *Phys.Rev.Lett.* **1997**, *79*, 1293.
- [91] D. T. Bowron, A. Filipponi, M. A. Roberts, J. L. Finney, *Phys.Rev.Lett.* **1998**, *81*, 4164.
- [92] A. Filipponi, P. D. D' Angelo, *J.Chem.Phys.* **1998**, *109*, 5356.
- [93] A. Knop-Gericke, E. Kleimenov, M. Hävecker, R. Blume, D. Teschner, S. Zafeiratos, R. Schlögl, V. I. Bukhtiyarov, V. V. Kaichev, I. P. Prosvirin, A. I. Nizovskii, H. Bluhm, A. Barinov, P. Dudin, M. Kiskinova, *Adv.Catal.* **2009**, *52*, 213.
- [94] H. Bluhm, *J.Electron Spectrosc.Relat.Phenom.* **2011**, *177*, 71.
- [95] T. Schiros, K. J. Andersson, L. G. M. Pettersson, A. Nilsson, H. Ogasawara, *J.Electron Spectrosc.Relat.Phenom.* **2010**, *177*, 85.
- [96] S. L. M. Schroeder, G. D. Moggridge, R. M. Lambert, T. Rayment, in *Spectroscopy for Surface Science (Advances in Spectroscopy, Vol.26)*, (Eds.: R. J. H. Clark, R. E. Hester), Wiley & Sons:New York, Chichester, **1998**, p. pp. 1-70.
- [97] J. Stöhr, in *X-Ray Absorption: Principles, Applications, Techniques of EXAFS, SEXAFS and XANES*, (Eds.: D. C. Koningsberger, R. Prins), Wiley:New York, Chichester, **1988**, p. pp. 443-571.
- [98] J. Stöhr, in *Emission and Scattering Techniques*, (Ed.: P. Day), Reidel:Boston, **1981**, p. pp. 213-250.

- [99] S. L. M. Schroeder, G. D. Moggridge, E. Chabala, R. M. Ormerod, T. Rayment, R. M. Lambert, *Faraday Discuss.Chem.Soc.* **1996**, *105*, 317.
- [100] S. L. M. Schroeder, G. D. Moggridge, T. Rayment, R. M. Lambert, *J.Mol.Catal.A* **1997**, *119*, 357.
- [101] L. Tröger, D. Arvanitis, K. Baberschke, H. Michaelis, U. Grimm, E. Zschech, *Phys.Rev.B* **1992**, *46*, 3283.
- [102] F. Quinn, N. Poolton, A. Malins, E. Pantos, C. Andersen, P. Denby, V. Dhanak, G. Miller, *J.Synchrotron Rad.* **2003**, *10*, 461.
- [103] N. Peltekis, B. N. Holland, S. Krishnamurthy, I. T. McGovern, N. R. J. Poolton, S. Patel, C. McGuinness, *J.Am.Chem.Soc.* **2008**, *130*, 13008.
- [104] M. Ishii, B. Hamilton, N. Poolton, *J.Appl.Phys.* **2008**, *104*.
- [105] M. Ishii, N. Rigopoulos, N. R. J. Poolton, B. Hamilton, *X-Ray Absorption Fine Structure-XAFS13* **2007**, 882, 761.
- [106] T. H. Yoon, *Applied Spectroscopy Reviews* **2009**, *44*, 91.
- [107] J. Stöhr, F. Sette, A. L. Johnson, *Phys.Rev.Lett.* **1984**, *53*, 1684.
- [108] M. Cavalleri, M. Odelius, D. Nordlund, A. Nilsson, L. G. M. Pettersson, *Phys.Chem.Chem.Phys.* **2005**, *7*, 2854.
- [109] *StoBe-deMon version 3.1*, Hermann, K., Pettersson, L. G. M., Casida, M. E., Daul, C., Goursot, A., Koester, A., Proynov, E., St-Amant, A., Salahub, D. R., Carravetta, V., Duarte, H., Friedrich, C., Godbout, N., Guan, J., Jamorski, C., Leboeuf, M., Leetmaa, M., Nyberg, M., Patchkovskii, S., Pedocchi, L., Sim, F., Triguero, L., and Vela, A., **2011**, Stockholm, Berlin.
- [110] F. D. Vila, J. J. Rehr, H. H. Rossner, H. J. Krappe, *Phys.Rev.B* **2007**, *76*.
- [111] J. J. Rehr, J. J. Kas, M. P. Prange, A. P. Sorini, Y. Takimoto, F. Vila, *Comptes Rendus Physique* **2009**, *10*, 548.
- [112] J. J. Rehr, J. J. Kas, F. D. Vila, M. P. Prange, K. Jorissen, *Phys.Chem.Chem.Phys.* **2010**, *12*, 5503.
- [113] J. Vinson, J. J. Rehr, J. J. Kas, E. L. Shirley, *Phys.Rev.B* **2011**, *83*.
- [114] J. J. Rehr, *Radiat.Phys,Chem.* **2006**, *75*, 1547.
- [115] J. J. Rehr, A. L. Ankudinov, *Coordination Chemistry Reviews* **2005**, *249*, 131.
- [116] J. J. Rehr, R. C. Albers, *Rev.Mod.Phys.* **2000**, *72*, 621.
- [117] B. Winter, *Nucl.Instrum.Methods A* **2009**, *601*, 139.
- [118] A. Golzhauser, C. Wöll, *ChemPhysChem* **2010**, *11*, 3201.
- [119] A. Golzhauser, C. Wöll, *Phys.Chem.Chem.Phys.* **2010**, *12*, 4273.
- [120] B. Winter, M. Faubel, *Chem.Rev.* **2006**, *106*, 1176.
- [121] L. A. Naslund, J. Luning, Y. Ufuktepe, H. Ogasawara, P. Wernet, U. Bergmann, L. G. M. Pettersson, A. Nilsson, *J.Phys.Chem.B* **2005**, *109*, 13835.

- [122] M. Cavalleri, L. A. Näslund, D. C. Edwards, P. Wernet, H. Ogasawara, S. Myneni, L. Ojamae, M. Odelius, A. Nilsson, L. G. M. Pettersson, *J.Chem.Phys.* **2006**, *124*.
- [123] M. Leetmaa, M. Ljungberg, H. Ogasawara, M. Odelius, L. A. Näslund, A. Nilsson, L. G. M. Pettersson, *J.Chem.Phys.* **2006**, *125*.
- [124] D. Nordlund, M. Odelius, H. Bluhm, H. Ogasawara, L. G. M. Pettersson, A. Nilsson, *Chem.Phys.Lett.* **2008**, *460*, 86.
- [125] P. Wernet, D. Testemale, J. L. Hazemann, R. Argoud, P. Glatzel, L. G. M. Pettersson, A. Nilsson, U. Bergmann, *J.Chem.Phys.* **2005**, *123*.
- [126] T. Tokushima, Y. Harada, O. Takahashi, Y. Senba, H. Ohashi, L. G. M. Pettersson, A. Nilsson, S. Shin, *Chem.Phys.Lett.* **2008**, *460*, 387.
- [127] M. Leetmaa, K. T. Wikfeldt, M. P. Ljungberg, M. Odelius, J. Swenson, A. Nilsson, L. G. M. Pettersson, *J.Chem.Phys.* **2008**, *129*.
- [128] Ph. Wernet, D. Nordlund, U. Bergmann, M. Cavalleri, M. Odelius, H. Ogasawara, L. A. Näslund, T. K. Hirsch, L. Ojamäe, P. Glatzel, L. G. M. Pettersson, A. Nilsson, *Science* **2004**, *304*, 995.
- [129] L. A. Naslund, D. C. Edwards, P. Wernet, U. Bergmann, H. Ogasawara, L. G. M. Pettersson, S. Myneni, A. Nilsson, *J.Phys.Chem.A* **2005**, *109*, 5995.
- [130] C. Huang, K. T. Wikfeldt, T. Tokushima, D. Nordlund, Y. Harada, U. Bergmann, M. Niebuhr, T. M. Weiss, Y. Horikawa, M. Leetmaa, M. P. Ljungberg, O. Takahashi, A. Lenz, L. Ojamae, A. P. Lyubartsev, S. Shin, L. G. M. Pettersson, A. Nilsson, *Proceedings of the National Academy of Sciences of the United States of America* **2009**, *106*, 15214.
- [131] K. R. Wilson, M. Cavalleri, B. S. Rude, R. D. Schaller, T. Catalano, A. Nilsson, R. J. Saykally, L. G. M. Pettersson, *J.Phys.Chem.B* **2005**, *109*, 10194.
- [132] L. A. Naslund, D. C. Edwards, P. Wernet, U. Bergmann, H. Ogasawara, L. G. M. Pettersson, S. Myneni, A. Nilsson, *J.Phys.Chem.A* **2005**, *109*, 5995.
- [133] B. Winter, *Trac-Trends in Analytical Chemistry* **2008**, *27*, IX.
- [134] B. Winter, E. F. Aziz, U. Hergenbahn, M. Faubel, I. V. Hertel, *J.Chem.Phys.* **2007**, *126*.
- [135] K. M. Lange, K. F. Hodeck, U. Schade, E. F. Aziz, *J.Phys.Chem.B* **2010**, *114*, 16997.
- [136] B. Winter, M. Faubel, R. Vacha, P. Jungwirth, *Chem.Phys.Lett.* **2009**, *474*, 241.
- [137] M. A. Brown, B. Winter, M. Faubel, J. C. Hemminger, *J.Am.Chem.Soc.* **2009**, *131*, 8354.
- [138] B. Winter, R. Weber, P. M. Schmidt, I. V. Hertel, M. Faubel, L. Vrbka, P. Jungwirth, *J.Phys.Chem.B* **2004**, *108*, 14558.
- [139] B. Winter, R. Weber, I. V. Hertel, M. Faubel, L. Vrbka, P. Jungwirth, *Chem.Phys.Lett.* **2005**, *410*, 222.
- [140] P. Jungwirth, B. Winter, *Ann.Rev.Phys.Chem.* **2008**, *59*, 343.
- [141] N. Ottosson, R. Vacha, E. F. Aziz, W. Pokapanich, W. Eberhardt, S. Svensson, G. Ohrwall, P. Jungwirth, O. Björneholm, B. Winter, *J.Chem.Phys.* **2009**, *131*.
- [142] B. Winter, M. Faubel, I. V. Hertel, C. Pettenkofer, S. E. Bradforth, B. Jagoda-Cwiklik, L. Cwiklik, P. Jungwirth, *J.Am.Chem.Soc.* **2006**, *128*, 3864.

- [143] D. Nolting, T. Schultz, I. V. Hertel, R. Weinkauff, *Phys.Chem.Chem.Phys.* **2006**, *8*, 5247.
- [144] D. Nolting, R. Weinkauff, I. V. Hertel, T. Schultz, *ChemPhysChem* **2007**, *8*, 751.
- [145] B. Jagoda-Cwiklik, P. Slavíček, L. Cwiklik, D. Nolting, B. Winter, P. Jungwirth, *J.Phys.Chem.A* **2008**, *112*, 3499.
- [146] B. Jagoda-Cwiklik, P. Slavíček, D. Nolting, B. Winter, P. Jungwirth, *J.Phys.Chem.B* **2008**, *112*, 7355.
- [147] D. Nolting, N. Ottosson, M. Faubel, I. V. Hertel, B. Winter, *J.Am.Chem.Soc.* **2008**, *130*, 8150.
- [148] P. Slavicek, B. Winter, M. Faubel, S. E. Bradforth, P. Jungwirth, *J.Am.Chem.Soc.* **2009**, *131*, 6460.
- [149] E. F. Aziz, S. Eisebitt, W. Eberhardt, L. Cwiklik, P. Jungwirth, *J.Phys.Chem.B* **2008**, *112*, 1262.
- [150] S. Bonhommeau, N. Ottosson, W. Pokapanich, S. Svensson, W. Eberhardt, O. Björneholm, E. F. Aziz, *J.Phys.Chem.B* **2008**, *112*, 12571.
- [151] E. F. Aziz, N. Ottosson, S. Eisebitt, W. Eberhardt, B. Jagoda-Cwiklik, R. Vacha, P. Jungwirth, B. Winter, *J.Phys.Chem.B* **2008**, *112*, 12567.
- [152] N. Ottosson, E. F. Aziz, H. Bergersen, W. Pokapanich, G. Ohrwall, S. Svensson, W. Eberhardt, O. Björneholm, *J.Phys.Chem.B* **2008**, *112*, 16642.
- [153] H. Conrad, F. Lehmkuhler, C. Sternemann, A. Sakko, D. Paschek, L. Simonelli, S. Huotari, O. Feroughi, M. Tolan, K. Hamalainen, *Phys.Rev.Lett.* **2009**, *103*, 218301.
- [154] M. B. Hay, S. C. B. Myneni, *J.Phys.Chem.A* **2010**, *114*, 6138.
- [155] F. Lehmkuhler, A. Sakko, C. Sternemann, M. Hakala, K. Nygard, C. J. Sahle, S. Galambosi, I. Steinke, S. Tiemeyer, A. Nyrow, T. Buslaps, D. Pontoni, M. Tolan, K. HAMALAINEN, *Journal of Physical Chemistry Letters* **2010**, *1*, 2832.
- [156] R. G. Wilks, J. B. MacNaughton, H. B. Kraatz, T. Regier, A. Moewes, *J.Phys.Chem.B* **2006**, *110*, 5955.
- [157] E. F. Aziz, A. Zimina, M. Freiwald, S. Eisebitt, W. Eberhardt, *J.Chem.Phys.* **2006**, *124*, 114502.
- [158] *StoBe-deMon version 2.2*, Herrmann, K., Pettersson, L. G. M., Casida, M. E., Daul, C., Goursot, A., Koester, A., Proynov, E., St-Amant, A., and Salahub, D. R., **2006**, Berlin, Stockholm.
- [159] E. F. Aziz, M. Freiwald, S. Eisebitt, W. Eberhardt, *Phys.Rev.B* **2006**, *73*, 075120.
- [160] D. Nolting, E. F. Aziz, N. Ottosson, M. Faubel, I. V. Hertel, B. Winter, *J.Am.Chem.Soc.* **2007**, *129*, 14068.
- [161] M. A. Brown, F. Vila, M. Sterrer, S. Thurmer, B. Winter, M. Ammann, J. J. Rehr, J. A. van Bokhoven, *Journal of Physical Chemistry Letters* **2012**, *3*, 1754.
- [162] J. S. Stevens, S. J. Byard, C. C. Seaton, G. Sadiq, R. J. Davey, S. L. M. Schroeder, *Angew.Chemie - Int.Ed.* **2011**, *50*, 9916.
- [163] J. S. Stevens, S. J. Byard, S. L. M. Schroeder, *Cryst.Growth Des.* **2010**, *10*, 1435.

- [164] J. S. Stevens, S. J. Byard, S. L. M. Schroeder, *J.Pharm.Sci.* **2010**, *99*, 4453.
- [165] J. S. Stevens, S. J. Byard, C. A. Muryn, S. L. M. Schroeder, *J.Phys.Chem.B* **2010**, *114*, 13961.
- [166] J. S. Stevens, S. J. Byard, E. Zlotnikov, S. L. M. Schroeder, *J.Pharm.Sci.* **2011**, *100*, 942.
- [167] G. Will, *Nature* **1963**, *198*, 575.
- [168] S. Martinez, *Acta Cryst.* **1966**, *20*, 783.
- [169] B. M. Craven, R. K. McMullan, J. D. Bell, H. C. Freeman, *Acta Crystallographica Section B-Structural Science* **1977**, *33*, 2585.
- [170] E. Apen, A. P. Hitchcock, J. L. Gland, *J.Phys.Chem.* **1993**, *97*, 6859.
- [171] L. Colombo, *J.Chem.Phys.* **1968**, *49*, 4688.
- [172] H. Zimmermann, *Zeitschrift fur Elektrochemie* **1961**, *65*, 821.
- [173] T. C. Damen, S. P. S. Porto, B. Tell, *Phys.Rev.* **1966**, *142*, 570.
- [174] A. Kastler, *Comptes Rendus Hebdomadaires des Seances de l Academie des Sciences* **1948**, *227*, 1024.
- [175] L. Giulotto, G. Olivelli, *J.Chem.Phys.* **1948**, *16*, 555.
- [176] C. Perchard, A. M. Bellocq, A. Novak, *Journal de Chimie Physique* **1965**, *62*, 1344.
- [177] C. Perchard, A. Novak, *J.Chem.Phys.* **1968**, *48*, 3079.
- [178] W. Maier, O. Schifferdecker, *Spectrochim.Acta* **1962**, *18*, 709.
- [179] M. Majoube, *J.Mol.Struct.* **1980**, *61*, 129.
- [180] S. A. Asher, J. L. Murtaugh, *Appl.Spectrosc.* **1988**, *42*, 83.
- [181] N. Agmon, *Chem.Phys.Lett.* **1995**, *244*, 456.
- [182] B. S. Hickman, M. Mascal, J. J. Titman, I. G. Wood, *J.Am.Chem.Soc.* **1999**, *121*, 11486.
- [183] J. T. Daycock, G. P. Jones, J. R. N. Evans, J. M. Thomas, *Nature* **1968**, *218*, 672.
- [184] Y. A. Borisov, N. P. Vorobeva, I. A. Abronin, A. F. Kolomiets, *Bulletin of the Academy of Sciences of the Ussr Division of Chemical Science* **1988**, *37*, 2504.
- [185] H. Walba, R. W. Isensee, *J.Org.Chem.* **1961**, *26*, 2789.
- [186] H. Walba, R. W. Isensee, *J.Org.Chem.* **1956**, *21*, 702.
- [187] U. Domanska, M. K. Kozłowska, M. Rogalski, *Journal of Chemical and Engineering Data* **2002**, *47*, 456.
- [188] W. Hüchel, J. Datow, E. Simmersbach, *Z.Phys.Chem.Abt.A* **1940**, *186*, 129.
- [189] R. Wolff, *Angew.Chemie - Int.Ed.* **1955**, *67*, 89.
- [190] D. M. W. Anderson, J. L. Duncan, F. J. C. Rossotti, *J.Chem.Soc.* **1961**, 2165.

- [191] H. Zimmermann, N. Joop, *Zeitschrift fur Elektrochemie* **1962**, 66, 766.
- [192] N. JOOP, H. Zimmermann, *Zeitschrift fur Elektrochemie* **1962**, 66, 541.
- [193] N. JOOP, H. Zimmermann, *Zeitschrift fur Physikalische Chemie-Frankfurt* **1964**, 42, 61.
- [194] H. Zimmermann, *Angew.Chemie - Int.Ed.* **1964**, 3, 157.
- [195] A. Lukton, *Nature* **1961**, 192, 422.
- [196] W. Otting, *Chemische Berichte-Recueil* **1956**, 89, 2887.
- [197] K. Pralat, G. Czechowski, *J.Mol.Liquids* **1988**, 38, 147.
- [198] S. M. Wang, L. Y. Lee, J. T. Chen, *Spectrochimica Acta Part A-Molecular and Biomolecular Spectroscopy* **1979**, 35, 765.
- [199] F. Peral, E. Gallego, *J.Mol.Struct.* **1997**, 415, 187.
- [200] L. Gontrani, R. Caminiti, L. Bencivenni, C. Sadun, *Chem.Phys.Lett.* **1999**, 301, 131.
- [201] M. S. Shaik, S. Y. Liem, Y. N. Yuan, P. L. A. Popelier, *Phys.Chem.Chem.Phys.* **2010**, 12, 15040.
- [202] S. Y. Liem, M. S. Shaik, P. L. A. Popelier, *J.Phys.Chem.B* **2011**, 115, 11389.
- [203] J. Zischang, J. J. Lee, M. A. Suhm, *J.Chem.Phys.* **2011**, 135, 061102.
- [204] IXAS Resources: Books and Codes,
http://www.ixasportal.net/ixas/index.php?option=com_content&view=article&id=92&Itemid=250, **2013**.
- [205] S. I. Zabinsky, J. J. Rehr, A. Ankudinov, R. C. Albers, M. J. Eller, *Phys.Rev.B* **1995**, 52, 2995.
- [206] A. L. Ankudinov, B. Ravel, J. J. Rehr, S. D. Conradson, *Phys.Rev.B* **1998**, 58, 7565.
- [207] J. J. Rehr, A. Ankudinov, S. I. Zabinsky, *Catal.Today* **1998**, 39, 263.
- [208] A. L. Ankudinov, J. J. Rehr, *Geochimica et Cosmochimica Acta* **2005**, 69, A601.
- [209] E. Z. Kurmaev, A. L. Ankudinov, J. J. Rehr, L. D. Finkelstein, P. F. Karimov, A. Moewes, *J.Electron Spectrosc.Relat.Phenom.* **2005**, 148, 1.
- [210] J. J. Rehr, A. L. Ankudinov, *Coordination Chemistry Reviews* **2005**, 249, 131.
- [211] A. L. Ankudinov, W. T. Elam, J. R. Sieber, J. J. Rehr, *X-ray Spectrom.* **2006**, 35, 312.
- [212] T. Jiang, D. E. Ellis, *J.Mater.Res.* **1996**, 11, 2242.
- [213] H. Nakamatsu, T. Mukoyama, H. Adachi, *Chem.Phys.* **1990**, 143, 221.
- [214] H. Nakamatsu, T. Mukoyama, H. Adachi, *J.Chem.Phys.* **1991**, 95, 3167.
- [215] I. Tanaka, J. Kawai, H. Adachi, *Phys.Rev.B* **1995**, 52, 11733.
- [216] S. Yamashita, M. Fujiwara, Y. Kato, T. Yamaguchi, H. Wakita, H. Adachi, *Advances in Quantum Chemistry, Vol.29: Electronic Structure of Clusters* **1997**, 29, 357.

- [217] S. Matsuo, N. Sakaguchi, E. Obuchi, K. Nakano, R. C. C. Perera, T. Watanabe, T. Matsuo, H. Wakita, *Anal.Sci.* **2001**, *17*, 149.
- [218] H. Nakamatsu, *Chem.Phys.* **1995**, *200*, 49.
- [219] A. M. Duffin, C. P. Schwartz, A. H. England, J. S. Uejio, D. Prendergast, R. J. Saykally, *J.Chem.Phys.* **2011**, *134*, 154503.
- [220] S. Fatehi, C. P. Schwartz, R. J. Saykally, D. Prendergast, *J.Chem.Phys.* **2010**, *132*, 094302.
- [221] C. P. Schwartz, J. S. Uejio, R. J. Saykally, D. Prendergast, *J.Chem.Phys.* **2009**, *130*, 184109.
- [222] P. W. Atkins, *Physical Chemistry*, 6 ed. Oxford University Press:Oxford, **1998**, p. 401.
- [223] ESRF Brochure, European Synchrotron Radiation Facility (ESRF), **1996**.
- [224] Aziz, E. F., Freie Universität Berlin, **2007**.
- [225] L. Triguero, L. G. M. Pettersson, *Surf.Sci.* **1998**, *398*, 70.
- [226] L. Triguero, L. G. M. Pettersson, B. F. Minaev, H. Agren, *J.Chem.Phys.* **1998**, *108*, 1193.
- [227] S. H. Vosko, L. Wilk, *Phys.Rev.B* **1980**, *22*, 3812.
- [228] C. Kolczewski, R. Püttner, O. Plashkevych, H. Agren, V. Staemmler, M. Martins, G. Snell, A. S. Schlachter, M. Sant'Anna, G. Kaindl, L. G. M. Pettersson, *J.Chem.Phys.* **2001**, *115*, 6426.
- [229] L. Triguero, L. G. M. Pettersson, H. Agren, *J.Phys.Chem.A* **1998**, *102*, 10599.
- [230] L. Triguero, L. G. M. Pettersson, H. Agren, *Phys.Rev.B* **1998**, *58*, 8097.
- [231] D. P. Chong, C. H. Hu, P. Duffy, *Chem.Phys.Lett.* **1996**, *249*, 491.
- [232] C. H. Hu, D. P. Chong, *Chem.Phys.Lett.* **1996**, *262*, 729.
- [233] M. Stener, A. Lisini, P. Decleva, *Chem.Phys.* **1995**, *191*, 141.
- [234] *Gaussian 03, Revision C.02*, Frisch, M. J., Trucks, G. W., Schlegel, H. B., Scuseria, G. E., Robb, M. A., Cheeseman, J. R., Montgomery Jr, J. A., Vreven, T., Kudin, K. N., Burant, J. C., Millam, J. M., Iyengar, S. S., Tomasi, J., Barone, V., Mennucci, B., Cossi, M., Scalmani, G., Rega, N., Petersson, G. A., Nakatsuji, H., Hada, M., Ehara, M., Toyota, K., Fukuda, R., Hasegawa, J., Ishida, M., Nakajima, T., Honda, Y., Kitao, O., Nakai, H., Klene, M., Li, X., Knox, J. E., Hratchian, H. P., Cross, J. B., Bakken, V., Adamo, C., Jaramillo, J., Gomperts, R., Stratmann, R. E., Yazyev, O., Austin, A. J., Cammi, R., Pomelli, C., Ochterski, J. W., Ayala, P. Y., Morokuma, K., Voth, G. A., Salvador, P., Dannenberg, J. J., Zakrzewski, V. G., Dapprich, S., Daniels, A. D., Strain, M. C., Farkas, O., Malick, D. K., Rabuck, A. D., Raghavachari, K., Foresman, J. B., Ortiz, J. V., Cui, Q., Baboul, A. G., Clifford, S., Cioslowski, J., Stefanov, B. B., Liu, G., Liashenko, A., Piskorz, P., Komaromi, I., Martin, R. L., Fox, D. J., Keith, T., Al-Laham, M. A., Peng, C. Y., Nanayakkara, A., Challacombe, M., Gill, P. M. W., Johnson, B., Chen, W., Wong, M. W., Gonzalez, C., and Pople, J. A., **2004**, Gaussian, Inc.:Wallingford, CT.
- [235] J. A. Pople, H. B. Schlegel, R. Krishnan, D. J. Defrees, J. S. Binkley, M. J. Frisch, R. A. Whiteside, R. F. Hout, W. J. Hehre, *Int.J.Quantum Chem.* **1981**, *20*, 269.
- [236] L. Onsager, *J.Am.Chem.Soc.* **1936**, *58*, 1486.

- [237] S. Miertus, J. Tomasi, *Chem.Phys.* **1982**, *65*, 239.
- [238] M. W. Wong, K. B. Wiberg, M. Frisch, *J.Chem.Phys.* **1991**, *95*, 8991.
- [239] J. B. Foresman, T. A. KEITH, K. B. Wiberg, J. Snoonian, M. J. Frisch, *The Journal of Physical Chemistry* **1996**, *100*, 16098.
- [240] S. J. Clark, M. D. Segall, C. J. Pickard, P. J. Hasnip, M. J. Probert, K. Refson, M. C. Payne, *Zeitschrift fur Kristallographie* **2005**, *220*, 567.
- [241] M. D. Segall, P. J. D. Lindan, M. J. Probert, C. J. Pickard, P. J. Hasnip, S. J. Clark, M. C. Payne, *Journal of Physics-Condensed Matter* **2002**, *14*, 2717.
- [242] W. Frentrup, D. Schröder, R. Manzke, *J.Phys.IV France* **1997**, 7-C2.
- [243] L. Tröger, E. Zschech, D. Arvanitis, K. Baberschke, *Jpn.J.Appl.Phys* **1993**, 32-2, 144.
- [244] S. Eisebitt, T. Böske, J.-E. Rubensson, W. Eberhardt, *Phys.Rev.B* **1993**, *47*, 14103.
- [245] Z. Tan, J. I. Budnick, S. M. Heald, *Rev.Sci.Instrum.* **1989**, *60*, 1021.
- [246] D. M. Pease, D. L. Brewes, Z. Tan, J. I. Budnick, C. C. Law, *Phys.Letters A* **1989**, *138*, 230.
- [247] J. Goulon, C. Goulon-Ginet, R. Cortes, J. M. Dubois, *J.Phys.France* **1982**, *43*, 539.
- [248] S. P. Gao, C. J. Pickard, A. Perlov, V. Milman, *Journal of Physics-Condensed Matter* **2009**, *21*, 104203.
- [249] S. P. Gao, C. J. Pickard, M. C. Payne, J. Zhu, J. Yuan, *Phys.Rev.B* **2008**, *77*, 115122.
- [250] Pickard, C. J., University of Cambridge, **2007**.
- [251] J. D. Pack, H. J. Monkhorst, *Phys.Rev.B* **1977**, *16*, 1748.
- [252] H. J. Monkhorst, J. D. Pack, *Phys.Rev.B* **1976**, *13*, 5188.
- [253] C. R. Seabourne, A. J. Scott, R. Brydson, R. J. Nicholls, *Ultramicroscopy* **2009**, *109*, 1374.
- [254] M. Thomason, G. Hembury, E. F. Aziz, C. R. Seabourne, A. J. Scott, S. L. M. Schroeder, *Phys.Chem.Chem.Phys.* **2012**, *in preparation*.
- [255] C. R. Seabourne, *Unpublished results* **2012**.
- [256] J. S. Stevens, A. C. de Luca, M. Pelendritis, G. Terenghi, S. Downes, S. L. M. Schroeder, *Surf.Interface Anal.* **2012**, *submitted*.
- [257] P. Edington, M. M. Harding, *Acta Cryst.B* **1974**, *30*, 204.
- [258] S. T. King, *The Journal of Physical Chemistry* **1970**, *74*, 2133.
- [259] M. Majoube, G. Vergoten, *J.Mol.Struct.* **1992**, *266*, 345.
- [260] T. N. Wassermann, C. A. Rice, M. A. Suhm, D. Luckhaus, *J.Chem.Phys.* **2007**, *127*, 234309.

Appendix I: N K-edge NEXAFS data of obtained using an open stagnant solution cell

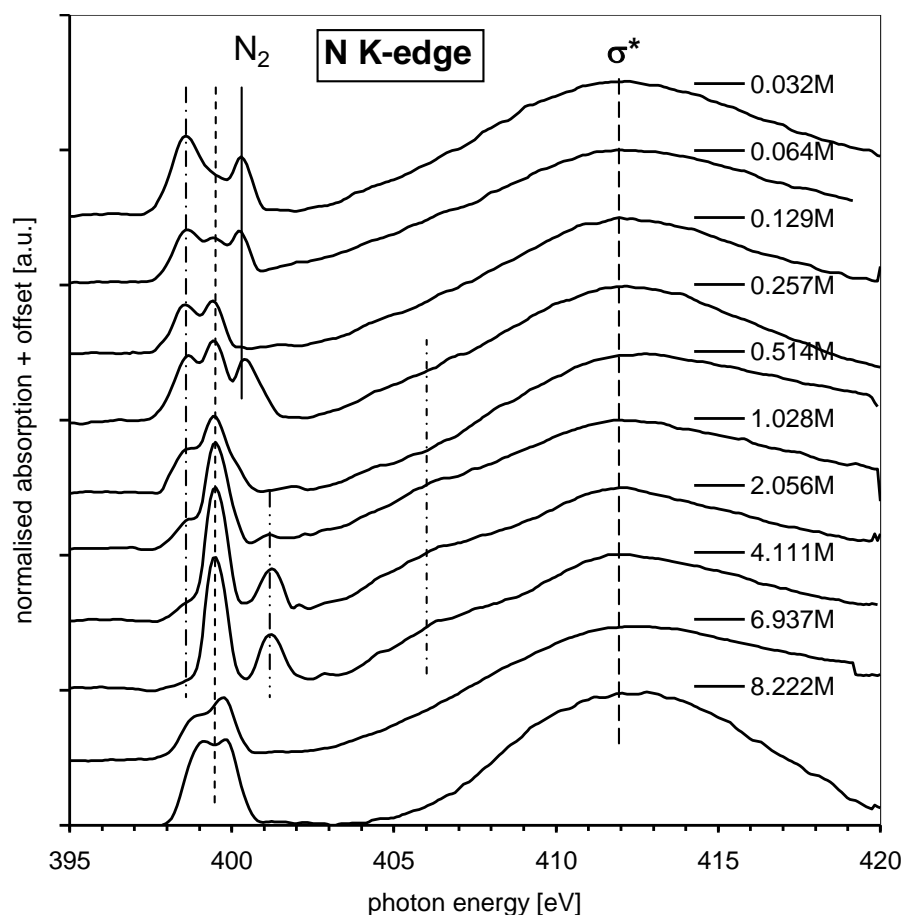


Figure 69 Experimental N K-edge NEXAFS data of aqueous imidazole solutions from 0.03 M to 8.2 obtained in an open stagnant container cell enclosed in a He-filled chamber. These data were acquired during an initial run at BESSY, but indicated a number of problems with the setup. First, air ingress resulted in contamination of the data by emission from gaseous N_2 ; evaporation of solvent led to the detection of solid imidazole (bottom spectrum) at the saturation concentration; later studies (see chapter 6) with a flow cell indicated that beam damage and other restructuring effects may take place under stagnant conditions.

Appendix II: Co-Authored Publication

Journal of Physics: Conference Series 190 (2009) 012156.

Continuous Tubular Flow Reactor for XAFS Studies of Organometallic Reactions: Possibilities and Limitations for Studies of the Soai Reaction

Luanga N. Nchari¹, Guy A. Hembury¹, Angela M. Beesley¹, David J. Meehan², Nikolaos Tsapatsaris¹, Matthew Hudson¹, Matthew Thomason² and Sven L.M Schroeder^{1,2}

(1) School of Chemical Engineering and Analytical Science, The University of Manchester, PO Box 88, Manchester, M60 1QD, UK

(2) School of Chemistry, The University of Manchester, Oxford Road, Manchester, M13 9PL, UK

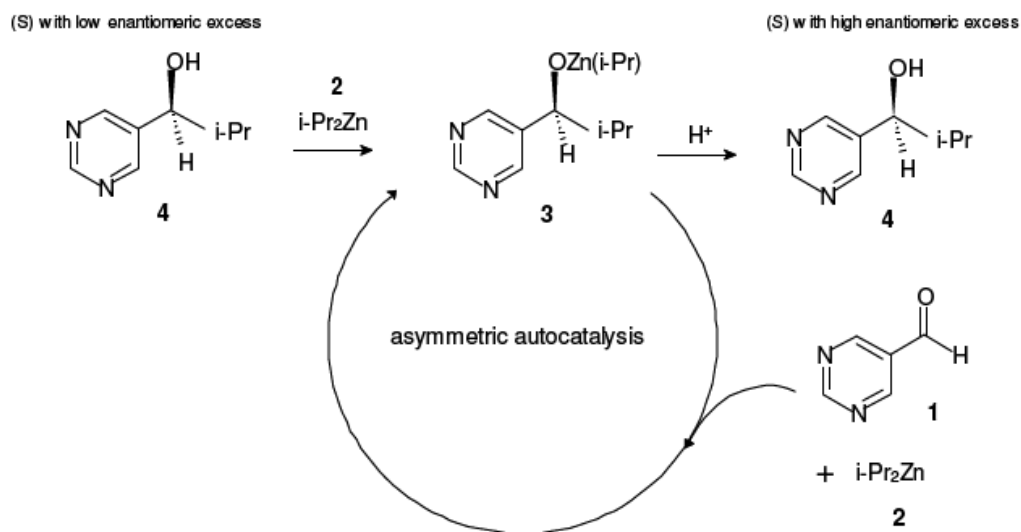
s.schroeder@manchester.ac.uk

Abstract. A computer-controlled continuous tubular flow reactor system has been commissioned that permits time-resolved *in situ* XAFS measurements of organometallic reactions. The system was commissioned by Zn K-edge measurements of products formed during the Soai reaction. XANES data are shown that illustrate the quality of the data that can be achieved. The XANES spectra are compatible with the presence of dimer, trimer or other oligomeric alkoxide species in the Soai process. It is shown how heterogeneity in the Soai reaction system leads to considerable complications with the measurements due to the formation of floating particles of the aldehyde/*i*Pr₂Zn adduct formed in the reaction; additionally, decomposition of *i*Pr₂Zn with residual air and moisture leads to deposits on cell walls.

1. Introduction

Alkylations of pyrimidyl aldehydes (Scheme 1) by diisopropylzinc have over the last two decades received considerable attention because they represent an amplifying asymmetric autocatalytic reaction mechanism that can, in principle, achieve homochiral products in an essentially non-chiral environment.¹ The reaction has initially been developed by Soai and co-workers²⁻⁵ and is therefore often referred to as the ‘Soai’ reaction. A pyrimidyl aldehyde **1** reacts with diisopropylzinc **2** to an organozinc complex **3**, from which the pyrimidyl alcohol (product **4**) can be obtained by hydrolysis. Chiral amplification in this reaction occurs because the chiral product **3** transfers the unreacted isopropyl group enantioselectively, forming the pyrimidyl alcohol **4**, which can then react with further diisopropylzinc **2** to form the same product. In other words, **4** is both the product of the alkylation *and* the chiral auxiliary, so the overall process is autocatalytic and strong amplification of chirality can be achieved.

Elucidating the structural nature of the intermediate(s) involved in the decisive autocatalytic step of the reaction will be crucial for a deep understanding of the chiral amplification process. Mechanistic details of the reaction have until now been derived only from computational studies of possible intermediates, NMR-studies of the relevant species in solution, and by calorimetric studies of



Scheme 1. An example of a Soai autocatalytic reaction.

the reaction kinetics.⁶⁻¹⁰ Organometallic zinc complexes that are monomeric, dimeric, trimeric or even tetrameric have been proposed as possible candidates for the chiral intermediate that achieves the autocatalytic selection of only one product enantiomer. We have now undertaken the first studies of the reaction by X-ray Absorption Fine Structure (XAFS) spectroscopy at the Zn K-edge, to obtain structural information about the local environment of zinc in the reaction media.

2. Experimental

The *in situ* flow XAFS measurements at the Zn K-edge were performed at station 9.3 of the SRS, UK, and at 12ID-B¹¹ of the Advanced Photon Source (APS) at Argonne National Laboratory (USA). Supporting work with non-flowing solutions was performed using sealed Eppendorf microcentrifuge tubes¹³ at BM29 of the ESRF, Grenoble, France. Solutions were loaded into the microcentrifuge tubes in a glove bag continuously purged with dry N₂. All reactions were performed at room temperature. At all three beamlines simultaneous measurements in transmission mode with gas ionization chambers and by fluorescence-yield (FY) detection with multielement Ge detectors were performed. Reactants and dry toluene solvent were obtained from Aldrich.

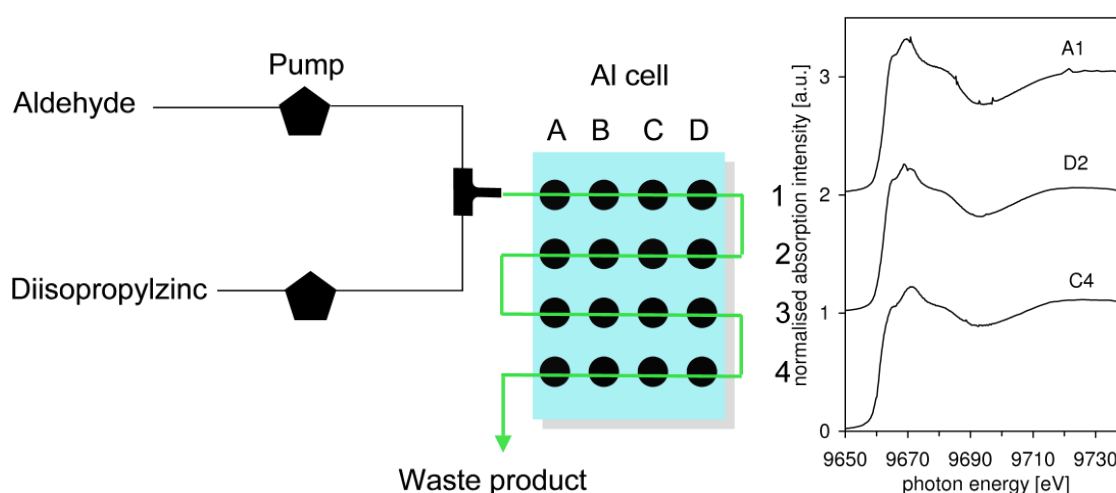


Figure 1. Schematic arrangement of the PTFE tubular flow reactor mounted on a heatable Al frame; also shown are representative *in situ* Zn K-edge FY XANES data taken at positions A1, D2 and C4 during the Soai reaction with a 1:1 volume mixture of 0.1 mol L diisopropylzinc and pyrimidyl aldehyde solutions.

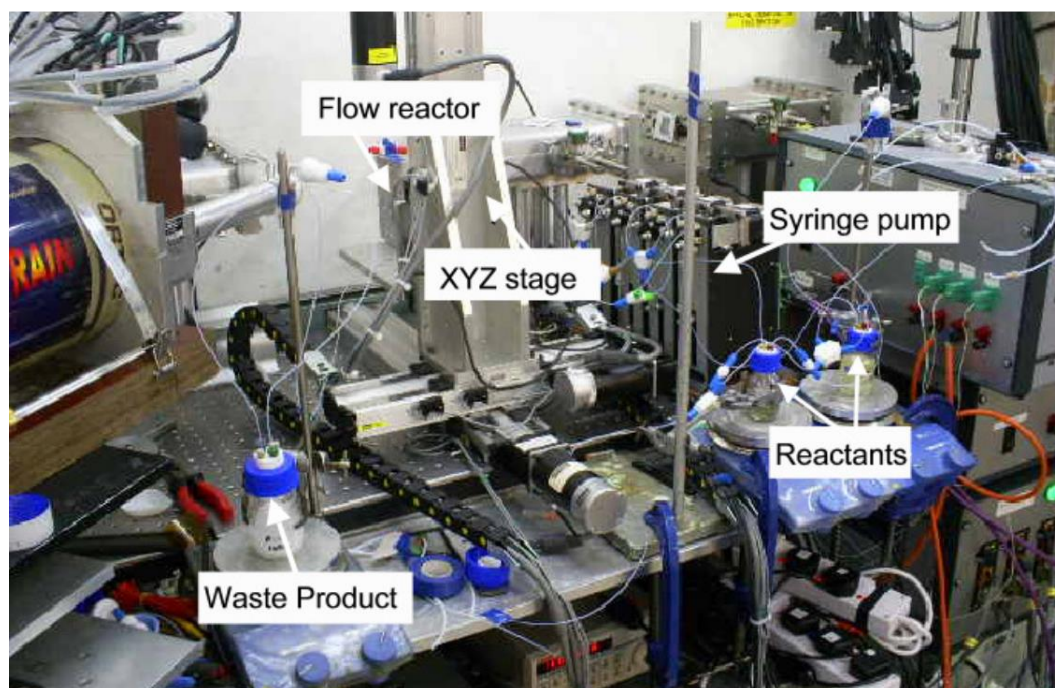


Figure 2. Tubular flow reactor assembled at station 9.3, Daresbury UK.

The flow reactor was based on PTFE tubing (1/8 inch outer diameter) attached to an aluminium support frame that had 16 holes in a regular 4×4 pattern machined out of it (see schematic sketch in figure 1). At the positions of these holes *in situ* monitoring of the reaction progress along the tube was possible by combined transmission and fluorescence-yield detection. For our studies of the Soai reaction the pyrimidyl aldehyde and diisopropylzinc were mixed at the tube inlet by joining the two solution streams in a PTFE ‘T’-piece (Omnifit). The solution streams were provided by syringe pumps (Versa 6, Kloehn) fitted with 1 mL syringes and non-distribution valves; they were controlled remotely *via* a serial interface with a LabVIEW (National Instruments) GUI. A pair of syringe pumps was used for each of the two reactants (0.1 mol L⁻¹ diisopropylzinc and pyrimidyl aldehyde solutions). Handshaking operation synchronised the pump pairs: while one pump was dispensing the other was aspirating in preparation for subsequent dosing. As mentioned above, due to the oxygen and moisture sensitivity of this iPr₂Zn solution a nitrogen atmosphere was needed to keep the environment inert within the pump pairs and flow cell apparatus. This was achieved by including a nitrogen feed on the multiport pump-head and purging before introduction of iPr₂Zn solution. The reactant solutions were also prepared and stored under nitrogen. By varying the flow rate from the dosing pumps it is possible to tune the flow rate in the reactor to obtain information about the nature of metal species as a function of reaction time. Positioning in the X-ray beam was achieved by using a computer controlled XYZ stage calibrated to the dimensions of the reactor system. FY XANES data obtained at the APS during the reaction in a solution containing 0.1 mol L⁻¹ of pyrimidyl aldehyde and 0.1 mol L⁻¹ diisopropylzinc are included in figure 1. A photograph of the completely assembled system at station 9.3 of the SRS is shown in figure 2.

3. Results and Discussion

3.1 Flow Experiments

The XANES data from figure 1 indicate that under the chosen flow conditions the reaction had progressed almost to completion at the initial measurement point, A1. Only minor spectral changes

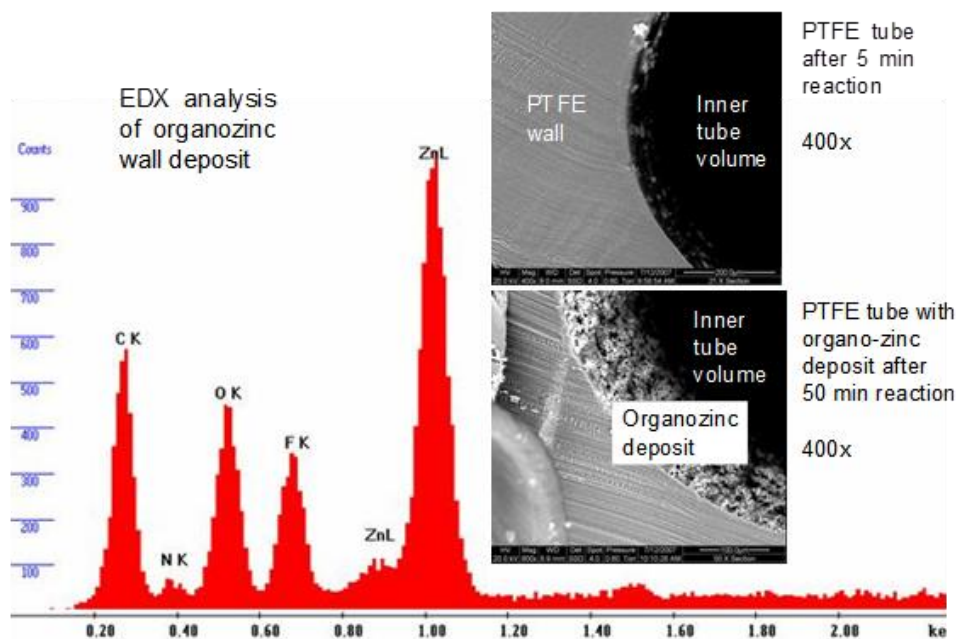


Figure 3. EDX analysis of the organozinc wall deposit on the inside of the PTFE reactor tube.

occur as the reaction progresses towards positions D2 and C4. The appearance of occasional ‘spikes’ in the XANES data shown in figure 1 was traced to the formation of small floating particles of a precipitate formed by the Soai process. We found that particles moving into and out of the X-ray beam would cause such distortions of the spectra, which were especially strong in transmission mode. In fact, several runs of experiments were rendered uninterpretable by the resulting presence of strong non-random noise. In addition to the observed formation of a precipitate a strongly adherent wall deposit became apparent during the flow reactor experiments. These stationary deposits additionally influenced the XANES spectra. They form because the velocity of the flowing solution near the wall is lower than in the inner volume of the tube. The extent to which wall deposits can grow quickly is illustrated by electron microscopic images in figure 3. The lower of the two images shows that after running the Soai reaction for 50 min the deposit had a thickness of 5 μm . *Ex situ* energy-dispersive X-ray (EDX) analysis (figure 3) confirmed that the deposit contains ZnO and organozinc material. It seems likely that the formation of such wall deposits can only be suppressed if the reactor design is modified to maintain a high space velocity of the reaction medium, for example through strong turbulent flow or shear, near the wall where the XAFS measurements take place. Abrupt changes of flow direction or introduction of constricted regions on the tube may achieve this objective. The XANES data included in figure 1 are reminiscent of the Zn K-edge XANES of Zn^{2+} species in a tetrahedral environment, such as ZnO ¹². This is illustrated in figure 4, in which the spectrum from position C4 is compared to a previously published¹² spectrum of solid crystalline ZnO . It can be seen that the energetic positions of the shoulder at ~ 9664 eV, the main resonance at ~ 9669 eV and the broad resonance around ~ 9682 eV coincide. Note however that the amplitudes of the XANES resonances of the Soai product, and especially the features in the EXAFS region (e.g., at ~ 9717 eV), are strongly reduced, indicating disorder relative to crystalline ZnO on one hand and the presence of a significant self-absorption effect, likely associated with the formation of the observed solid product on the other. It appears that deposition of a poorly ordered ZnO and/or $\text{Zn}(\text{OH})_2$ product.

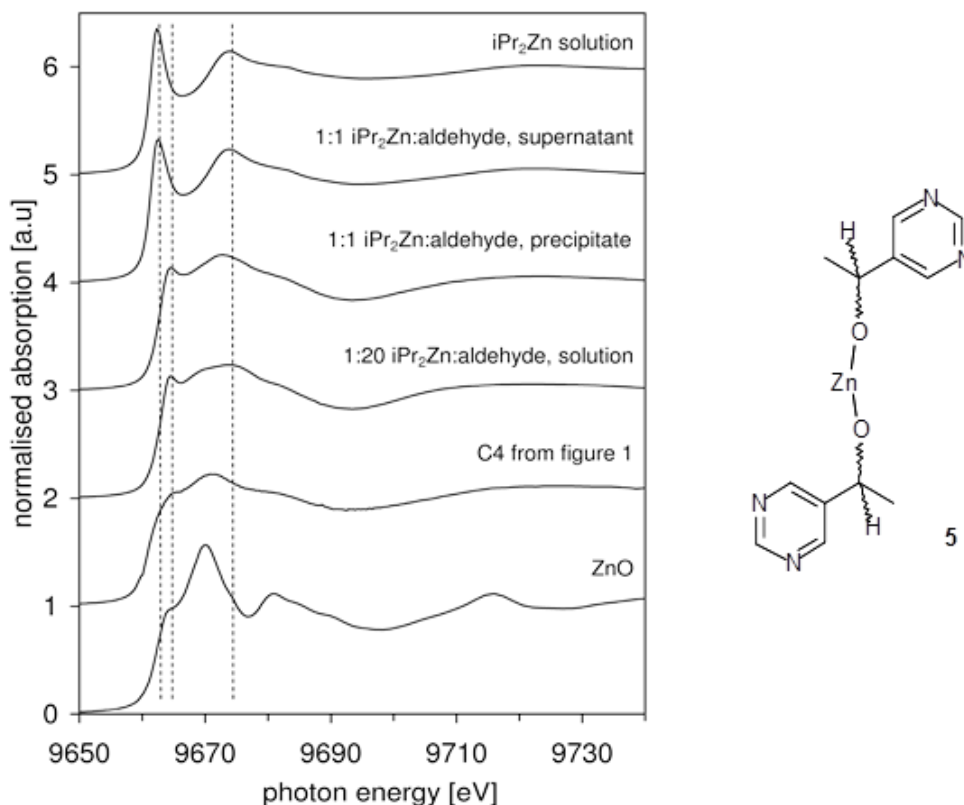


Figure 4. *In situ* transmission XANES (BM29, ESRF) obtained in microcentrifuge tubes. From top to bottom: Zn K-edge XANES spectra of a toluene solution containing 0.1 M diisopropylzinc; the supernatant of a solution formed by reacting 0.1 M diisopropylzinc and 0.1 M pyrimidine aldehyde in toluene; the sediment formed in this solution; a toluene solution containing 0.1 M diisopropylzinc and 2 M pyrimidine aldehyde; the spectrum labelled C4 in figure 1 (measured at the SRS); a spectrum of ZnO¹².

takes place on the wall of the reactor tube and dominates the observed XAFS spectrum. The most likely origin is the presence of residual water and/or O₂ in the reaction system, decomposing diisopropylzinc to Zn(OH)₂ and ZnO, respectively.

3.2 Products of Soai Process under Non-Flow Conditions

Experiments with a sealed static reactor cell (a standard Eppendorf polypropylene microcentrifuge tube¹³) allowed us to minimise the formation of wall deposits and to selectively characterise the precipitate formed by the Soai process. This was achieved by allowing sedimentation of the precipitate at the bottom of the microcentrifuge tube, which also enabled us to separately examine the remaining supernatant solution. Figure 4 contains the resulting transmission XANES spectra of the sedimented precipitate (3rd spectrum from top) and of the supernatant solution (2nd spectrum from top) obtained by mixing 0.1 mol L⁻¹ aldehyde and 0.1 mol L⁻¹ iPr₂Zn in toluene in a 1:1 molar ratio. It can be seen by comparison with the spectrum of iPr₂Zn in toluene (top spectrum) that any Zn species remaining in the supernatant solution stem from unreacted iPr₂Zn. In contrast, the spectrum of the sedimented precipitate (second spectrum from top) has no strong white line, indicating that p-like valence states are occupied and that the local bonding and/or coordination geometry are fundamentally different from that in iPr₂Zn. For a 1:1 mixture of iPr₂Zn and

aldehyde one would statistically expect a product mixture containing unreacted iPr_2Zn as well as the monomeric species **3** (Scheme 1) and some monomeric dialkoxide species **5** (figure 3). To address which of these species was responsible for the observed spectrum we carried out the reaction of iPr_2Zn with a 20-fold excess of aldehyde because this reaction is expected to result in the formation of only the dialkoxide **5**. Interestingly, the XANES spectrum of this product (3rd spectrum from bottom in figure 3) is very similar to the spectrum of the precipitate formed in the 1:1 mixture, indicating that the dialkoxide is preferentially formed even when understoichiometric amounts of aldehyde are supplied. What is currently not clear is whether the precipitate contains the monomeric species **5** or whether the previously proposed⁶⁻¹⁰ dimers, trimers or oligomers of **5** are formed. In these products the Zn centres would be in a distorted tetrahedral coordination environment,¹⁰ which is compatible with the overall appearance of the spectra and especially the absence of the strong white line in the XANES spectra of the observed product.

4. Conclusions

A fully computer-controlled continuous tubular flow reactor system for time-resolved *in situ* XAFS measurements has been commissioned. Zn K-edge XANES data demonstrate that with 3rd generation synchrotron beam spectra of very good quality can be achieved with Zn concentrations in the 100 mmol region. Heterogeneous processes in the Soai reaction lead to considerable complications with the measurements due to the formation of floating particles of the aldehyde/ iPr_2Zn adduct formed in the reaction, while the deposition of solid iPr_2Zn decomposition products on the walls of the flow reactor dominates the spectra after less than an hour of continuous reaction. The Soai precipitate formed in 1:1 iPr_2Zn :aldehyde mixtures appears to be the dialkoxide complex, while the remaining supernatant still contains unreacted iPr_2Zn . The XANES data for the dialkoxide do not exclude the presence of non-monomeric species; that a precipitate is observed supports the notion that the formation of dimers, trimers, tetramers or higher oligomers takes place.

5. Acknowledgments

This project was supported by EPSRC under grant EP/D023807/1. We thank the SRS (UK), the APS (USA) and the ESRF (France) for the allocation of beamtime for this project.

References

1. Buono, F. G.; Iwamura, H.; Blackmond, D. G., *Ang. Chem. -Int. Ed.* 2004, 43, 2099.
2. Soai, K.; Kawasaki, T., *Chirality* 2006, 18, 469.
3. Soai, K.; Shibata, T., *J. Synth. Org. Chem. Japan* 1997, 55, 994.
4. Soai, K.; Niwa, S., *Chem. Rev.* 1992, 92, 833.
5. Todd, M. H., *Chem. Soc. Rev.* 2002, 31, 211.
6. Gridnev, I. D.; Serafimov, J. M.; Quiney, H.; Brown, J. M., *Org. Biomol. Chem.* 2003, 1, 3811.
7. Islas, J. R.; Lavabre, D.; Grevy, J. M.; Lamonedá, R. H.; Cabrera, H. R.; Micheau, J. C.; Buhse, T., *Proc. Nat. Acad. Sci.* 2005, 102, 13743.
8. Buhse, T., *Tetrahedron-Asymmetry* 2003, 14, 1055.
9. Gridnev, I. D.; Serafimov, J. M.; Brown, J. M., *Ang. Chem. - Int.Ed.* 2004, 43, 4884.
10. Klankermayer, J.; Gridnev, I. D.; Brown, J. M., *Chem. Commun.* 2007, 3151.
11. Beno, M. A.; Jennings, G.; Engbretson, M.; Knapp, G. S.; Kurtz, C.; Zabransky, B.; Linton, J.; Seifert, S.; Wiley, C.; Montano, P.A. *Nucl. Instrum. Meth, A* 2001, 690, 467.
12. Schroeder, S.L.M.; Moggridge, G.D.; Lambert, R.M.; Rayment, T., *J. Phys. IV*, 1996, C7, 91.
13. Meehan, D.J.; Nchari, L.N.; Hembury, G.A.; Beesley, A.M.; Schroeder, S.L.M.; in preparation.

Appendix III: Stobe Operational Procedures

This section will provide a brief guide on how to carry out a simple StoBe calculation. The critical aspect as with any calculation is to ensure that starting geometry for your molecule or cluster is viable. If it is not any attempted StoBe calculation will not go through to completion. A general outline of what is required for a StoBe calculation is as follows: generation and collection of XYZ or Z matrix data for the StoBe input file, creation of StoBe input file for selected atom, process the calculation, checks made to final output files to ensure calculation is successful, normalisation and plotting of data in excel. Also for all my calculations I retrieved manually from the Stobe out file the core level binding energy specific to that calculation.

So to generate the coordinates this can be done several ways, however I used basic molden imaging software to save my cartesian or z-matrix or the coordinates were directly taken from another calculation. This then was inputted in to the StoBe input file, 2 files are then generated for both the N and NH atom positions. This can be easily done in StoBe as it is just a matter of changing the target atom by inserting a X- dummy line at the bottom of the input file, the target atom will then change from line 1 to line 2. A number of X- dummy commands can be used depending on the order of atoms in the StoBe input file. After the coordinates are inputted a sequential order of basis sets needs to be added in the same order as represented by the coordinates. Below is an example of a Stobe input file for a simple imidazole monomer this input is generated for the NH contribution:

```

title
Study the X-ray absorption spectra of 1S of N. Mulliken.
Nosym
CARTESIAN ANGSTROM
N  1.335425  0.001042  -0.354076  5.  32
N  1.293652  0.000000  1.883303  7.  32
C  0.000000  0.000000  0.000000  6.  32
C  0.000000  0.000000  1.391853  6.  32
C  2.076521  0.000862  0.802174  6.  32
H  3.163924  0.001198  0.800176  1.  32
H  1.702307  0.002166  -1.298413  1.  32
H  -0.798705  -0.000103  -0.737277  1.  32
H  -0.860572  -0.000574  2.057398  1.  32
end
runtime startup
scftype direct
potential local NORM VWN
grid fine
multiplicity 1

```

```

charge 0
maxcycles 100
econvergence 0.0000001
dconvergence 0.0000001
diis on
dmixing mdens 0.1
mulliken on full
fsym scfoc excited
Alfa 17
Beta 17
SYM 1
alfa 1 1 1 0.5
beta 1 0
end
XRAY XAS
end
shrt
end
A-NITROGEN (5,2;5,2)
A-NITROGEN (5,2;5,2)
A-CARBON (4,3;4,3)
A-CARBON (4,3;4,3)
A-CARBON (4,3;4,3)
A-HYDROGEN (3,1;3,1)
A-HYDROGEN (3,1;3,1)
A-HYDROGEN (3,1;3,1)
A-HYDROGEN (3,1;3,1)
O-NITROGEN(+5) (211/211/1)
O-NITROGEN (721/51/1*)
O-CARBON (721/51/1*)
O-CARBON (721/51/1*)
O-CARBON (721/51/1*)
O-HYDROGEN (41)
O-HYDROGEN (41)
O-HYDROGEN (41)
O-HYDROGEN (41)
P-NITROGEN(+5) (3,0;7,0)
P-NITROGEN(+5) (3,0;7,0)
X-DUMMY
X-FIRST
end

```

At this point I should include the respective in ms dos batch files in StoBe that are used to run input files, define parameters eg broadening and output graph data from out files. To run an input file the run_sxa ms dos batch file needs to be edited to include the name of the input, output, molden and spec file. Here is the run_sxa file for the imidazole NH monomer:

```

copy ..\basis\BASEX.new6 fort.3
copy ..\basis\symbasis.new fort.4
..\StoBe.exe < IMIN10x.inp > C:\Documents\IMIN10x.out
copy fort.11 C:\Documents\IMIN10x.spec
copy MOLDEN.mdf C:\Documents\IMIN10x.mdf
del fort.*
copy ..\basis\BASEX.new6 fort.3
copy ..\basis\symbasis.new fort.4
..\StoBe.exe < IMIN10y.inp > C:\Documents\IMIN10y.out
copy fort.11 C:\Documents\IMIN10y.spec
copy MOLDEN.mdf C:\Documents\IMIN10y.mdf
del fort.*

```

This file is then saved and run to produce the StoBe out file. If the calculation is successful and runs to completion the ms dos batch file spec_analy_gau is edited and ran to produce the xy data suitable for excel input. This file also includes an input file for any associated broadening factors to the data and in my case is called N1_1s_sxa. The spec and N1 broadening are shown below:

```

spec_analy_gau
copy C:\Documents\IMIN10x.spec fort.1
..\xrayspec.exe < N1_1S_sxa.inp > C:\Documents\IMIN10x.out
copy XrayT001.out C:\Documents\IMIN10x.spec
del XrayT001.out
del fort.*
copy C:\Documents\IMIN10y.spec fort.1
..\xrayspec.exe < N1_1S_sxa.inp > C:\Documents\IMIN10y.out
copy XrayT001.out C:\Documents\IMIN10y.spec
del XrayT001.out
del fort.*

```

```

N1_1s_sxa
title
N Xray absorption spectrum
print
range 390 420
points 8000
width 0.5 9.0 404 410
xray xas
total 1
end

```

The output for the spec file can then be directly imported to excel and used for the NEXAF spectra related to the atom interrogated by StoBe. All of my simulations involved for any cluster the StoBe simulation for both the N= and NH sites.